Economic Geology
November 2023, Volume 118 Issue 7 Pages 1719-1739
https://doi.org/10.5382/econgeo.4986
https://archimer.ifremer.fr/doc/00819/93144/

Boron and Oxygen Isotope Systematics of Two Hydrothermal Systems in Modern Back-Arc and Arc Crust (PACMANUS and Brothers Volcano, W-Pacific)

Schlicht Lucy E.M. [1, *], Rouxel Olivier [2], Deans Jeremy [3], Fox Stephen [4], Katzir Yaron [4], Kitajima Kouki [5], Kasemann Simone A. [1], Meixner Anette [1], Bach Wolfgang [1]

[1] Faculty of Geosciences and MARUM-Center for Marine Environmental Sciences, University of Bremen, Leobener Str. 8, Bremen 2835, Germany
[2] IFREMER, Unité de Géosciences Marines, Plouzané, France
[3] School of Biological, Environmental, and Earth Sciences, the University of Southern Mississippi, Walker Science Building, 117601-266-5381, USA
[4] Department of Earth and Environmental Sciences, Marcus Family Campus, Ben Gurion University of the Negev, Be´er Sheva 84105, Israel
[5] Department of Geoscience, University of Wisconsin, Madison, Wisconsin 53706, USA

* Corresponding author : Lucy E. M. Schlicht, email address : lucy.schlicht@uni-bremen.de

Abstract :

A better characterization of subsurface processes in hydrothermal systems is key to a deeper understanding of fluid-rock interaction and ore-forming mechanisms. Vent systems in oceanic crust close to subduction zones, like at Brothers volcano and in the eastern Manus basin, are known to be especially ore rich. We measured B concentrations and isotope ratios of unaltered and altered lava that were recovered from drilling sites at Brothers volcano and Snowcap (eastern Manus basin) to test their sensitivity for changing alteration conditions with depth. In addition, for Brothers volcano, quartz-water oxygen isotope thermometry was used to constrain variations in alteration temperature with depth. All altered rocks are depleted in B compared to unaltered rocks and point to interaction with a high-temperature (>150°C) hydrothermal fluid. The δ11B values of altered rocks are variable, from slightly lower to significantly higher than those of unaltered rocks. For Brothers volcano, at the Upper Cone, we suggest a gradual evolution from a fluid- to a more rock-dominated system with increasing depth. In contrast, the downhole variations of δ11B at Snowcap as well as δ11B and δ18O variations at the NW Caldera (Site U1530) of Brothers volcano are suggested to indicate changes in water-rock ratios and, in the latter case, also temperature, with depth due to permeability contrasts between different lithology and alteration type boundaries. Furthermore, δ11B values from the NW Caldera (Site U1527) might point to a structural impact on the fluid pathway. These differences in the subseafloor fluid flow regime, which ranges from more pervasive and fluid-controlled to stronger and controlled by lithological and structural features, have significant influence on alteration conditions and may also impact metal precipitation within the sea floor.

Introduction

Water-rock (w/r) interactions in seafloor hydrothermal systems cause intense exchange of mass and heat between oceanic crust and seawater and can form seafloor massive sulfide deposits of economically important base and noble metals. Hydrothermal activity in back-arc and arc settings is of particular interest because of the commonly observed formation of high-grade and Au-rich ore bodies (e.g., Yang and Scott, 1996) and the similarity to porphyry-type and epithermal ore deposits on land (e.g., Whitney, 1975; Audétat, 2019). The formation of high-grade ore deposits requires a large source of metals from which metals are leached and an ore trap in which the mobilized metals are concentrated efficiently. This mobilization and precipitation of metals in hydrothermal systems strongly depends on the fluid flow regime that is influenced by the presence of faults and fractures as well as by interbedding of more and less permeable strata that can act as barriers for uprising metal-rich fluids (e.g., Zierenberg et al., 1998). Isotopic tracers are useful recorders of temperature of water-rock interactions and the intensity of fluid flow in different domains of the basement (e.g., Kesler, 2005).

Boron is a highly fluid-mobile element and can also show a moderately volatile character, depending on the salinity of solutions (Foustoukos and Seyfried, 2007). In unaltered volcanic rocks B is hosted in clinopyroxene and to a minor extent in plagioclase (Raffone et al., 2008), and also is abundant in the glassy matrix or rather in volcanic glasses (e.g., Marschall et al., 2017). The B concentrations of unaltered whole rocks from back-arc and arc crust are usually elevated (up to 37 µg/g B) compared to MOR (mid-ocean ridge) basalts (< 1 µg/g B) due to addition of B derived from the dehydration of subducted altered oceanic crust and sediments (e.g, Hoog and Savov, 2018). In volcanic rocks that were affected by seafloor hydrothermal alteration, clay minerals like smectites, illite and also chlorite are the major B hosting mineral phases and dominate the B concentration of the altered whole rocks. At low alteration temperatures (< 150 °C) B concentrations of altered whole rocks > 100 µg/g commonly occur due to uptake of B by secondary minerals (mainly clay minerals), while high temperature (> 150 °C) altered volcanic rocks usually show B concentrations lower than the unaltered rock due to leaching (e.g., Thompson and Melson, 1970; Spivack and Edmond, 1987; Smith et al., 1995; James et al., 2003; Yamaoka et al., 2015a).

Boron has two stable isotopes, ^{10}B and ^{11}B, whose ratio (expressed as $\delta^{11}B$) in different reservoirs in back-arc and arc hydrothermal environments strongly deviate. While seawater shows high isotopic values ($\delta^{11}B \approx +40$ ‰), unaltered oceanic crust in back-arc and arc settings shows highly variable but generally lower isotopic values than seawater ($\delta^{11}B \approx -9$ to +16 ‰; Hoog and Savov, 2018; Marschall, 2018 and references therein). The $\delta^{11}B$ values of unaltered volcanic rocks in supra-subduction zones are commonly higher than the MOR basalt average (-7.1 ± 0.9 ‰; Marschall et al., 2017) due to release of B from the subducting slab. Because of the variable isotope ratios of sources, B concentrations and isotope ratios are potentially useful tracers for hydrothermal w/r interaction processes.

This study reports B concentrations and isotope ratios of unaltered rocks from the seafloor and of variably altered rocks from subseafloor sections of active seafloor hydrothermal systems in two supra-subduction zone locations in the Western Pacific. One location is situated in the Manus back-arc basin of Papua New Guinea (Ocean Drilling Program (ODP) Leg 193) and the other location is Brothers volcano in the Southern Kermadec arc, New Zealand (International Ocean Discovery Program (IODP) Expedition 376 "Brothers Arc Flux"). Both cruises were executed aboard the *D/V JOIDES Resolution*. At Brothers volcano, we also measured O isotope ratios of hydrothermal quartz crystals to constrain the temperature range of precipitating fluids and measured Sr isotope ratios for one unaltered rock and several altered rock samples. At both locations, previous work on the composition of discharging fluids (Reeves et al., 2011; de Ronde et al., 2011) and secondary mineralogy (de Ronde et al., 2005; Seewald et al., 2019) indicate reactions between basement rocks and seawater-derived fluids, as well as influx of magmatic vapor rich in H_2O and SO_2 into the hydrothermal systems. Our goal was to obtain a deeper understanding of B isotopic fractionation and the overall variations in B isotopic composition in seafloor hydrothermal systems and to investigate what downhole variations in $\delta^{11}B$ values in combination with $\delta^{18}O$ based temperature estimates can tell us about changes in the fluid flow regime in the sub-seafloor that is an important controlling factor of ore mineral precipitation in hydrothermal systems.

Geological Setting

Snowcap, Manus Basin

The Manus back-arc basin opened along the Manus spreading center and is delimited to the north by the now inactive Manus trench and to the south by the actively subducting New Britain trench (Martinez and Taylor, 1996). ODP Leg 193 drilled several holes in the Pual Ridge, a neovolcanic zone and part of the Southeast Ridges (SER) between the Djaul and Weitin Transforms in the eastern Manus Basin (Fig. 1). Pual Ridge hosts several hydrothermal vent areas, including Snowcap, which is part of the large PACManus hydrothermal area (Binns and Scott, 1993). Snowcap (ODP Leg 193, Site 1188) is in a water depth of 1640 mbsl (meters below sea-level) and features mainly diffusive, low-temperature fluid discharge (6 °C) through a dome-shaped area, interpreted as volcanic dome or cryptodome (Thal et al., 2014). A small cluster of chimneys in the northwestern section of Snowcap dome about 60 m WNW of ODP Site 1188 vents hydrothermal fluids with temperatures between 150 and 180°C (Reeves et al., 2011). Beneath the seafloor, Snowcap consists of dacitic lava flows (Paulick et al., 2004; Thal et al., 2014) that range from unaltered to extensively altered. The discharging fluids at Site 1188 are at 6 °C, and a maximum temperature of 313 °C was measured at 360 mbsf (meters below sea-floor) within borehole 1188F eight days after drilling, which indicates a steep geothermal gradient (Shipboard Scientific Party, 2002). Fluid inclusions in anhydrite indicate high temperatures at depth (270–385°C) but both low and high temperatures in the shallower section, suggesting variable mixing with entrained seawater (Vanko et al., 2004). The presence of abundant native sulfur (Thal et al., 2014) is interpreted as relict of prior venting of acid-sulfate fluids involved in advanced argillic alteration.

Brothers Volcano, Kermadec Arc

Brothers volcano is located in the southern part of the Kermadec arc and represents an active, submarine caldera volcano of 3 to 3.5 km in diameter, approximately 2200 mbsl at the base, 1850 mbsl at the caldera floor and from 1320 to 1540 mbsl at the caldera rim (de Ronde et al., 2019a; Fig. 2). Two neovolcanic cones occur in the southeastern part of the caldera. The larger, Upper Cone reaches 1220 mbsl and is partly connected with the smaller, Lower Cone to the Northeast (Fig. 2B).

Brothers volcano is the most hydrothermally active volcano along the Kermadec arc and hosts two adjacent hydrothermal system types with contrasting fluid chemistry and rock alteration characteristics (de Ronde et al., 2005; de Ronde et al., 2011; de Ronde et al., 2019d). One type is characterized by discharge of high-temperature (≤ 320 °C) fluids that are moderately acidic and are suggested to originate from heating of infiltrating seawater (e.g., de Ronde et al., 2011). This type occurs at the W, NW, and Upper Caldera sites (Sites U1527 and U1530; Fig. 2). The other type is defined by the venting of lower temperature (≤ 120 °C) fluids that are highly acidic, enriched in CO_2 (and other gases) as well as sulfate (de Ronde et al., 2011), and often associated with native sulfur-bearing chimneys. The low pH and abundance of sulfur and sulfate are commonly associated with an influx of magmatic vapors rich in SO_2, which disproportionates upon cooling to form native sulfur and sulfuric acid (e.g., Gamo et al., 1997; de Ronde et al., 2011; Seewald et al, 2015). Active venting of these acid-sulfate fluids occurs at the crests of the neovolcanic Upper Cone (Site U1528). However, the alteration minerals in deeper sections at the NW Caldera (Hole U1530A) also indicate the presence of acid-sulfate fluids at an earlier stage of hydrothermal and magmatic activity (de Ronde et al., 2019c; de Ronde et al., 2019d).

Sample Materials

Snowcap, Manus Basin

We investigated one unaltered plagioclase-phyric dacitic rock that was collected at Snowcap by the ROV *MARUM-QUEST* during the *RV SONNE* Expedition SO-216 (Table 1) and nine rock samples that were drilled during ODP Expedition 193 (Site 1188) and show variable extents of alteration and types of secondary mineral assemblages. Two main alteration types can be distinguished based on the secondary mineralogy: one type typically contains chlorite, illite, and magnetite while the other type (argillic alteration) produces rocks of bleached appearance with pyrophyllite as the main secondary phase, which is commonly accompanied by natroalunite. This pyrophyllite-natroalunite assemblage suggests alteration by acidic fluids at moderate temperatures. The low pH is likely related to the condensation of magmatic SO_2 in the shallow basement above felsic intrusions and is common in suprasubduction magma-hydrothermal systems (e.g, Gamo et al., 1997; Seewald et al., 2019; Hedenquist and Arribas, 2021). The two main alteration types can be further subdivided to five alteration subtypes, using a classification scheme based on previous work (Shipboard Scientific Party, 2002; Lackschewitz et al., 2004; Paulick et al., 2005; Lackschewitz et al. 2006; Paulick and Bach, 2006). In the following, the alteration types are described in order of their occurrence with depth (in brackets are the respective colors in Figure 3):

(1) unaltered dacite (dark gray): seafloor down to ~33.80 mbsf, the dacitic to rhyodacitic rocks are unaltered to weakly altered lava flows that are aphyric to plagioclase-clinopyroxene phyric and moderately vesicular. The groundmass is glassy to microlitic and locally shows a perlitic texture.

(2) Pyrophyllite (prl)-rich alteration (light pink): is manifested by pervasive bleaching and replacement of primary phases by pyrophyllite, accompanied by varying proportions of illite, chlorite, cristobalite, smectite, anhydrite, gypsum, barite, mixed-layer clays

and pyrite down to 116.86 mbsf, with some gaps where pyrophyllite is absent. A second bleached and pyrophyllite-rich zone appears at deeper levels (236.40 to 255.80 mbsf); it has quartz instead of cristobalite.

(3) Illite (ill)-rich alteration (blue): illite is present in most of the altered rocks and is typical for hydrothermal alteration by seawater-derived fluids (K-rich) at elevated temperatures. Besides illite, only quartz or cristobalite, anhydrite and pyrite were detected.

(4) Chlorite (chl)-rich alteration (green): several zones show significant amounts of chlorite, along with illite, quartz or cristobalite, mixed-layer clays, magnetite, anhydrite and pyrite. Especially below 275 mbsf, chlorite becomes a prominent secondary phase.

(5) Magnetite (mgt)-rich alteration (brown): two depth intervals stand out by the abundance of magnetite (154.98 to 183.87 mbsf and 318.23 mbsf to down to the bottom of the Hole 1188F at 386.7 mbsf), which occurs with illite and/or chlorite, quartz, anhydrite and pyrite as other common secondary phases. Magnetite appears in vesicles, as halos around anhydrite-pyrite veins, and disseminated in the groundmass. In the lower part of the first magnetite-rich section also the clay mineral corrensite was detected.

Brothers Volcano, Kermadec Arc

Brothers volcano consists of dacitic to rhyolitic lavas that are commonly plagioclase-clinopyroxene phyric and show a glassy to microlitic groundmass; as well as volcaniclastic rocks comprising mono- or polymict lapillistones and pyroclastic material (Haase et al., 2006; de Ronde et al., 2019a). At Hole U1530A, a sedimentary unit is also present from 30.70 to 59.62 mbsf, comprised of mud-, silt-, and sandstone (de Ronde et al., 2019c). In this study, we investigated four rocks from Brothers volcano that were classified as unaltered, plagioclase-clinopyroxene phyric, dacitic lavas. Two samples were collected by ROV *MARUM-QUEST* during *RV Sonne* Expedition SO-253 (one at the NW Caldera and one at the Upper Cone site) and two were recovered during IODP drilling Expedition 376, one from Hole U1527A at the NW Caldera and one from Hole U1528D at the Upper Cone (Table 2). We also investigated 76 altered rock samples from Brothers volcano that were recovered during IODP Expedition 376: 24 samples from Site U1527, 28 samples from Site U1528, and 24 samples from Site U1530 (Table 2).

The alteration type classification of Brothers volcano used in this study is based on secondary mineralogy from observations of the IODP Expedition 376 shipboard scientists and XRD data of five drill cores (de Ronde et al., 2019d; de Ronde et al., 2019e). Two of the cores studied here are located at the NW Caldera, approximately 400 m horizontal distance from each other; Site U1527 is located on the rim of the NW Caldera in a water depth of 1464 mbsl and reaches a drilled depth of 238 mbsf, whereas Hole U1530A was drilled to 453.1 mbsf on a narrow terrace along the caldera wall at 1595 mbsl (Fig. 2). Five alteration types for the NW Caldera were distinguished in this study (in brackets the dedicated colors in Figure 4 are given):

(1) stockwork zone (red): At the very top of Hole U1530A, rocks of a stockwork zone consisting of bluish altered lava fragments replaced by opal-CT, smectite, chlorite and pyrite were cored. The clasts are surrounded by a network of up to cm-thick veins of anhydrite, barite, pyrite, sphalerite and minor chalcopyrite.
(2) chlorite (chl)-rich alteration (green): this alteration type underlies the stockwork zone in Hole U1530A and is the only alteration type at Site U1527 underneath the unaltered dacitic cap. The protoliths are lava flows, volcaniclastic, pyroclastic and sedimentary rocks. The main alteration color is green but at Site U1527 some parts are brownish in color. The secondary mineral assemblage comprises chlorite, quartz, illite and pyrite. In Hole U1527C chalcopyrite and the Na-Ca-K-rich zeolite mordenite were detected.

In core from Hole U1530A, plagioclase is pseudomorphed by chlorite, anhydrite, quartz and smectite and vugs are commonly lined by quartz and anhydrite. At deeper levels of Hole U1530A, several intersections of chlorite-rich alteration of massive lava flows (Fig. 4D) alternate with pyrophyllite-rich (4) and pyrophyllite-diaspore-rich (5) alteration types.

(3) Illite (ill)-rich alteration (blue): In Hole U1530A between 65.65 and 185.16 mbsf, an illite-rich assemblage occurs, accompanied by quartz, pyrite and chlorite and mainly hosted in lapillistones and other volcaniclastics.

(4) Pyrophyllite (prl)-rich alteration (light orange): spatially below the illite-rich alteration and starting at 189.16 mbsf, a pyrophyllite alteration together with quartz, illite, pyrite and rutile occurs. The alteration stands out by its bleached appearance that in places affects the whole rock or occurs as halo around veins and fractures.

(5) Pyrophyllite (prl)-diaspore(dsp)-rich alteration (dark orange): starting at 227.50 mbsf and going down-core, the pyrophyllite-rich mineral assemblage already present in the overlying alteration type is accompanied by diaspore, as well as quartz, illite, pyrite, rutile and in the upper part of this alteration type the Al-rich sorosilicate zunyite is present.

Deep in Hole U1527C (220.98 to 226.49 mbsf), there is a zone of plastic deformation in which the rocks have elevated chlorite and illite contents (Fig. 4B).

In addition to the unaltered and altered rock samples, we also investigated hydrothermal quartz separates from the NW Caldera (Hole U1530A) that formed in vugs, veins or matrix.

The third studied drill core is 359-m deep and originates from Hole U1528D at the Upper Cone, situated in a water depth of 1228 mbsl. The uppermost basement of the Upper Cone site comprises unconsolidated dacitic lava fragments (purple cap, Fig. 4A) that contain aggregates of native sulfur. Below around 40 mbsf two alteration types were identified with diffuse boundaries against each other that are strongly interlinked and mixed with each other (in brackets the dedicated colors in Figure 4 are given):

(1) Pyrophyllite (prl)-natroalunite (natro)-rich altered effusive and volcaniclastic rocks show white to light gray color due to strong bleaching. Pyrophyllite, natroalunite, anhydrite and pyrite are the main secondary phases. Veins and vugs are commonly filled with native sulfur, quartz, anhydrite and pyrite.
(2) Illite-rich alteration of lavas and volcaniclastics, show dark to grayish-blue alteration colors and a secondary mineral assemblage of illite, opal-CT, quartz, anhydrite and pyrite.

The rocks at the Upper Cone site (U1528) commonly have a strongly bleached appearance. In deeper sections of Hole U1528D, however, some of the rocks still have relatively unaltered to weakly altered patches that are closely associated with highly bleached, pyrophyllite-natroalunite-rich zones (de Ronde et al., 2019b).

Methods

Preparation of Rock Powders

Geochemical analyses in this study were performed on rock powders. For the unaltered rock samples collected by ROV at Snowcap (SO-216) and at Brothers volcano (SO-253), as well as for the altered rocks from the drill-cores of Brothers volcano (IODP Exp. 376) rock powders were prepared at the University of Bremen, Germany. The outer surface of rock pieces was removed by a diamond saw and the interior was powdered by an agate-ball-bearing mill.

The rock powders of the two unaltered samples from Brothers volcano drill-cores (IODP Exp. 376) were prepared at the GEOMAR – Helmholtz Centre for Ocean Research Kiel, Germany by an agate mortar and mill.

For the altered material from the drill cores of Snowcap (ODP Leg 193), the shipboard-prepared rock powders from the core depository were used.

Boron and Strontium Concentrations

The B concentrations of unaltered and altered rock samples from Snowcap (Manus Basin), as well as B concentrations of the unaltered rocks recovered from Brothers volcano were determined during the course of B isotope ratio measurements using a Thermo Scientific Neptune Plus Multicollector-inductively coupled plasma-mass spectrometer (MC-ICP-MS) at the University of Bremen, following methods described in Hansen et al. (2017). Based on long-term analyses of reference material IAEA-B5 (basalt), boron concentrations are usually determined with an uncertainty of 10% (2RSD). In this study, the average B concentration of four independent sample solutions of IAEA-B-5 was 9.2 ± 1.2 µg/g (2sd), in good agreement with the range of published concentration values (8.9 to 11.3 µg/g B, GeoRem database; query January 2020; http:// georem. mpchmainz.gwdg. de).

The B concentrations of altered rocks from Brothers volcano were measured by ICP-MS at the at the PSO (Pôle Spectrométrie Océan), Brest, France. Before measurements, rock powders (120 mg) were dissolved in a mixture of concentrated HF + HNO_3, evaporated to dryness, subsequently dissolved in concentrated HNO_3 + HCl and evaporated again at 80 °C. Sample concentrations were calibrated against rock reference materials AN-G (anorthosite), IF-G (iron formation) and WS-E (dolerite) from GIT-IWG; BHVO-2 (basalt), W2 (diabase), and DN-C (dolerite) from USGS; and BR (basalt), GH (granite), UB-N (serpentinite) from CNRS-CRPG (Govindaraju, 1994). The reference material BHVO-2 yielded a B concentration of 3.0 µg/g, in agreement with the range of published concentration values (1–3.12 µg/g B) and the compiled value (2.95 µg/g B) of the GeoRem database; query December 2021; http:// georem. mpchmainz.gwdg. de. The detection limit of this method was 0.64 µg/g B and the blank concentration 0.31 µg/g B. The repeatability of values for the same standard solution (BHVO-2) was always better than 4% (2RSD). The intermediate precision was ≤ 20% (2RSD).

The Sr concentrations of altered rock samples from Brothers volcano were measured by ICP-MS at the at the PSO (Pôle Spectrométrie Océan), Brest, France. The detection limit was 0.05 µg/g Sr and the blank concentration was 0.01 µg/g Sr. The repeatability of values for the same standard solution (BHVO-2) was always better than 1% (2RSD).

The Sr concentrations of the unaltered rock samples from Brothers volcano were determined by a SPECTRO Xepos Plus X-Ray fluorescence (XRF) analyzer at the GeoZentrum Nordbayern, FAU Erlangen-Nürnberg. Analyses were performed from fused discs created from the sample powders. The typical repeatability precision expressed as RSD was <2% for high concentrations (basaltic references materials BE-N of 1370 µg/g and BR of 1320 µg/g), <4% for intermediate concentrations (granitic reference material GA of 310 µg/g), and <11% for low concentrations (granitic reference material AC-E of 3 µg/g). The Sr reference values were taken from the GEOREM database.

Boron Isotope Ratios

Preparation of sample material and determination of B isotope ratios of three unaltered and 36 altered rock samples from Snowcap and Brothers volcano were performed in the Isotope Geochemistry Laboratory at MARUM – Centre for Marine Environmental Sciences, University of Bremen. Procedures for isolation and purification of B were adapted from Romer et al. (2014) and are described in further detail in Hansen et al. (2017). The procedure was based on alkaline fusion of rock powders (44.5 to 454.9 mg) with K_2CO_3 as fluxing agent (1:4), followed by a two-step column separation; first with Amberlit IRA 743 and then with AG 50W-X8 (mesh 200-400). An appropriate amount of mannitol was used to keep B stable in solution. Isotope measurements were performed on the MC-ICP-MS using the SIS (stable introduction system consisting of a low flow PFA nebulizer (50 µl) combined with a doublepass quartz spray chamber) and a high- efficiency x-cone (same as for B concentrations). Purified sample and reference solutions were dissolved in 2% HNO_3, closely matched to 50ppb B, and repeatedly analyzed in the standard – sample - standard bracketing mode using unprocessed NIST SRM 951 as standard, supplemented by baseline determination. Boron isotopic compositions are given in the $\delta^{11}B$ (‰) notation: [$\delta^{11}B = \{[(^{11}B/^{10}B)_{sample}/(^{11}B/^{10}B)_{NIST\ SRM\ 951}] -1\}\times1000$]. The digestion and chemical separation technique was checked for B loss and contamination. The total B loss was always < 0.2 % of the total amount of B in sample solution and thus without influence on the B isotope composition. The procedural blank was less than 23 ng B with a $\delta^{11}B$ value of on average -1.7 ± 6.6 ‰ ($2sd_{mean}$). Accuracy and repeatability for the separation procedure and measurement was checked through multiple analyses of reference materials. The certified reference material NIST SRM 951 gave a $\delta^{11}B$ value of -0.1 ± 0.1 ‰ (2sd, n=4). The basaltic reference material IAEA-B-5 gave a $\delta^{11}B$ value of -4.3 ± 0.1 ‰ (2sd, n=3), in good agreement with the compiled value of -4.1 ± 2.7 ‰ from Gonfiantini et al. (2003), and also agreed with measured values of -4.3 ± 0.2 ‰ (2sd, n=3, Hansen et al., 2017) and -4.2 ± 0.2 ‰ (2sd, n=4, Wilckens et al., 2018). The granitic reference material ZGI-GM yielded a $\delta^{11}B$ value of -0.1 ± 0.2 ‰ (2sd, n=3). The uncertainty of the B isotopic composition of rock samples is given as 2sd based on multiple mass-spectrometer analyses.

Strontium Isotope Ratios

The Sr isotope measurements of one unaltered and 18 altered rock samples from Brothers volcano were performed at the Isotope Geochemistry Laboratory at the MARUM. The rock powders were dissolved in several successive steps. It was ensured that the samples were completely in solution; if necessary, the last two steps had to be repeated. First, the powder was dissolved in a 5:1 mixture of concentrated HF and HNO_3 at 140 °C for three days and dried at 80 °C. Then the sample was re-dissolved in a 2:1 mixture of concentrated HCl and HNO_3 for two days at 140 °C, dried at 80 °C, dissolved in 300 µl HNO3 and 150 µl H_2O_2, dried at 65 °C and finally dissolved in 3 ml 2.5 M HNO_3 overnight at 140 °C and dried. The baryte-rich sample from the stockwork zone (376-U1530A-4R-1W, 67-69 cm) left an insoluble residue that had to be removed by centrifugation before purification. Separation and purification of Sr were conducted by column separation prepared with 70 µl Sr.spec^{TM} resin, following the procedure described by Deniel and Pin (2001). Firstly, the sample material dissolved in 1 ml 2 M HNO_3 were loaded on the columns (in 100 µl steps). Secondly, 1.2 ml of 2 M HNO_3, 1 ml 7 M HNO_3 and 0.3 ml 2 M HNO_3 were added (in 100 µl, 500 µl and 100 µl steps) to remove unwanted elements. Subsequently, Sr was collected by adding 1 ml of 0.05 HNO_3 (in 100 µl steps), charged with 30 µl 0.1 M H_3PO_4 and the solution was dried at 90 °C on a hotplate. Removal of organic material was ensured by adding 40 µl of concentrated HNO_3, drying at 90 °C, adding of 40 µl of H_2O_2 and drying again.

The determination of Sr isotopes was performed by a Thermo Scientific TRITON Plus thermal ionization mass spectrometer (TIMS) in the Isotope Geochemistry Laboratory at the MARUM. The instrumental fractionation was corrected to the natural $^{87}Sr/^{86}Sr$ ratio of 0.1194. The procedural blank (< 50 pg Sr) is insignificant compared with the Sr concentration in the sample solutions (≥ 200 ng Sr). The reference material NIST SRM 987 gave a composition of 0.710247 ± 0.000004 ($2sd_{mean}$, n = 1). The analytical accuracy and long-term precision for $^{87}Sr/^{86}Sr$ of reference material NIST SRM 987 was 0.710246 ± 0.000011 ($2sd_{mean}$, n = 24; period: May 2015 to May 2017). This is within the range of published values analyzed by TIMS of 0.710250 ± 0.000034 (2SD, n = 1245, disregarding data < 0.7102 and > 0.7103) calculated from GeoRem database (query September 2017; http:// georem.mpch-mainz. gwdg. de).

In addition, Sr isotopic compositions of 16 altered rock samples from Brothers volcano drill-cores were measured by a Thermo Scientific Neptune MC-ICP-MS at the PSO, Brest, France. Prior to measurements, Sr was purified by a one stage chromatography procedure using

Sr.spec™ resin. The standard reference material NIST SRM 987 measured over three analytical sessions yielded $^{87}Sr/^{86}Sr$ = 0.710251 ± 0.000028 (n=10), 0.710257 ± 0.000018 (n=25), 0.710255 ± 0.000020 (n=50). The in-house seawater standard (IAPSO Standard Seawater) gave $^{87}Sr/^{86}Sr$ = 0.709133 ± 0.000034 (n=5) identical, within uncertainty, to the average of worldwide oligotrophic oceanic water (e.g., El Meknassi et al., 2020). The comparability of Sr isotope data from the two different methods and facilities was checked using rock sample 376-U1530A-39R-2W,78-80. The $^{87}Sr/^{86}Sr$ compositions from the University of Bremen (0.705990 ± 0.000006) and the PSO (0.706007 ± 0.000014) agree within analytical uncertainties.

Oxygen Isotope Analysis of Quartz

From drill-core of Hole U1530A at the NW Caldera of Brothers volcano, 13 quartz separates were handpicked under the binocular microscope, including vein (7) and vug fillings (4) and coarse quartz crystals replacing rock matrices (2). Selected quartz grains from each separate were mounted in epoxy, polished, coated with a thin carbon layer and imaged by cathodoluminescence (CL) to study their inner textures and crystal zoning. The CL imaging was performed using a Gatan CL detector installed on a JEOL Superprobe JXA-8230 at the Hebrew University of Jerusalem.

Oxygen isotope ratios were measured along traverses in single quartz crystals (previously imaged by CL, Appendix Table A1) using the CAMECA IMS-1280 secondary ion mass spectrometer (SIMS) at Wisc-SIMS (Wisconsin Secondary Ion Mass Spectrometer), Department of Geoscience, University of Wisconsin-Madison. Detailed descriptions of the O isotope analytical methods are given elsewhere (Kelly et al., 2007; Kita et al., 2009; Valley & Kita, 2009; Heck et al., 2011; Wang et al., 2014) and the most important points are summarized here. Oxygen isotope analyses were performed by using a primary beam of 2 nA $^{133}Cs^{+}$ ions focused to a spot diameter of approximately 10 μm (1 to 2 μm pit depth). One spot analysis lasted four minutes, including pre-sputtering through the carbon layer, stabilizing of the secondary beam, and centering as well as integrating of the secondary ions. The ions of $^{16}O^{-}$ and $^{18}O^{-}$ were simultaneously collected in two movable Faraday cup detectors, accompanied by collection of $^{16}OH^{-}$ ions in the axial Faraday cup to identify potential water traces in the quartz. The average $^{16}O^{-}$ intensity was 3×10^9 counts per second (cps). A nuclear magnetic resonance (NMR) probe stabilized the magnetic field strength, which was readjusted every 12 hours. Analyses were performed in the standard-sample-standard bracketing mode (four analyses of UWQ-1 quartz followed by up to 20 sample analyses and another four analyses of UWQ-1) to evaluate the reproducibility of measurements and to ensure that measurements were not affected by instrumental drift. Raw $^{18}O/^{16}O$ sample ratios were corrected for the VSMOW oxygen scale based on UWQ-1 standard measurements ($\delta^{18}O_{UWQ\text{-}1}$ = 12.33 ± 0.14 ‰, Kelly et al., 2007). Oxygen isotope ratios are given in the conventional notation: [$\delta^{18}O_{VSMOW}$ (‰) = $\{[(^{18}O/^{16}O)_{sample}/(^{18}O/^{16}O)_{VSMOW}] - 1\} \times 1000$]. The intermediate precision of the $\delta^{18}O$ bracketing standard measurements was on average ±0.2 ‰ (2sd, n=27).

Results

Unaltered Rocks

The unaltered dacite sample from Snowcap has a B concentration of 21.7 µg/g and a $\delta^{11}B$ value of +6.8 ± 0.1 ‰, close to the values measured for the two unaltered dacites from Brothers volcano (18.7 and 19.6 µg/g B and $\delta^{11}B$ values of +4.8 ± 0.1 and +5.8 ± 0.1 ‰). The unaltered rocks from Brothers volcano have a Sr isotope ratio of 0.703970 ± 0.000004 at the Lower Cone and 0.704109 ± 0.000006 at the NW Caldera site and Sr contents of 202 µg/g and 232 µg/g, respectively.

Altered Rocks

The B concentrations and $\delta^{11}B$ values of altered rocks from Snowcap (Fig. 3) range from 1.2 to 7.8 µg/g and +5.0 ± 0.1 to +23.2 ± 0.1 ‰, respectively (Table 1, Fig. 5A). The two advanced argillic altered rocks that were sampled from Snowcap have slightly higher B concentrations (4.8 and 7.8 µg/g) compared to the other altered rocks that were recovered from Snowcap (up to 3.9 µg/g). The highest $\delta^{11}B$ value at Snowcap of +23.2 ± 0.1 ‰ is reached at 174.36 mbsf for an altered rock with a magnetite-illite-(corrensite)-rich alteration mineral assemblage.

Altered rocks from the three drill sites at Brothers volcano (Fig. 4) range from 0.8 to 5.2 µg/g B (with one exceptional value of 15.6 µg/g) and from +1.2 ± 0.1 to +16.7 ± 0.1 ‰ in $\delta^{11}B$ (Table 2, Fig. 5A, B). Three altered rocks from the upper part of Hole U1527C have $\delta^{11}B$ values lower than unaltered rock, whereas two rocks from a deformed zone that appears between 220.98 and 226.49 mbsf have higher than unaltered rock $\delta^{11}B$ values (Fig. 4B). At Site U1528, altered rock samples shallower than ca. 75 m have increased $\delta^{11}B$ values compared to unaltered rock, while altered rock samples deeper than 75 m have lower than unaltered rock $\delta^{11}B$ values (Fig. 4C). At Hole U1530A $\delta^{11}B$, values of altered rocks are usually higher than fresh values, beside one sample at 127.11 mbsf with a lower value of +1.2 ± 0.1 ‰. The $\delta^{11}B$ values at Hole U1530A alternate between higher and lower values with depth (Fig. 4D).

Altered rocks at Brothers volcano have Sr concentrations between 15 µg/g and 766 µg/g. The $^{87}Sr/^{86}Sr$ values lie between 0.704190 ± 0.000005 and 0.706982 ± 0.000013 (Fig. 5B, D).

Oxygen Isotope Ratios and $\Delta^{18}O_{Qtz\text{-}H2O}$ Thermometry

The CL images in Figure 6 show representative microtextural features of individual quartz crystals that were separated from altered rocks of Hole U1530A at the NW Caldera of Brothers volcano. A hydrothermal origin of the investigated quartz crystals was suggested because the crystals were either hand-picked from vein or vug fillings and thus were certainly precipitated from solutions, or the crystals were separated from the matrix and were texturally closely associated with the secondary mineral assemblage. The vug-filling quartz crystals from the top part of Hole U1530A show µm-scale alternating CL-brighter and CL-darker growth bands, representing progressive stages of hydrothermal precipitation or continuous growth with varying fluid composition (Fig. 6B). The CL images of quartz crystals from intermediate depth in Hole U1530A show healed fractures with CL-brighter or CL-darker quartz compared to the surrounding quartz crystal (Fig.6), also indicative of a later stage crystal growth under shifted hydrothermal precipitation conditions. The variations in the CL-imaging spectrum of quartz can be explained by different intrinsic and extrinsic defects, like lattice defects, poor crystallographic ordering, or incorporation of trace elements to a certain extent (Götze et al., 2001). Several CL images of euhedral shaped quartz crystals separated from vein or vug infills reveal concentric zoning, indicative of free growth towards open spaces within the host rocks (Fig. 6).

The $\delta^{18}O$ values from traverses across 13 quartz grains from Hole U1530A are given in Table 3. Eight of the traverses, representative of six depth intervals in Hole U1530A, are shown with corresponding CL images in Fig. 6. The total range in measured $\delta^{18}O$ values is +5.6 ± 0.1 ‰ to +9.9 ± 0.2 ‰. One quartz crystal with concentric zoning from the deeper part of Hole U1530A (Fig. 6E, rightmost) shows the highest variability in $\delta^{18}O$ values of an individual crystal from +6.7 ± 0.2 ‰ (crystal rim) to +9.5 ± 0.2 ‰ (crystal core).

Quartz precipitation temperatures were calculated using qtz-water oxygen isotope thermometry, as calibrated by Sharp and Kirschner (1994): $1000 \ln \alpha_{(qtz\text{-}water)} = -2.9 + (3.65 \times 10^6/T^2)$. The calculations are based on the assumption that the measured $\delta^{18}O$ values of the quartz crystals represent the equilibrium values with the interacting hydrothermal fluid during precipitation of the quartz. The exact $\delta^{18}O$ of the interacting fluid is unknown but it is assumed to be near seawater, and we calculated a temperature range for the minimum ($\delta^{18}O_{water}$ = 0 ‰) and maximum ($\delta^{18}O_{water}$ = +1 ‰) values measured in fluids venting at the NW Caldera (de Ronde et al., 2011). The calculated temperatures show±3 to ±8 °C (2sd) that derived from $\delta^{18}O$ measurements. However, also regarding the range in $\delta^{18}O$ value of the fluids from 0 to +1 ‰ an average absolute temperature difference of 31 ± 10 °C (2sd) for an individual temperature has to be considered.

The total range of quartz precipitation temperatures is 262 to 425 °C (for $\delta^{18}O_{water}$ between 0 and +1 ‰). Two quartz grains from the stockwork zone at shallow levels (22.07 to 22.09 mbsf) of Hole U1530A yielded comparably low precipitation temperatures (of 278 to 315 °C). Two quartz grains from a lava flow altered to a chlorite-rich secondary mineral assemblage (61.08 to 61.11 mbsf) gave highly variable temperatures (269 to 425 °C), but mostly above 350 °C. Likewise, a primarily chlorite-altered lava flow in greater depth of Hole U1530A (290.86 to 290.88 mbsf) gave high formation temperatures in the range of 334 to 400 °C, except for one measurement very close to a crack within the grain (289 to 315 °C). Quartz separates from host rocks dominated by pyrophyllite and diaspore-rich secondary mineral assemblages from above and below the chlorite-rich altered lava flow show considerable variation in $\delta^{18}O$ values, but a tendency towards lower precipitation temperatures (262 to 353 °C). Quartz separates from the deepest interval (309.83 to 309.85 mbsf) display zoning in the CL images for two of the three quartz crystals (Fig. 6E) and high $\delta^{18}O$ values at the core (formation temperatures as low as 262 °C), enveloped by low $\delta^{18}O$ values at the rim (formation temperatures as high as 380 °C). In the third crystal low $\delta^{18}O$ values were measured only at the outermost edges and these therefore may represent secondary effects.

Discussion

Signatures of Unaltered Rocks

Brothers volcano. The B contents (18.7 and 19.6 µg/g) and $\delta^{11}B$ values (+4.8 ± 0.1 and +5.8 ± 0.1 ‰) of the two unaltered dacites from Brothers volcano lie between the published values of two seamounts to the south of Brothers volcano (Rumble III: B of 10.4 µg/g, $\delta^{11}B$ of 11.5 ± 0.4 ‰, and Rumble IV: B of 15.7 µg/g, $\delta^{11}B$ of 11.5 ± 0.4 ‰, Leeman et al., 2017) and the volcanic edifices of the Northern Kermadec arc (B > 20 µg/g and $\delta^{11}B$ of up to 7.0 ± 0.5 ‰, Leeman et al., 2017). This is in agreement with the overall increase in B concentrations and $\delta^{11}B$ values along the Tonga-Kermadec volcanic arc from New Zealand northwards that was described by Leeman et al., 2017 and was attributed by them to a steeper thermal gradient or a greater sedimentary influence in the magma source to the south.

Snowcap, PACMANUS. The Manus back-arc basin exhibits a complicated tectonic constellation, with the inactive Manus trench to the north and the actively subducting New Britain trench to the south (Martinez and Taylor, 1996, Fig. 1). The Southeast Rifts (SER), of which Pual Ridge with the Snowcap hydrothermal area is a part, were suggested to represent back-arc crust in an early rifting stage that shows geochemical indications of present influx from slab subduction to the south (Park et al., 2010; Beier et al., 2015). Typical evidence for slab influx is an increased abundance of fluid mobile elements, like B, in rocks from arcs and back arc basins (up to 37 µg/g B) compared to MORB (< 1 µg/g B, Hoog and Savov, 2018), and variable but tends to be higher $\delta^{11}B$ values ($\delta^{11}B \approx$ -9 to +16 ‰; Hoog and Savov, 2018; Marschall, 2018 and references therein) compared to MOR basalt average (-7.1 ± 0.9 ‰; Marschall et al., 2017). In line with these predictions, the unaltered dacitic sample from Snowcap has arelatively high B content of 21.7 µg/g and a $\delta^{11}B$ value of +6.8 ± 0.1 ‰, similar to other volcanic edifices of the SER that showed B concentrations of 11.8 to 23.7

µg/g and $\delta^{11}B$ values in a range of +6.5 to +8.3 ‰ (Wilckens et al., 2018). This indicates that the dacitic rocks at Snowcap experienced significant contribution from the subducting slab.

Signatures of Altered Oceanic Crust

Boron Concentrations and Isotope Ratios. During hydrothermal alteration of mafic and felsic rocks, B tends to partition into the fluid phase at higher temperatures (> 150 °C) and into the solid phase at lower temperatures (<150 °C, e.g., Ishikawa and Nakamura, 1992). The B isotopic fractionation during fluid-rock interaction is controlled by variations in temperature, mineralogy and w/r-ratios (Spivack and Edmond, 1987). The potential pH effect on B isotopic fractionation is negligible in hydrothermal systems that are hosted in basaltic or more felsic crust because the interacting fluids have pH values < 5 at which the $B(OH)_3$ species dominates (e.g., Kakihana et al., 1977, Spivack and Edmond, 1987, Palmer et al., 1987). Altered rocks usually show an increase in $\delta^{11}B$ values by progressive alteration compared to unaltered oceanic crust (≤ +16 ‰, also regarding unaltered crust in arc and back-arc basin settings) due to interaction with seawater-derived fluids ($\delta^{11}B$ values of initially +40 ‰).

Altered rocks from Brothers volcano and Snowcap are B-depleted relative to unaltered rocks and usually have ≤ 5 µg/g, corresponding to a B loss of ≥ 75 % (Fig. 5A) pointing to extensive alteration at elevated temperatures.

At Snowcap and Brothers volcano the alteration mineral assemblages (Paulick and Bach, 2006; de Ronde et al., 2011), fluid inclusion data (Vanko et al., 2004; de Ronde et al., 2005; Diehl et al., 2020; Lee et al., 2022), as well as temperature, acidity and gas concentrations of vent fluids (de Ronde et al., 2011; Kleint et al., 2019; Reeves et al., 2011) suggest the existence of two distinct types of hydrothermal activity. One of these types is thought to be dominated by heated seawater-rock interaction. The chlorite-, illite- and magnetite-(corrensite)-rich alteration types at Snowcap and Brothers volcano as well as the mixed alteration types that occur at Snowcap and the stockwork alteration at Brothers volcano are thought to be part of this seawater hydrothermal type. This is because the appearance of chlorite points to hydrothermal alteration by entrained seawater (Mg-rich) at elevated temperatures (e.g., Bach et al., 2013). The other type of hydrothermal interaction is advanced argillic alteration, in which the pyrophyllite-alunite and pyrophyllite-diaspore-rich assemblages and the presence of native sulfur are attributed to the influx of a magmatic vapor rich in SO_2 (e.g., de Ronde et al., 2011; Seewald et al., 2019). Wilckens et al. (2018) presented B and $\delta^{11}B$ vent fluid data from Western Pacific back-arc basins that implicate a lowering in $\delta^{11}B$ fluid compositions due to the influence of magmatic fluids compared to solely seawater derived hydrothermal fluids. This shift in $\delta^{11}B$ values of the fluids might also be reflected by differences in the $\delta^{11}B$ composition of altered rocks that are either affected by seawater- or by magmatic-derived fluids. However, the B and $\delta^{11}B$ data of altered rocks from Snowcap and Brothers volcano that were investigated in this study show no systematic difference in B or $\delta^{11}B$ between the advanced argillic alteration and seawater-dominated alteration types (Fig. 5A). The missing evidence for a magmatic fluid imprint on the B and $\delta^{11}B$ values of altered rocks, can be explained by three possibilities: (1) the magmatic fluid and the seawater-derived fluid have similar $\delta^{11}B$ values, (2) overprint of the magmatic fluid signal of the altered rocks due to extensive dilution by high seawater fluxes, (3) overprint by low-temperature (< 150 °C) alteration. A seawater-like $\delta^{11}B$ value of the magmatic fluid is implausible, since lowering in $\delta^{11}B$ of fluids affected by magma degassing versus solely seawater affected fluids was previously observed (Wilckens et al., 2018) and the advanced argillic altered rocks show no noticeable lowering in $\delta^{11}B$ compared to the other altered rocks (Fig. 5A). More likely is a combination of strong dilution of the magmatic fluid by high fluxes of seawater-derived hydrothermal fluids, locally accompanied by a low-temperature alteration overprint. Low-temperature overprint is evident by the occurrence of smectite through-out all three investigated drill cores of Brothers volcano (de Ronde et al., 2019e) and by the abundance of corrensite at intermediate depth at Snowcap (Fig. 3). Nonetheless, a greater extent of low-temperature overprint is unlikely due to the low B concentrations of the altered rocks. One altered rock from the top-part section of Hole U1527C at the NW Caldera of Brothers volcano has comparatively high B concentrations (15.6 µg/g) but the $\delta^{11}B$ value points to higher retention of the unaltered signal and do not support a larger impact by a seawater-derived fluid of high $\delta^{11}B$ composition (Fig. 4B).

The previous paragraph emphasized that secondary mineralogy and differing fluid sources seem to have a minor effect on B and $\delta^{11}B$ systematics of altered rocks at Brothers volcano and Snowcap. Instead, the B content and $\delta^{11}B$ composition of altered rocks are potentially more strongly affected by alteration temperatures and w/r-ratios. The low B concentrations of altered compared to unaltered rocks and high $\delta^{11}B$ values of altered rocks, up to +23.2 ± 0.1 ‰ at Snowcap and +16.7 ± 0.1 ‰ at Brothers volcano, point to extensive high-temperature fluid-rock interaction with a seawater-derived fluid (Fig. 5A). The Sr isotope ratio of hydrothermally altered rocks is a well-established proxy for w/r-ratios (McCulloch et al., 1980; Marks et al., 2015). The $\delta^{11}B$ values show a weak positive ($R^2 = 0.3$) but nonetheless significant ($F_{krit} << F$, $p < 0.05$) correlation with Sr isotope ratios of altered rocks from Brothers volcano (Fig. 5B), suggesting that B isotopes are also influenced by w/r-ratios but there are also other impact factors. A significant difference is that $^{11}B/^{10}B$ fractionate in dependance on temperature and potentially also the secondary minerals during fluid-rock interaction (Spivack and Edmond, 1987), while $^{87}Sr/^{86}Sr$ show no isotopic fractionation. Further, B is strongly depleted in the altered rocks which indicates more efficient leaching of B relative to Sr (Table 2). To test the impact of various w/r-ratios on the B and $\delta^{11}B$ values of altered rocks for different temperatures, we modified a model calculation suggested by Yamaoka et al. (2015a) to estimate the change in altered rock composition with increasing reaction progress (Fig. 7). The calculation is based on reaction of multiple batches of fluids in equilibrium with a progressively altered rock portion. The changing B concentration of the altered rock (C_R) can be calculated by using the following mass balance:

$$C_R + (W/R)C_F = C_R^i + (W/R)C_F^i \qquad (2)$$

where C_R^i is the B concentration of the unaltered rock (20.0 µg/g, average B concentration of unaltered rocks from Brothers volcano and Snowcap), C_F^i is the B concentration of seawater (4.5 µg/g), and *W/R* is the water/rock-ratio. Further, the distribution coefficient between rock (C_R) and fluid B concentrations (C_F) of D_B that is defined as $D_B=C_R/C_F$ is needed for the calculation. The D_B value is temperature-dependent due to the preferred B partitioning into the fluid phase at elevated temperatures (e.g., Ishikawa and Nakamura, 1992). It is also influenced by the nature of the secondary mineral assemblage. Yamaoka et al. (2012) estimated a D_B of 0.1 (and also tested 0.3) at 350 °C for their model calculations in a basalt-hosted system. For later model calculations of a basalt-hosted (Yamaoka et al., 2015a) and a back-arc-hosted system of more felsic rock compositions (Yamaoka et al., 2015b), a D_B value of 0.1 at 300 °C was assumed. In this study, D_B values of 0.1 for 300 °C, 0.3 for 250 °C, 0.6 for 200 °C, and 1 for 150 °C were used to emphasize the enhanced partitioning of B towards the fluid with increasing temperatures. The main B hosting phases in basalt-fluid as well as dacite-fluid hydrothermal systems are newly formed clay minerals (e.g. chlorite, illite, smectite) and therefore the approach to use similar D_B values for basaltic as well as more felsic hosted hydrothermal systems might be acceptable.

The changing B isotope ratio of the altered rock (${}^{11/10}B_R$) is based on a mass balance assuming a B isotopic fractionation factor, α, between the B isotope ratio of the rock and fluid (${}^{11/10}B_F$) that is defined as $\alpha={}^{11/10}B_R/{}^{11/10}B_F$:

$$[C_R\,{}^{11/10}B_R + \left(\frac{W}{R}\right) C_F\,{}^{11/10}B_F]/[C_R + (W/R)C_F]$$

$$= \left[C_R^i\,{}^{\frac{11}{10}}B_R^i + \left(\frac{W}{R}\right) C_F^i\,{}^{\frac{11}{10}}B_F^i\right]/[C_F^i + \left(\frac{W}{R}\right) C_F^i] \qquad (3)$$

where $^{11/10}B_R^i$ is the B isotope ratio of the unaltered rock (+5.8 ‰, deduced from the average δ^{11}B value of unaltered rocks from Brothers volcano and Snowcap), and $^{11/10}B_F^i$ is the B isotope ratio of seawater (+39.6 ‰, Foster et al., 2010). The α values for different temperature conditions (0.985 for 300°C, 0.983 for 250 °C, 0.981 for 200 °C, and 0.979 for 150 °C) were calculated based on the empirical calibration of mica-fluid B isotope fractionation by Wunder et al. (2005). This procedure is appropriate to address the $^{11/10}B$ partitioning between minerals and fluids, which is affected by the coordination of B in the interacting phases (e.g. Kakihana et al., 1977). Micas and the likely B hosting mineral phases in the altered dacites (illite, pyrophyllite, chlorite or smectites) have in common that B is tetrahedrally coordinated (e.g. Williams et al., 2001, Hervig et al., 2002).

The results of the model calculations show the potential influence of changes in the w/r-ratios and temperature on the B and δ^{11}B composition of the altered rocks (Fig. 7). In accordance to the model (Fig. 7), a fast onset of significant B loss from the rocks with increasing reaction progress can be expected that is even greater at elevated temperatures. In early stages of fluid-rock interaction when a significant portion of primary B is still retained, the δ^{11}B composition of the altered rocks is expected to decrease relative to the unaltered rocks due to the preference of ^{11}B for the trigonal B species that is dominant in acidic fluids that leads to a passive enrichment of ^{10}B in tetrahedrally coordinated silicates (Kakihana et al., 1977; Palmer et al., 1987; Spivack and Edmond, 1987). In later stages when the proportion of fluid- relative to rock-derived B becomes greater, a distinct increase in δ^{11}B values of the altered rocks with progressing fluid-rock interaction can be expected due to the high δ^{11}B values of seawater-derived fluids (Fig. 7).

For Snowcap, the model results and measured δ^{11}B values of the altered rocks indicate that the illite-magnetite-(corrensite)-altered rocks around 170 to 190 mbsf experienced very high w/r-ratios. In contrast, the δ^{11}B values of the two advanced argillic altered samples at the top-part of Hole 1188A suggest moderate w/r-ratios and comparatively low alteration temperatures (Fig. 3, Fig. 7). For the NW Caldera site of Brothers volcano, the $\delta^{11}B$ values of altered rocks that are lower than unaltered rock $\delta^{11}B$ values of the upper part in Hole U1527C point to relatively low w/r-ratios according to the model calculation results (Fig. 4B, Fig. 7). The deformed zone that appears in deeper sections of Hole U1527C has higher $\delta^{11}B$ values than the top section and suggests increased w/r-ratios. The more variable $\delta^{11}B$ values of altered rock samples that were recovered from Hole U1530A from the NW Caldera indicate higher variability of w/r-ratios based on the model (Fig. 4D). Noticeable is the decrease in $\delta^{11}B$ values starting from the chlorite-rich lava flow at the top of Hole U1530A downwards to the underlying illite-rich and highly altered volcaniclastics, pointing to a possible decrease in w/r-ratios in this section. At the Upper Cone (Site U1528), in the part above ~75 m the $\delta^{11}B$ values are significantly increased relative to unaltered compositions and point to moderate to high w/r-ratios, while < 75 m the lower than unaltered $\delta^{11}B$ values point to lower w/r-ratios based on the model calculations.

The temperatures assumed in the model calculations are in accordance with estimated alteration temperatures of the seawater dominated alteration (≤ 250 °C) and the advanced argillic alteration potentially influenced by magma degassing (230-350 °C), constrained based on secondary minerals at Brothers volcano (de Ronde et al., 2019d) and oxygen isotopes of clay minerals at Snowcap (Lackschewitz et al., 2004). Indeed, the differences in resulting B and $\delta^{11}B$ composition of altered rocks at differing temperatures (Fig. 7) are rather moderate and insufficiently resolvable, especially due to the strong dependency on the determined D_B value that still has to be defined for dacite-fluid interaction.

In general, limitations of w/r-ratio constraints based on the model calculations are: (1) inappropriate assumptions of alteration temperature could lead to an underestimation of w/r-ratios, (2) modification of the interacting fluid composition towards lower $\delta^{11}B$ than seawater values are not regarded by the model but would also cause underestimation of w/r-ratios, and (3) potential variations of the D_B and α values for different alteration mineral assemblages that would affect $\delta^{11}B$ compositions of altered rocks were not considered. Estimated w/r-ratios based on $\delta^{11}B$ compositions must be regarded as minimal values because the model tends to underestimate the effective w/r-ratios as described above. Nevertheless, the w/r-ratio sensitivity interlinked with a temperature dependency of B distribution and isotopic fractionation makes it a useful complement to other tracers for w/r-ratio variations, like Sr isotope ratios.

Oxygen Isotope Ratios and Temperature Constraints. The $\delta^{18}O$ values of quartz crystals from Hole U1530A at the NW Caldera site of Brothers volcano constrain variations of precipitation temperatures with depth and over time. The stockwork zone in Hole U1530A (NW Caldera site, seafloor to 31.28 mbsf), displays uniformly lower alteration temperatures (278 to 315 °C, Fig. 6) than the underlying basement, likely due to infiltration of cold seawater through cracks and joints close to the seafloor. Fluctuations in the relative intensity of low-T seawater ingress versus pulses of hydrothermal activity with high-T fluid upflow possibly led to the wider range of alteration temperatures (269 to 425 °C) in the chlorite-altered lava flow underlying the stockwork zone. A deeper chloritized lava flow of Hole U1530A shows relatively high and less-variable alteration temperatures (334 to 400 °C) compared to those in the volcaniclastic zones above and below it (262 to 353 °C). These temperature differences may reflect a permeability contrast between the more coherent lava flows and the surrounding volcaniclastic units (Fig. 8). Indeed, the core-to-rim $\delta^{18}O$ zoning in quartz grains from deeper levels of Hole U1530A (Fig. 6) indicates a shift from lower (minimum 262 °C) to higher (maximum 380 °C) temperatures with time. The increase in temperature can be explained by a sealing effect of secondary minerals that led to a decrease in seawater ingress (e.g., Dobson et al., 2003; Heap et al., 2017), which is also indicated by the very few open fractures observed in the core of Hole U1530A (de Ronde et al., 2019c) or by an increase in higher-T fluid pulses in later stages of alteration.

Implications for Subsurface Processes in Hydrothermal Systems

In this section, we combine B and O isotope data to set constraints on w/r-ratios and temperatures with depth and assess potential reasons for variations. Shifts in the w/r-ratios and temperatures are often linked to changes of the fluid flow in the sub-seafloor that in turn is sensitively coupled to mobilization and precipitation processes, potentially also critical for ore formation.

For Snowcap (Site 1188), the comparatively high B concentrations of two altered samples that were taken from the topmost part of the site closely below the dacitic cap indicate relatively low alteration temperatures and moderate w/r-ratios based on the model calculations (Fig. 7). In contrast, for the deeper-seated illite-magnetite-(corrensite)-rich alteration type at Snowcap the model calculation gives very high w/r-ratios (Fig. 7) and $\delta^{18}O$ measurements of clay minerals from this section (Lackschewitz et al., 2004) point to lower alteration temperatures than above and below. An increase in w/r-ratios accompanied by a decrease in alteration temperature might point to a preferred ingress of cold seawater to this domain, potentially due to higher permeability than in the overlying rocks. Indeed, reconstructions of volcanic facies at Snowcap (Paulick and Herzig, 2003; Paulick et al., 2004; Paulick and Bach, 2006) showed that the basement exhibits distinct boundaries between more coherent volcanic lavas and primary as well as re-sedimented hyaloclastites, which likely have distinctly different permeabilities. Thus, the high $\delta^{11}B$ values of the magnetite- and corrensite-rich layer may best be explained by alteration with high w/r-ratios caused by the proximity to the permeability barrier imposed by imposed by more coherent overlying lava flows.

Similar to Snowcap, altered rocks that were recovered from Hole U1530A at the NW Caldera of Brothers volcano show a high variability in $\delta^{11}B$ values with depth (Fig. 4D) that might be the result of changing w/r-ratios due to permeability contrasts between the different lithological units (Fig. 7, Fig. 8). This assumption is supported by $\delta^{18}O_{Qtz}$-derived temperatures that indicate higher alteration temperatures within a lava flow around 291 mbsf (Fig. 6D) compared to the over- and underlying volcaniclastic rocks (Fig. 6C, E), which may point to reduced fluid-induced cooling within the lava flow. Furthermore, at a similar depth around 291 mbsf a coherent lava flow was identified in Hole U1530A that is less affected by alteration and shows a lower porosity than altered volcaniclastics based on microresistivity image facies interpretation and downhole petrophysical measurements (Massiot et al., 2022).

At the Upper Cone (Site U1528) of Brothers volcano, the $\delta^{11}B$ values of altered rocks are high in the upper sections and sharply decrease at around 75 mbsf and downwards (Fig. 4C). This points to an evolution from more fluid-dominated to more rock-dominated alteration conditions with depth. Downhole measurements and borehole wall imaging suggest that also at Site U1528 lava flows become more abundant in deeper parts (~270 mbsf and lower) of the basement (Massiot et al., 2022). The B contents and $\delta^{11}B$ values at the Upper Cone (Site U1528) however show only negligible variations at depths >75 mbsf. This might point to a more pervasive alteration at the Upper Cone site.

Estimates of w/r-ratios and temperatures as well as lithological and structural observations at Snowcap and Brothers volcano suppose a large impact on the sub-seafloor fluid flow regime by permeability contrasts between lithological units. The idea of sealing caps that act as traps for incoming fluids was described for oceanic spreading centers before (e.g., Zierenberg et al., 1998; Roberts et al., 2003). Nevertheless, particularly the shallow water depth (typical < 1000 mbsl) volcanic features in arc- and back-arc environments are hosted in promotes an especially explosive volcanism that often results in the formation of more permeable basement that is prone for entrainment of cold seawater (e.g., Fiske et al., 2001). Cooling within the hydrothermal system is one of the major factors that enhances metal-sulfide precipitation (e.g., Reed and Palandri, 2006), and following the basement structure and permeability distribution of interbedded strata are highly important for ore formation processes (e.g., Tivey, 2007).

Summary and Conclusions

Pathways of fluid flow and the distribution of temperature are primary controls of mass transfers in subseafloor hydrothermal systems. In this study, we investigated the applicability of B concentrations and isotope ratios of altered rocks and O isotope ratios of hydrothermal quartz as tracers for water-to-rock interaction conditions, including w/r-ratios, precipitation temperatures, secondary mineralogy, and different fluid sources. The results indicate that the combination of B and O isotope systematics is a useful approach in assessing variations in w/r-ratios and temperatures of seafloor hydrothermal systems. The approach was used to determine the variability in subseafloor fluid flow intensity and temperature in two felsic rock-hosted hydrothermal systems that are variably affected by influx of magma-derived fluids: Brothers volcano in the Southern Kermadec Arc, and Snowcap vent field in the PACMANUS hydrothermal area on Pual Ridge in the Manus Basin. In both sites, ocean drilling has sampled the subseafloor of hydrothermally active areas, which provides unparalleled insights into basement alteration and mineralization.

For Brothers volcano, at the Upper Cone (Site U1528) a distinct shift from higher to lower $\delta^{11}B$ values with increasing depth occurs that is suggested to be caused by a decrease in w/r-ratios with increasing depth and probably represent a change from fluid- to rock-dominated hydrothermal conditions with depth potentially due to compaction processes. In contrast, at the NW Caldera (Site U1527) a plastically deformed zone in greater depth (220 to 225 mbsf) seems to be influenced by increased w/r-ratios compared to shallower levels of the site. At the NW Caldera (Site U1530) the high variability in $\delta^{11}B$ values of altered rocks that are suggested to be coupled to changing w/r-ratios and the results that were derived from quartz-water oxygen isotope thermometry hint to a strong control of fluid flow by permeability differences between more coherent lava flows and more permeable volcaniclastic rocks. These results highlight that fluid flow in the seafloor can be characterized by a more fluid controlled pervasive flow through the rock column that naturally decreases with depth due to compaction or can be stronger controlled by lithological or structural features.

For Snowcap, high $\delta^{11}B$ values in -magnetite-chlorite altered rocks between 160 and 190 mbsf point to rock alteration under increased w/r ratios. This peak in alteration intensity occurs close to volcanic facies boundaries suggesting that (similar to Site U1530) permeability contrasts between different volcanic units had a strong control on the intensity of fluid flow.

This study hence shows the importance of permeability contrasts on fluid pathways and alteration temperatures in the subseafloor of arc and back-arc hydrothermal systems. Episodes of deformation likewise caused pulses of increased flow of seawater-derived fluids. The variable alteration types (in particular at Site U1530) are most plausibly explained by transients in the intensity of magmatic degassing. Unfortunately, our combined B and O isotopic approach did not turn out a useful tracer for identifying different sources of elements (i.e., magma-derived versus rock-leached). This is because a systematic difference in B isotopic composition of rocks altered by interactions with seawater-derived fluids that were variably affected by magmatic fluids could not be recognized.

The data presented help constrain the conditions of water-rock interactions in two active felsic rock-hosted hydrothermal vent systems both of which have considerable accumulation of polymetallic massive sulfides at the seafloor. It is clear that the basement underneath these sulfide deposits should also be mineralized to some extent, in particular in areas where hot, metal-laden hydrothermal solutions mix with cold entrained seawater. Although we identified zones in the basement where this mixing likely played a role in setting the water-rock interactions, a relation between alteration and mineralization could not be established. This is in part due to the generally low intensity of sulfidization throughout the basement drilled in the two work areas.

Acknowledgements

The authors thank the shipboard participants of ODP Expedition 193, IODP Expedition 376 and of SO-216 and SO-253, including the crews and pilots of *MARUM QUEST*. We also thank P. Brandl, M. Portnyagin, D. Garbe-Schönberg, and F. Hauff for providing the rock powders and performing the Sr concentration measurements of the two unaltered drill-core samples from Brothers volcano. Further, we thank J. Valley for support conducting the oxygen isotope measurements and S. Humphris for her helpful remarks on the manuscript. We also thank R. Trumbull and one anonymous reviewer for their constructive comments. This research used samples and/or data provided by the International Ocean Discovery Program (IODP). This research was funded by the German-Israeli Foundation for Scientific Research and Development grant #I-1357-301.8/2016 to W. Bach and Y. Katzir.

References

Audétat, A., 2019, The Metal Content of Magmatic-Hydrothermal Fluids and Its Relationship to Mineralization Potential: Economic Geology, v. 114, p. 1033–1056.

Bach, W., Jöns, N., and Klein, F., 2013, Metasomatism within the Ocean Crust, in Harlov, D., and Austrheim, H., ed., Metasomatism and the chemical transformation of rock: the role of fluids in terrestrial and extraterrestrial processes, Lecture Notes in Earth System Sciences, Springer, p. 253-288.

Balance, P.F., Ablaev, A.G., Pushchin, I.K., Pletnev, S.P., Birylina, M.G., Itaya, T., Follas, H.A., and Gibson, G.W., 1999, Morphology and history of the Kermadec trench–arc–backarc basin–remnant arc system at 30 to 32°S: Marine Geology, v. 159, p. 35–62.

Beier, C., Bach, W., Turner, S., Niedermeier, D., Woodhead, J., Erzinger, J., and Krumm, S., 2015, Origin of Silicic Magmas at Spreading Centres—an Example from the South East Rift, Manus Basin: Journal of Petrology, v. 56, p. 255–272.

Binns, R.A., and Scott, S.D., 1993, Actively forming polymetallic sulfide deposits associated with felsic volcanic rocks in the Eastern Manus back-arc basin, Papua New Guinea: Economic Geology, v. 88, p. 2226-2236.

Caratori Tontini, F., Davy, B., de Ronde, C.E.J., Embley, R.W., Leybourne, M., and Tivey, M.A., 2012, Crustal Magnetization of Brothers Volcano, New Zealand, Measured by Autonomous Underwater Vehicles: Economic Geology, v. 107, p. 1571–1581.

de Ronde, C.E.J., Hannington, M.D., Stoffers, P., Wright, I.C., Ditchburn, R.G., Reyes, A.G., Baker, E.T., Massoth, G.J., Lupton, J.E., Walker, S.L., Greene, R.R., Soong, C.W.R., Ishibashi, J., Lebon, G.T., Bray, C.J., and Resing, J.A., 2005, Evolution of a Submarine Magmatic-Hydrothermal System: Economic Geology, v. 100, p. 1097–1133.

de Ronde, C.E.J., Humphris, S.E., Höfig, T.W., Brandl, P.A., Cai, L., Cai, Y., Caratori Tontini, F., Deans, J.R., Farough, A., Jamieson, J.W., Kolandaivelu, K.P., Kutovaya, A., Labonté, J.M., Martin, A.J., Massiot, C., McDermott, J.M., McIntosh

I.M., Nozaki, T., Pellizari, V.H., Reyes, A.G., Roberts, S., Rouxel, O., Schlicht, L.E.M., Seo, J.H., Straub, S.M., Strehlow, K., Takai, K., Tanner, D., Tepley III, F.J., and Zhang, C., 2019a, Expedition 376 summary, in de Ronde, C.E.J., Humphris, S.E., Höfig, T.W. and the Expedition 376 Scientists, ed., Proceedings of the International Ocean Discovery Program, v. 376, College Station, Texas.

de Ronde, C.E.J., Humphris, S.E., Höfig, T.W., Brandl, P.A., Cai, L., Cai, Y., Caratori Tontini, F., Deans, J.R., Farough, A., Jamieson, J.W., Kolandaivelu, K.P., Kutovaya, A., Labonté, J.M., Martin, A.J., Massiot, C., McDermott, J.M., McIntosh, I.M., Nozaki, T., Pellizari, V.H., Reyes, A.G., Roberts, S., Rouxel, O., Schlicht, L.E.M., Seo, J.H., Straub, S.M., Strehlow, K., Takai, K., Tanner, D., Tepley III, F.J., and Zhang, C., 2019b, Site U1528, in de Ronde, C.E.J., Humphris, S.E., Höfig, T.W. and the Expedition 376 Scientists, ed., Proceedings of the International Ocean Discovery Program, v. 376, College Station, Texas.

de Ronde, C.E.J., Humphris, S.E., Höfig, T.W., Brandl, P.A., Cai, L., Cai, Y., Caratori Tontini, F., Deans, J.R., Farough, A., Jamieson, J.W., Kolandaivelu, K.P., Kutovaya, A., Labonté, J.M., Martin, A.J., Massiot, C., McDermott, J.M., McIntosh, I.M., Nozaki, T., Pellizari, V.H., Reyes, A.G., Roberts, S., Rouxel, O., Schlicht, L.E.M., Seo, J.H., Straub, S.M., Strehlow, K., Takai, K., Tanner, D., Tepley III, F.J., and Zhang, C., 2019c, Site U1530, in de Ronde, C.E.J., Humphris, S.E., Höfig, T.W. and the Expedition 376 Scientists, ed., Proceedings of the International Ocean Discovery Program, v. 376, College Station, Texas.

de Ronde, C.E.J., Humphris, S.E., Höfig, T.W., Reyes, A.G., and the IODP Expedition 376 Scientists, 2019d, Critical role of caldera collapse in the formation of seafloor mineralization: Geology, v. 47, p. 762–766.

de Ronde, C.E.J., Humphris, S.E., Höfig, T.W., and the Expedition 376 Scientists, 2019e, Proceedings of the International Ocean Discovery Program, v. 376, College Station, Texas.

de Ronde, C.E.J., Massoth, G.J., Butterfield, D.A., Christenson, B.W., Ishibashi, J., Ditchburn, R.G., Hannington, M.D., Brathwaite, R.L., Lupton, J.E., Kamenetsky, V.S., Graham, I.J., Zellmer, G.F., Dziak, R.P., Embley, R.W., Dekov, V.M., Munnik, F., Lahr, J., Evans, L.J., and Takai, K., 2011, Submarine hydrothermal activity and gold-rich mineralization at Brothers Volcano, Kermadec Arc, New Zealand: Mineralium Deposita, v. 46, p. 541–584.

Deniel, C., and Pin, C., 2001, Single-stage method for the simultaneous isolation of lead and strontium from silicate samples for isotopic measurements: Analytica Chimica Acta, v. 426, p. 95–103.

Diehl, A., 2019, Causes for variable hydrothermal vent fluid compositions in intraoceanic arcs : insights from fluid compositions and mineral precipitates of the South Kermadec Arc: Dissertation, Bremen, Germany, The University of Bremen, 170 p.

Diehl, A., de Ronde, C.E.J., and Bach, W., 2020, Subcritical phase separation and occurrence of deep-seated brines at the NW Caldera Vent Field, Brothers Volcano: Evidence from fluid inclusions in hydrothermal precipitates: Geofluids, v. 2020, ID 8868259, pp. 22.

Dobson, P.F., Kneafsey, T.J., Hulen, J., and Simmons, A., 2003, Porosity, permeability, and fluid flow in the Yellowstone geothermal system, Wyoming: Journal of Volcanology and Geothermal Research, v. 123, p. 313–324.

El Meknassi, S., Dera, G., De Rafélis, M., Brahmi, C., Lartaud, F., Hodel, F., Jeandel, C., Menjot, L., Mounic, S., Henry, M., Besson, P., Chavagnac, V., 2020, Seawater $^{87}Sr/^{86}Sr$ ratios along continental margins: Patterns and processes in open and restricted shelf domains: Chemical Geology, v. 558, 119874.

Embley, R.W., Ronde, C.E.J. de, Merle, S.G., Davy, B., and Tontini, F.C., 2012, Detailed Morphology and Structure of an Active Submarine Arc Caldera: Economic Geology, v. 107, p. 1557–1570.

Fiske, R.S., Nada, J., Iizasa, K., Yuasa, M., and Klaus, A., 2001, Submarine silicic caldera at the front of the Izu-Bonin arc, Japan: Voluminous seafloor eruptions of rhyolite pumice: Geological Society of America Bulletin, v. 133, p. 813-824.

Foster, G.L., Pogge von Strandmann, P.A.E., and Rae, J.W.B., 2010, Boron and magnesium isotopic composition of seawater: Geochemistry, Geophysics, Geosystems, v. 11.

Foustoukos, D.I., and Seyfried, W.E., 2007, Fluid Phase Separation Processes in Submarine Hydrothermal Systems: Reviews in Mineralogy and Geochemistry, v. 65, p. 213–239.

Gamo, T., Okamura, K., Charlou, J.-L., Urabe, T., Auzende, J.-M., Ishibashi, J., Shitashima, K., Chiba, H., and Cruise, S.S.P.o.t.M., 1997, Acidic and sulfate-rich hydrothermal fluids from the Manus back-arc basin, Papua New Guinea: Geology, v. 25, p. 139–142.

Gonfiantini, R., Tonarini, S., Gröning, M., Adorni-Braccesi, A., Al-Ammar, A.S., Astner, M., Bächler, S., Barnes, R.M., Bassett, R.L., Cocherie, A., Deyhle, A., Dini, A., Ferrara, G., Gaillardet, J., Grimm., J., Guerrot, C., Krähenbühl, U., Layne, G.D. Lemarchand, D., Meixner, A., Northington, D.J., Pennisi, M., Reitznerová, E., Rodushkin, I., Sugiura, N., Surberg, R., Tonn, S., Wiedenbeck, M., Wunderli, S., Xiao, Y., Zack, T., 2003, Intercomparison of boron isotope and concentration measurements. Part II: Evaluation of results: Geostandards Newsletter: The Journal of Geostandards and Geoanalysis, v. 27, p. 41-57.

Govindaraju, K., 1994, Compilation of working values and sample description for 383 geostandards: Geostandards and Geoanalytical Research, v. 18, p. 1-158.

Götze, J., Plötze, M., and Habermann, D., 2001, Origin, spectral characteristics and practical applications of the cathodoluminescence (CL) of quartz - a review: Mineralogy and Petrology, v. 71, p. 225-250.

Haase, K.M., Stroncik, N., Garbe-Schönberg, D., and Stoffers, P., 2006, Formation of island arc dacite magmas by extreme crystal fractionation: Journal of Volcanology and Geothermal Research, v. 152, p. 316–330.

Hansen, C.T., Meixner, A., Kasemann, S.A., and Bach, W., 2017, New insight on Li and B isotope fractionation during serpentinization derived from batch reaction investigations: Geochimica et Cosmochimica Acta, v. 217, p. 51–79.

Heap, M.J., Kennedy, B.M., Farquharson, J.I., Ashworth, J., Mayer, K., Letham-Brake, M., Reuschlé, T., Gilg, H.A., Scheu, B., Lavallée, Y., Siratovich, P., Cole, J., Jolly, A.D., Baud, P., and Dingwell, D.B., 2017, A multidisciplinary approach to quantify the permeability of the Whakaari/White Island volcanic hydrothermal system (Taupo Volcanic Zone, New Zealand): Journal of Volcanology and Geothermal Research, v. 332, p. 88–108.

Heck, P.R., Huberty, J.M., Kita, N.T., Ushikubo, T., Kozdon, R., and Valley, J.W., 2011, SIMS analyses of silicon and oxygen isotope ratios for quartz from Archean and Paleoproterozoic banded iron formations: Geochimica et Cosmochimica Acta, v. 75, p. 5879–5891.

Hedenquist, J.W., and Arribas, A., 2021, Exploration implications of multiple formation environments of advanced argillic minerals: Economic Geology and the Bulletin of the Society of Economic Geologists, v. 117 (3), p. 609-643.

Hervig, R.L., Moore, G.M., Williams, L.B., Peacock, S.M., Holloway, J.R., and Roggensack, K., 2002, Isotopic and elemental partitioning of boron between hydrous fluid and silicate melt: American Mineralogist, v. 87, p. 769-774.

Hoog, J.C. de, and Savov, I.P., 2018, Boron Isotopes as a Tracer of Subduction Zone Processes, in Marschall, H., and Foster, G., ed., Boron Isotopes, p. 217–247.

Ishikawa, T., and Nakamura, E., 1992, Boron isotope geochemistry of the oceanic crust from DSDP/ODP Hole 504B: Geochimica et Cosmochimica Acta, v. 56, p. 1633-1639.

James, R.H., Allen, D.E., and Seyfried, W.E., 2003, An experimental study of alteration of oceanic crust and terrigenous sediments at moderate temperatures (51 to 350°C): Geochimica et Cosmochimica Acta, v. 67, p. 681–691.

Kakihana, H., Kotaka, M., Satoh, S., Nomura, M., and Okamoto, M., 1977, Fundamental Studies on the Ion-Exchange Separation of Boron Isotopes: Bulletin of the chemical society of Japan, v. 50(1), p. 158-163.

Kelly, J.L., Fu, B., Kita, N.T., and Valley, J.W., 2007, Optically continuous silcrete quartz cements of the St. Peter Sandstone: Geochimica et Cosmochimica Acta, v. 71, p. 3812–3832.

Kesler, S.E., 2005, Ore-Forming Fluids: Elements v.1, p 13-18.

Kita, N.T., Ushikubo, T., Fu, B., and Valley, J.W., 2009, High precision SIMS oxygen isotope analysis and the effect of sample topography: Chemical Geology, v. 264, p. 43-57.

Kleint, C., Bach, W., Diehl, A., Fröhberg, N., Garbe-Schönberg, D., Hartmann, J.F., de Ronde, C.E.J., Sander, S.G., Strauss, H., Stucker, V.K., Thal, J., Zitoun, R., Koschinsky, A., 2019, Geochemical characterization of highly diverse hydrothermal fluids from volcanic vent systems of the Kermadec intraoceanic arc: Chemical Geology, v. 528, p. 119289.

Lackschewitz, K.S., Asada, R., and Paulick, H., 2006, Data Report: Summary of revised alteration phases for PACMANUS hydrothermal field - X-Ray Diffraction Analyses of altered felsic volcanic rocks from Holes 1188A, 1188F, 1189A, and 1189B, in Barriga, F.J.A.S., Binns, R.A., Miller, D.J., and Herzig, P.M., ed., Proceedings of the Ocean Drilling Program Scientific Results, v. 193.

Lackschewitz, K.S., Devey, C.W., Stoffers, P., Botz, R., Eisenhauer, A., Kummetz, M., Schmidt, M., and Singer, A., 2004, Mineralogical, geochemical and isotopic characteristics of hydrothermal alteration processes in the active, submarine, felsic-hosted PACMANUS field, Manus Basin, Papua New Guinea: Geochimica et Cosmochimica Acta, v. 68, p. 4405–4427.

Lee, H.J., Seo, J.H., de Ronde, C.E.J., and Heinrich, C.A., 2022, Fluid Inclusion Evidence for Subseafloor Magmatic-Hydrothermal Processes at Brothers Volcano, Kermadec Arc, New Zealand: Economic Geology Special Issue.

Leeman, W.P., Tonarini, S., and Turner, S., 2017, Boron isotope variations in Tonga-Kermadec-New Zealand arc lavas: Geochemistry, Geophysics, Geosystems, v. 18, p. 1126–1162.

Marks, N., Zierenberg, R.A., and Schiffman, P., 2015, Strontium and oxygen isotopic profiles through 3 km of hydrothermally altered oceanic crust in the Reykjanes Geothermal System, Iceland: Chemical Geology, v. 412, p. 34–47.

Marschall, H., 2018, Boron Isotopes in the Ocean Floor Realm and the Mantle, in Marschall H., and Foster, G., ed., Boron Isotopes, p. 189–215.

Marschall, H.R., Wanless, V.D., Shimizu, N., Pogge von Strandmann, P.A., Elliott, T., and Monteleone, B.D., 2017, The boron and lithium isotopic composition of mid-ocean ridge basalts and the mantle: Geochimica et Cosmochimica Acta, v. 207, p. 102–138.

Martinez, F., and Taylor, B., 1996, Backarc spreading, rifting, and microplate rotation, between transform faults in the Manus Basin: Marine Geophysical Research, v. 18, p. 203–224.

Massiot, C., McIntosh, I., Deans, J., Milicich, S.D., Caratori Tontini, F., de Ronde, C.E.J., Adam, L., Kolandaivelu, K., and Guerin, G., 2022, Petrophysical Facies and Inferences on Permeability at Brothers Volcano, Kermadec Arc, Using Downhole Images and Petrophysical Data: Economic Geology Special Issue.

McCulloch, M.T., Gregory, R.T., Wasserburg, G.J., and Taylor, Jr.H.P., 1980, A neodymium, strontium, and oxygen isotopic study of the Cretaceous Samail ophiolite and implications for the petrogenesis and seawater-hydrothermal alteration of oceanic crust: Earth and Planetary Science Letters, v. 46, p. 201–211.

Palmer, M.R., Spivack, A.J., and Edmond, J.M., 1987, Temperature and pH controls over isotopic fractionation during adsorption of boron on marine clay: Geochimica et Cosmochimica Acta, v. 51, p. 2319-2323.

Park, S.-H., Lee, S.-M., Kamenov, G.D., Kwon, S.-T., and Lee, K.-Y., 2010, Tracing the origin of subduction components beneath the South East rift in the Manus Basin, Papua New Guinea: Chemical Geology, v. 269, p. 339–349.

Paulick, H., and Bach,W., 2006, Phyllosilicate Alteration Mineral Assemblages in the Active Subsea-Floor Pacmanus Hydrothermal System, Papua New Guinea, ODP Leg 193: Economic Geology, v. 101, p. 633–650.

Paulick, H., and Herzig, P.M., 2003, Volcanic facies controls on mass transfer at the active, dacite-hosted Pacmanus hydrothermal system, Manus basin, Papua New Guinea (Ocean Drilling Program Leg 193), in Eliopoulos, G.D. et al., ed., Mineral exploration and sustainable development, Millpress Rotterdam, p. 167–170.

Paulick, H., Herzig, P.M., and Hoernes S., 2005, Data Report: A comprehensive geochemical, mineralogical, and isotopic data set of varibly altered dacitic volcanic rocks from the subsurface of the PACMANUS hydrothermal field (ODP Leg 193), in Barriga, F.J.A.S., Binns, R.A., Miller, D.J., and Herzig, P.M., ed., Proceedings of the Ocean Drilling Program Scientific Results, v. 193.

Paulick, H., Vanko, D.A., and Yeats, C.J., 2004, Drill core-based facies reconstruction of a deep-marine felsic volcano hosting an active hydrothermal system (Pual Ridge, Papau New Guinea, ODP Leg 193): Journal of Volcanology and Geothermal Research, v. 130, p. 31–50.

Raffone, N., Ottolini, L., Tonarini, S., Gianelli, G., and Fridleifsson, G.Ó., 2008, A SIMS study of lithium, boron and chlorine in basalts from Reykjanes (southwestern Iceland): Microchimica Acta, v. 161, p. 307-312.

Reed, M.H., and Palandri, J., 2006, Sulfide Mineral Precipitation from Hydrothermal Fluids: Reviews in Mineralogy and Geochemistry, v. 61(1), p. 609-631.

Reeves, E.P., Seewald, J.S., Saccocia, P., Bach, W., Craddock, P.R., Shanks, W.C., Sylva, S.P., Walsh, E., Pichler, T., and Rosner, M., 2011, Geochemistry of hydrothermal fluids from the PACMANUS, Northeast Pual and Vienna Woods hydrothermal fields, Manus Basin, Papua New Guinea: Geochimica et Cosmochimica Acta, v. 75, p. 1088–1123.

Roberts, S., Bach, W., Binns, R.A., Vanko, D.A., Yeats, C.J., Teagle, D., Blacklock, K., Blusztajn, J.S., Boyce, A.J., Cooper, M.J., Holland, N., and McDonald, B., 2003, Contrasting evolution of hydrothermal fluids in the PACMANUS system, Manus Basin: The Sr and S isotope evidence: Geology, v. 31, p. 805-808.

Romer, R.L., Meixner, A., and Hahne, K., 2014, Lithium and boron isotopic composition of sedimentary rocks — The role of source history and depositional environment: Gondwana Research, v. 26, p. 1093–1110.

Seewald, J.S., Reeves, E.P., Bach, W., Saccocia, P.J., Craddock, P.R., Shanks, W.C., Sylva, S.P., Pichler, T., Rosner, M., and Walsh, E, 2015, Submarine venting of magmatic volatiles in the Eastern Manus Basin, Papua New Guinea: Geochimica et Cosmochimica Acta, v. 163, p. 178–199.

Seewald, J.S., Reeves, E.P., Bach, W., Saccocia, P.J., Craddock, P.R., Walsh, E., Shanks, W.C., Sylva, S.P., Pichler, T., and Rosner, M., 2019, Geochemistry of hot-springs at the SuSu Knolls hydrothermal field, Eastern Manus Basin: Geochimica et Cosmochimica Acta, v. 255, p. 25–48.

Sharp, Z., and Kirschner, D., 1994, Quartz-calcite oxygen isotope thermometry: Geochimica et Cosmochimica Acta, v. 58, p. 4491–4501.

Shipboard Scientific Party, 2001, Leg 193 Preliminary Report: Anatomy of an Active Felsic-Hosted Hydrothermal System, Eastern Manus Basin. ODP Preliminary Reports, 93 (online). Available from World Wide Web: <http://www-odp.tamu.edu/publications/prelim/193_prel/193prel.pdf>, cited 2022-05-29.

Shipboard Scientific Party, 2002, Leg 193 Summary, in Binns, R.A., Barriga, F.J.A.S., and Miller, D.J., ed., Proceedings of the Ocean Drilling Program Initial Reports, v. 193.

Smith, H.J., Spivack, A.J., Staudigel, H., and Hart, S.R., 1995, The boron isotopic composition of altered oceanic crust: Chemical Geology, v. 126, p. 119-135.

Spivack, A., and Edmond, J., 1987, Boron isotope exchange between seawater and the oceanic crust: Geochimica et Cosmochimica Acta, v. 51, p. 1033–1043.

Thal, J., Tivey, M., Yoerger, D., Jöns, N., and Bach, W., 2014, Geologic setting of PACManus hydrothermal area — High resolution mapping and in situ observations: Marine Geology, v. 355, p. 98–114.

Thompson, G., and Melson, W.G., 1970, Boron contents of serpentinites and metabasalts in the oceanic crust: Implications for the boron cycle in the oceans: Earth and Planetary Science Letters, v. 8, p. 61-65.

Tivey, M.K., 2007, Generation of seafloor hydrothermal vent fluids and associated mineral deposits: Oceanography, v. 20, p. 50-65.

Valley, J.W., and Kita, N.T., 2009, In situ Oxygen Isotope Geochemistry by Ion Microprobe, in Fayek. M., ed., MAC Short Course: Secondary Ion Mass Spectrometry in the Earth Sciences, v. 41, p.19-63.

Vanko, D.A., Bach, W., Roberts, S., Yeats, C.J., and Scott, S.D., 2004, Fluid inclusion insights from anhydrite veins up to 350 meters below the seafloor at the deep-sea PACMANUS hydrothermal field. Manus Basin back-arc rift, Papua New Guinea: Journal of Geophysical Research, B03201.

Wang, X-L., Coble, M.A., Valley, J.W., Shu, X-J., Kitajima, K., Spicuzza, M.J., Sun, T., 2014, Influence of radiation damage on late Jurassic zircon from southern China: Evidence from in situ measurement of oxygen isotopes, laser Raman, U-Pb ages, and trace elements: Chemical Geology, v. 389, p. 122-136.

Whitney, J.A., 1975, Vapor generation on a quartz monzonite magma; a synthetic model with application to porphyry copper deposits: Economic Geology, v. 70, p. 346–358.

Wilckens, F.K., Reeves, E.P., Bach, W., Meixner, A., Seewald, J.S., Koschinsky, A., and Kasemann, S.A., 2018, The influence of magmatic fluids and phase separation on B systematics in submarine hydrothermal vent fluids from back-arc basins: Geochimica et Cosmochimica Acta, v. 232, p. 140–162.

Williams, L.B., Hervig, R.L., Holloway, J.R., and Hutcheon, I., 2001, Boron isotope geochemistry during diagenesis. Part I. Experimental determination of fractionation during illitization of smectite: Geochimica et Cosmochimica Acta, v. 65(11), p. 1769-1782.

Wunder, B., Meixner, A., Romer, R.L., Wirth, R., and Heinrich, W., 2005, The geochemical cycle of boron: Lithos, v. 84, p. 206–216.

Yamaoka, K., Ishikawa, T., Matsubaya, O., Ishiyama, D., Nagaishi, K., Hiroyasu, Y., Chiba, H. and Kawahata, H., 2012, Boron and oxygen isotope systematics for a complete section of oceanic crustal rocks in the Oman ophiolite: Geochimica et Cosmochimica Acta, v. 84, p. 543–559.

Yamaoka, K., Matsukura, S., Ishikawa, T., and Kawahata, H., 2015a, Boron isotope systematics of a fossil hydrothermal system from the Troodos ophiolite, Cyprus: Chemical Geology, v. 396, p. 61–73.

Yamaoka, K., Hong, E., Ishikawa, T., Gamo, T., and Kawahata, H., 2015b, Boron isotope geochemistry of vent fluids from arc/back-arc seafloor hydrothermal systems in the western Pacific: Chemical Geology, v. 392, p. 9-18.

Yang, K., and Scott, S.D., 1996, Possible contribution of a metal-rich magmatic fluid to a sea-floor hydrothermal system: Nature, v. 383, p. 420–423.

Zierenberg, R.A., Fouquet, Y., Miller, D.J., Bahr, J.M., Baker, P.A., Bjerkgard, T., Brunner, C.A., Duckworth, R.C., Gable, R., Gieskes, J., Goodfellow, W.D., Gröschel-Becker, H.M., Guerin, G., Ishibashi, J., Iturrino, G., James, R.H., Lackschewitz, K.S., Marquez, L.L., Nehling, P., Peter, J.M., Rigsby, C.A., Schultheiss, P., Shanks III, W.C., Simoneit, B.R.T., Summit, M., Teagle, D.A.H., Urbat, M., and Zuffa, G.G., 1998, The deep structure of a sea-floor hydrothermal deposit: Nature, v. 392, p.485-488.

Fig. 1: Geological setting of the Manus Basin. (A) Location of ODP Leg 193, PACManus in the Manus Basin (yellow star) modified after Thal et al. (2014). An overview map is inserted that shows the position of the Manus Basin in the Pacific with a red dot. (B) Rock types at Pual Ridge, sites of hydrothermal activity (red dots) and location of PACManus, modified after Shipboard Scientific Party (2001) The thick orange lines represent plate boundaries. Open-toothed lines symbolize inactive subduction, while filled-tooth lines indicate active subduction. Thin orange lines in (B) show extensional faults. WIT=Willaumez Transform; METZ=Manus Extensional Transform Zone; DT=Djaul Transform; WT=Weitin Transform; MMP=Manus Microplate; MSC=Manus Spreading Centre; SER=Southeast Ridges.

Fig. 2: Geological setting of the Southern Kermadec arc. (A) Location of Brothers volcano within the Southern Kermadec arc, modified after Ballance et al. (1999). (B) Bathymetric map of Brothers volcano modified from Embley et al. (2012). Light gray patches indicate zones of low magnetization intensity (Caratori Tontini et al., 2012) that are suggested to represent zones of high-temperature fluid upflow. Yellow stars mark drilling locations (IODP Expedition 376) from which samples used in this study came. The red line refers to the cross-section shown in Figure 4.

Fig.3: Variations in boron concentration and isotopic composition of altered rocks and alteration mineral assemblages with depth at Snowcap, ODP Site 1188 (Hole 1188A from 0 to 211.6 mbsf and Hole 1188F from 218 to 386.7 mbsf), Manus Basin. The gray vertical line represents the unaltered rock compositions. Errors of 2sd are smaller than symbol size. Half-boxes represent rocks with mixed alteration types. Mineral abbreviations: prl = pyrophyllite, ill = illite, chl=chlorite, qtz=quartz, crs=cristobalite, sm=smectite, anh=anhydrite, gp=gypsum, ba=barite, py=pyrite, mgt=magnetite, crr=corrensite.

Fig.4: Alteration patterns, lithostratigraphy (after de Ronde et al., 2019e) and geochemical variations with depth at Brothers volcano. (A) Cross-section (see Fig. ***2****B) of Brothers*

volcano and distribution of alteration types based on shipboard observations and XRD analyses of IODP Expedition 376, modified after de Ronde et al. (2019d). Boreholes were projected to the cross-section. (B, C, D): B concentrations and isotopic compositions of altered rocks Sites U1527, U1528 and Site U1530, respectively. The symbols are the same as in Figure 5; symbol colors match alteration type. The errors (2sd) of the B isotopic compositions are smaller than the symbol sizes. The range of unaltered rock compositions is illustrated as light gray vertical line, with the average in dark gray. Mineral abbreviations: plg = plagioclase, px = pyroxene.

Fig.5: Chemical and isotopic compositions of unaltered and variably altered rocks from Snowcap and Brothers volcano. Errors (2sd) of B and Sr isotopes are smaller than symbol size. (A) B concentrations versus $\delta^{11}B$ *compositions. (B) Sr versus B isotopic compositions. Inset shows the relation of the B and Sr isotope composition of unaltered and altered rocks relative to seawater. Mineral abbreviations are given in Fig.3.*

Fig.6: O isotope values ($\delta^{18}O_{VSMOW}$*) and calculated formation temperatures (pink shaded) of quartz grains from different depth intervals and alteration types in Hole U1530A, NW Caldera, Brothers volcano. Temperatures are based on oxygen isotope quartz-water thermometry calibrated by Sharp and Kirschner (1994). The pink shades give the range of minimum and maximum temperatures. (A)* $\delta^{18}O_{VSMOW}$ *and temperatures versus depth, alteration types also included; (B), (C), (D), and (E) show CL images of single quartz grains, including the locations of SIMS analyses, the measured* $\delta^{18}O_{Qtz}$ *values and the corresponding temperatures.*

Fig.7: Model calculations of B contents and isotopic ratio during progressive fluid-rock interaction for varies temperatures, adapted from Yamaoka et al. (2015a). The italic numbers mark the w/r-ratios. An initial rock composition based on average unaltered rock from Brothers volcano and Snowcap (20.0 µg/g and +5.8 ‰), and an initial fluid composition

based on unaltered bottom seawater (4.5 µg/g and +39.6 ‰) were assumed. The observed B and $\delta^{11}B$ compositions of Brothers volcano and Snowcap are shown with the same symbols as in Figure 5. Estimates (see text for details): for 300 °C (D_B=0.1, α=0.985), for 250 °C (D_B=0.3, α=0.983), for 200 °C (D_B=0.6, α=0.981), and for 150 °C (D_B=1.0, α=0.979).

Fig.8: Summary sketch of the alteration evolution at Brothers volcano. Alteration types are the same as in Figure 4. The formation steps (A) Pre-caldera, (B) Caldera collapse and (C) resurgent cone were adapted from de Ronde et al. (2019d). In the pre-caldera stage (A), advanced argillic alteration due to magmatic fluid upflow took place. After collapse of the caldera (B and C), increased seawater ingress was initiated and chlorite- and/or illite-rich alteration occurred. A more detailed section of Hole U1530A at the NW Caldera (D) shows that the more coherent lava-flows act as permeability barriers and exhibit low extents of seawater ingress and increased alteration temperatures (up to 425 °C) compared to the surrounding volcaniclastics that experienced increased seawater ingress and lower alteration temperatures (262 to 353 °C). At the Upper Cone site (C), increased seawater ingress occurs at the topmost part and decreasing with depth, probably due to compaction and sealing of the crust by secondary minerals.

Table 1: Alteration types, secondary mineral assemblages, B concentrations and isotopic compositions of unaltered and altered rocks from Snowcap, Manus Basin.

Table 2: Alteration types, and B and Sr concentrations and isotopic compositions of altered and unaltered classified rocks from Brothers volcano, Kermadec arc.

Table 3: Oxygen isotope ratios ($\delta^{18}O_{VSMOW}$) measured by SIMS of quartz single crystal domains from Hole U1530A, NW Caldera, Brothers volcano.

Appendix Table A1: Oxygen isotope measurements by SIMS on quartz from sample material (IODP Exp. 376, Brothers volcano) and reference material UWQ-1. The position of the measured points is projected to the CL images of the quartz separates.

Fig. 1

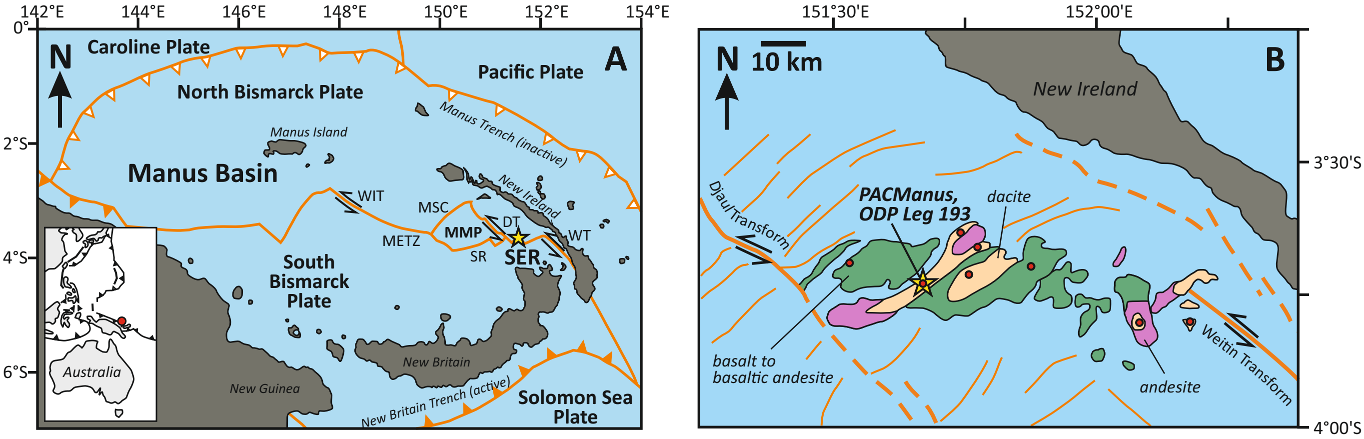

142°E
144°E
146°E
148°E
150°E
152°E
154°E
0°
2°S
4°S
6°S
A
N
Caroline Plate
North Bismarck Plate
Pacific Plate
Manus Island
Manus Basin
Manus Trench (inactive)
New Ireland
WIT
MSC
DT
MMP
METZ
SR
SER
WT
South Bismarck Plate
Australia
New Guinea
New Britain
New Britain Trench (active)
Solomon Sea Plate
151°30'E
152°00'E
3°30'S
4°00'S
B
10 km
New Ireland
Djaul Transform
PACManus, ODP Leg 193
dacite
basalt to basaltic andesite
andesite
Weitin Transform

Fig. 2

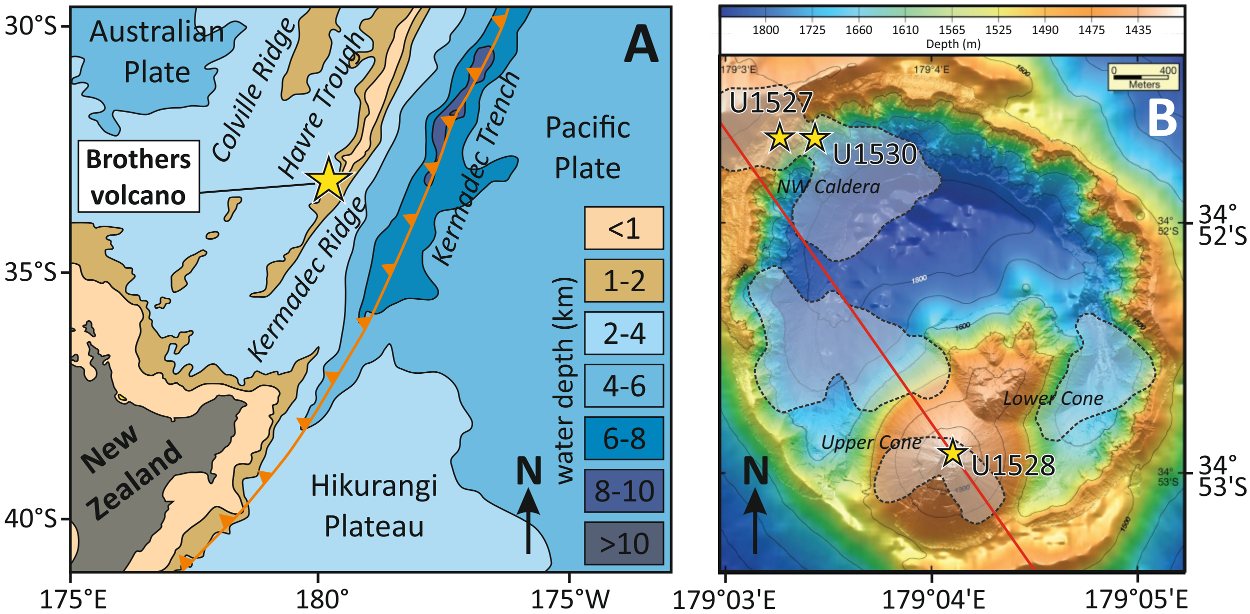

30°S
35°S
40°S
175°E
180°
175°W
Australian Plate
Colville Ridge
Havre Trough
Brothers volcano
Kermadec Ridge
Kermadec Trench
Pacific Plate
New Zealand
Hikurangi Plateau
A
N
water depth (km)
<1
1-2
2-4
4-6
6-8
8-10
>10
1800
1725
1660
1610
1565
1525
1490
1475
1435
Depth (m)
B
U1527
U1530
NW Caldera
Lower Cone
Upper Cone
U1528
N
Meters
34° 52'S
34° 53'S
179°03'E
179°04'E
179°05'E

Fig. 3

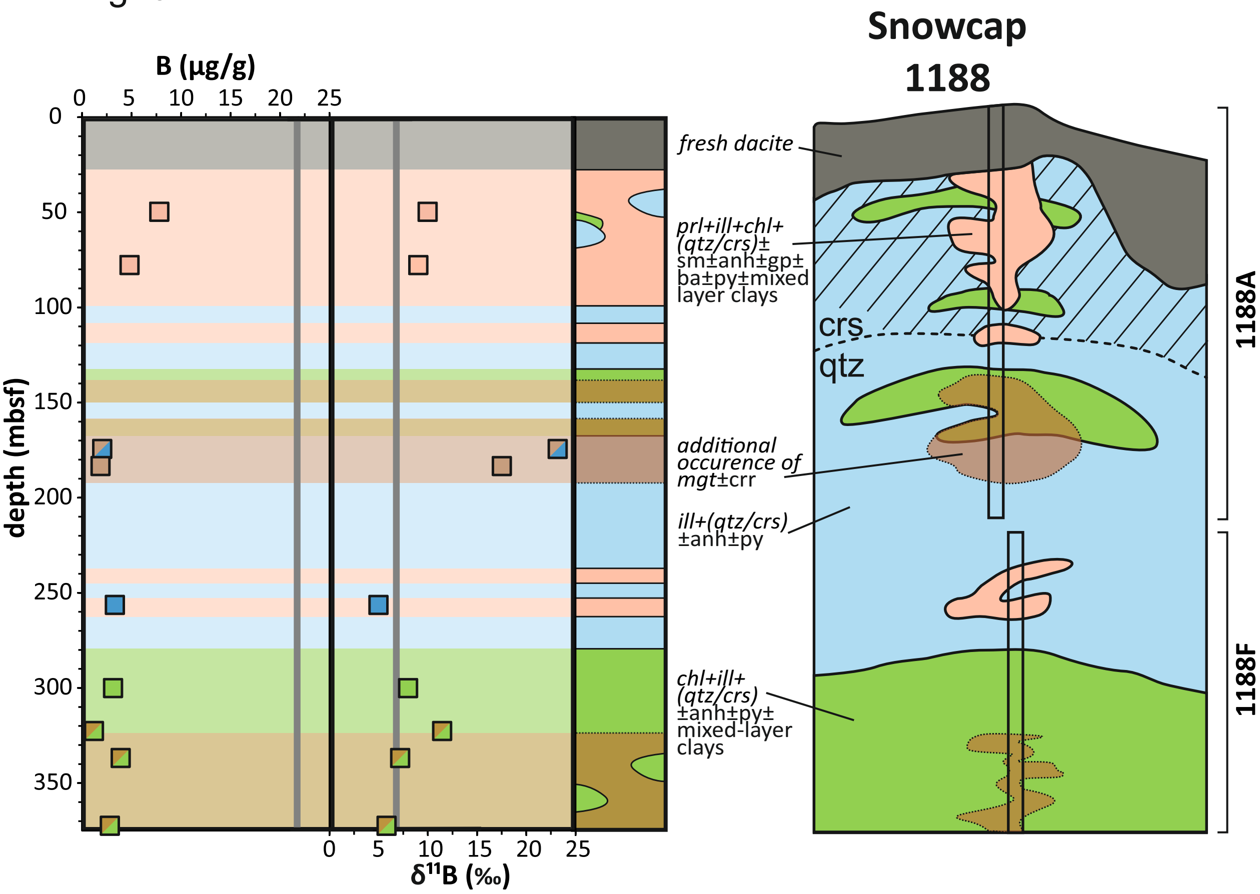

B (µg/g)
0 5 10 15 20 25
depth (mbsf)
0
50
100
150
200
250
300
350
0 5 10 15 20 25
δ¹¹B (‰)
Snowcap
1188
fresh dacite
prl+ill+chl+
(qtz/crs)±
sm±anh±gp±
ba±py±mixed
layer clays
crs
qtz
additional
occurence of
mgt±crr
ill+(qtz/crs)
±anh±py
chl+ill+
(qtz/crs)
±anh±py±
mixed-layer
clays
1188A
1188F

Fig. 4

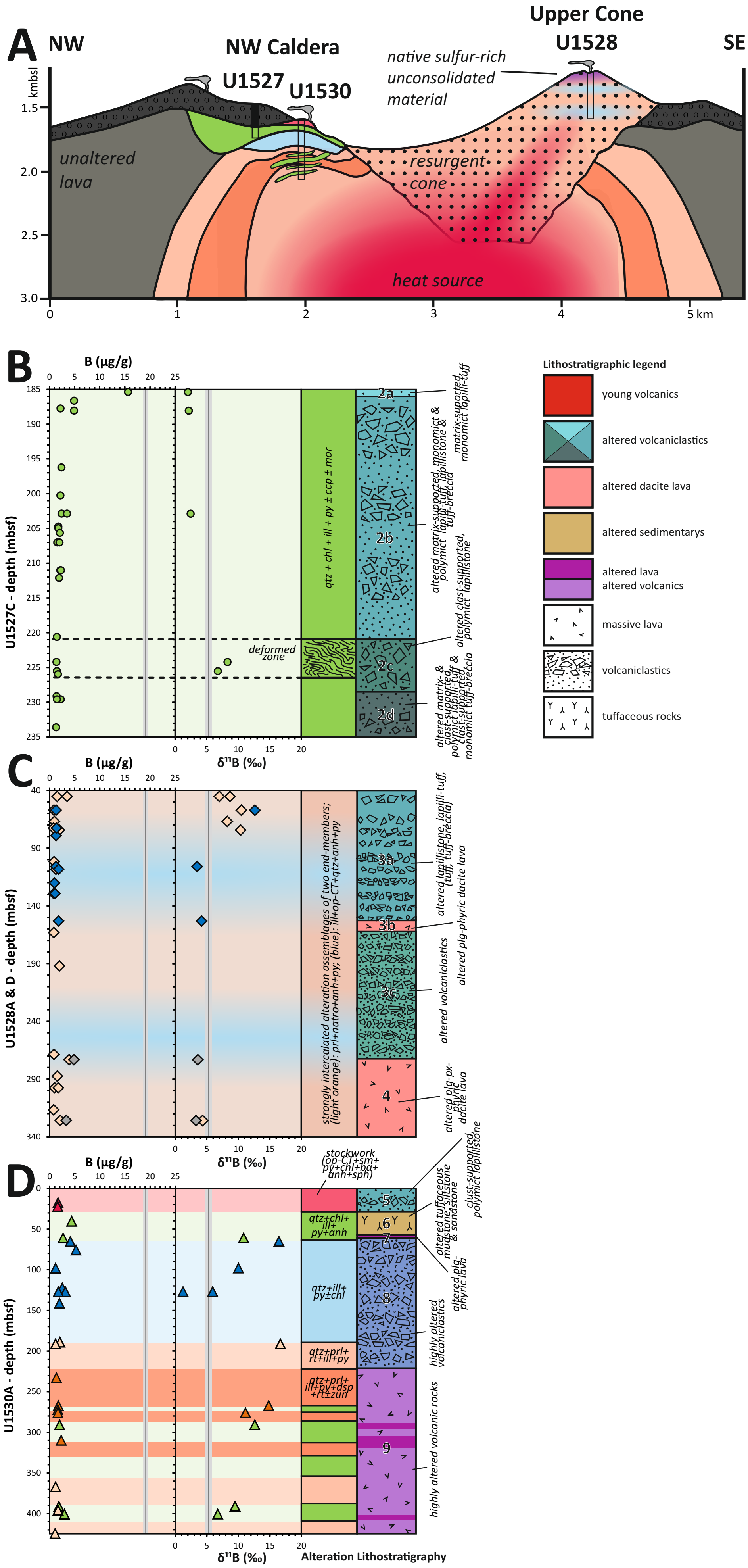
A
NW
NW Caldera
U1527
U1530
Upper Cone
U1528
SE
native sulfur-rich unconsolidated material
unaltered lava
resurgent cone
heat source
kmbsl
5 km
B
B (µg/g)
δ11B (‰)
U1527C - depth (mbsf)
qtz + chl + ill + py ± ccp ± mor
deformed zone
2a
2b
2c
2d
matrix-supported monomict lapilli-tuff
altered matrix-supported monomict & polymict lapilli-tuff, lapillistone & tuff-breccia
altered clast-supported, polymict lapillistone
altered matrix- & clast-supported polymict lapilli-tuff & clast-supported monomict tuff-breccia
C
U1528A & D - depth (mbsf)
strongly intercalated alteration assemblages of two end-members; (light orange): prl+natro+anh+py; (blue): ill+op-CT+qtz+anh+py
3a
3b
3c
4
altered lapillistone, lapilli-tuff, (tuff, tuff-breccia)
altered plg-phyric dacite lava
altered volcaniclastics
altered plg-px-phyric dacite lava
D
U1530A - depth (mbsf)
stockwork (op-CT+sm+py+chl+ba+anh+sph)
qtz+chl+ill+py+anh
qtz+ill+py±chl
qtz+prl+rt+ill+py
qtz+prl+ill+py+dsp+rt±zun
5
6
7
8
9
clast-supported, polymict lapillistone
altered tuffaceous mudstone, siltstone & sandstone
altered plg-phyric lava
highly altered volcaniclastics
highly altered volcanic rocks
Alteration
Lithostratigraphy
Lithostratigraphic legend
young volcanics
altered volcaniclastics
altered dacite lava
altered sedimentarys
altered lava
altered volcanics
massive lava
volcaniclastics
tuffaceous rocks

Fig. 5

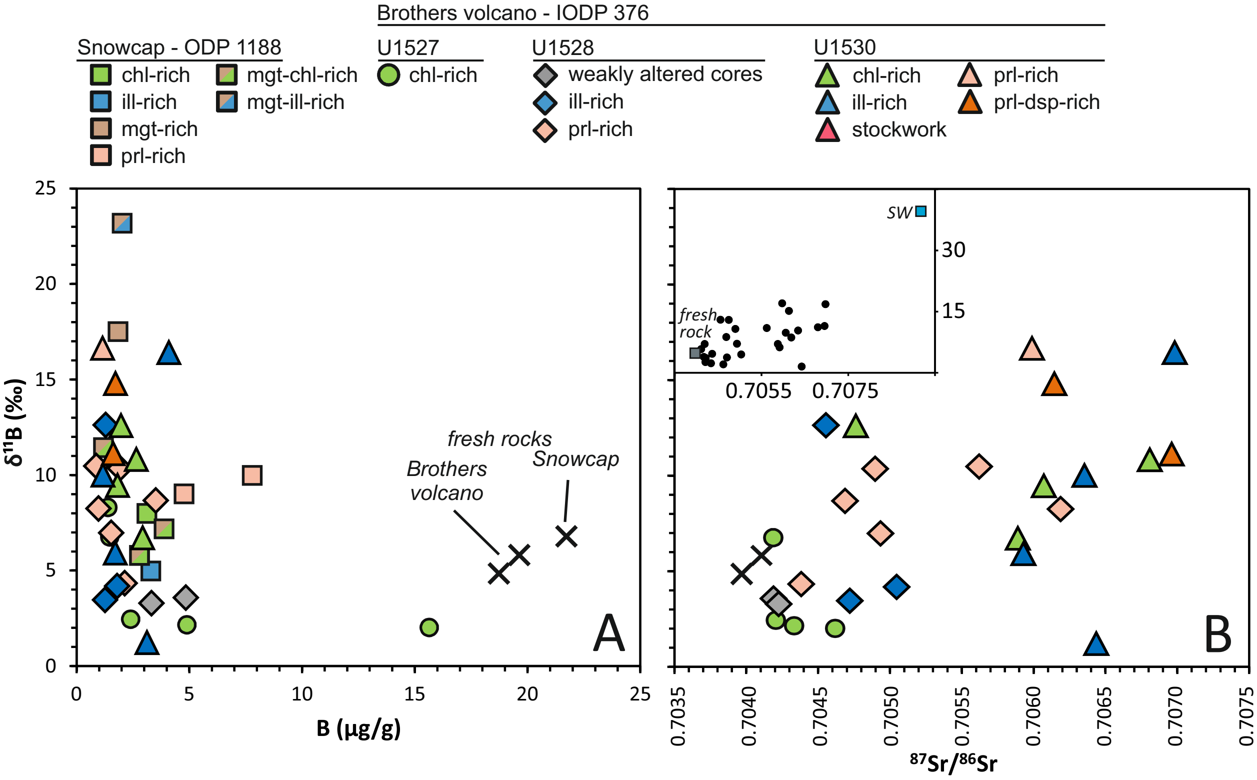

Brothers volcano - IODP 376
Snowcap - ODP 1188
chl-rich
ill-rich
mgt-rich
prl-rich
mgt-chl-rich
mgt-ill-rich
U1527
chl-rich
U1528
weakly altered cores
ill-rich
prl-rich
U1530
chl-rich
ill-rich
stockwork
prl-rich
prl-dsp-rich
δ11B (‰)
B (µg/g)
fresh rocks
Brothers volcano
Snowcap
A
SW
fresh rock
B
87Sr/86Sr

Fig. 6

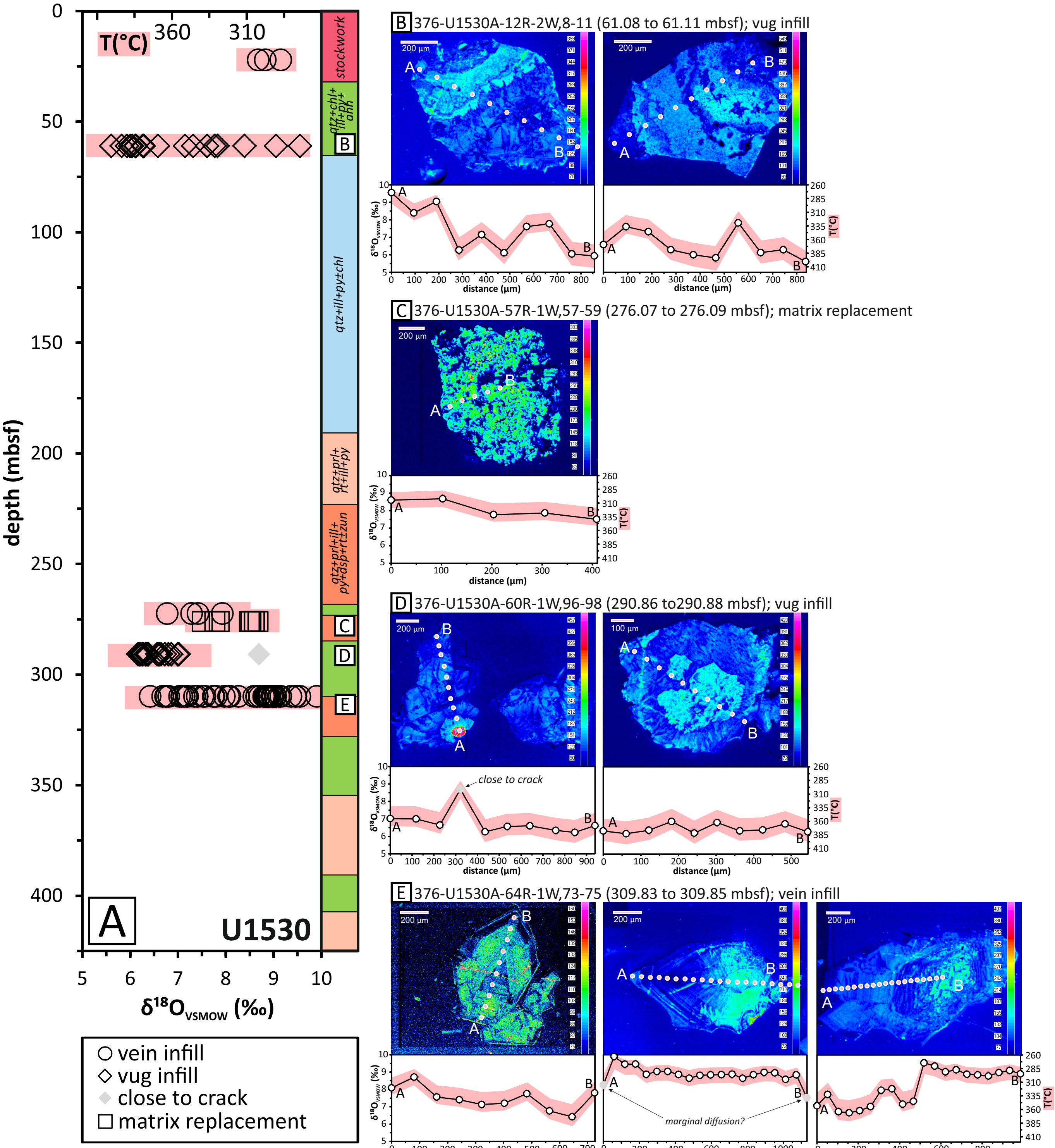

T(°C)
360
310
stockwork
qtz+chl+ill+py+anh
qtz+ill+py±chl
qtz+prl+ill+py
qtz+prl+ill+py+dsp+rt±zun
depth (mbsf)
A
U1530
δ18OVSMOW (‰)
vein infill
vug infill
close to crack
matrix replacement
B 376-U1530A-12R-2W,8-11 (61.08 to 61.11 mbsf); vug infill
C 376-U1530A-57R-1W,57-59 (276.07 to 276.09 mbsf); matrix replacement
D 376-U1530A-60R-1W,96-98 (290.86 to290.88 mbsf); vug infill
close to crack
E 376-U1530A-64R-1W,73-75 (309.83 to 309.85 mbsf); vein infill
marginal diffusion?
distance (µm)
T(°C)

Fig. 7

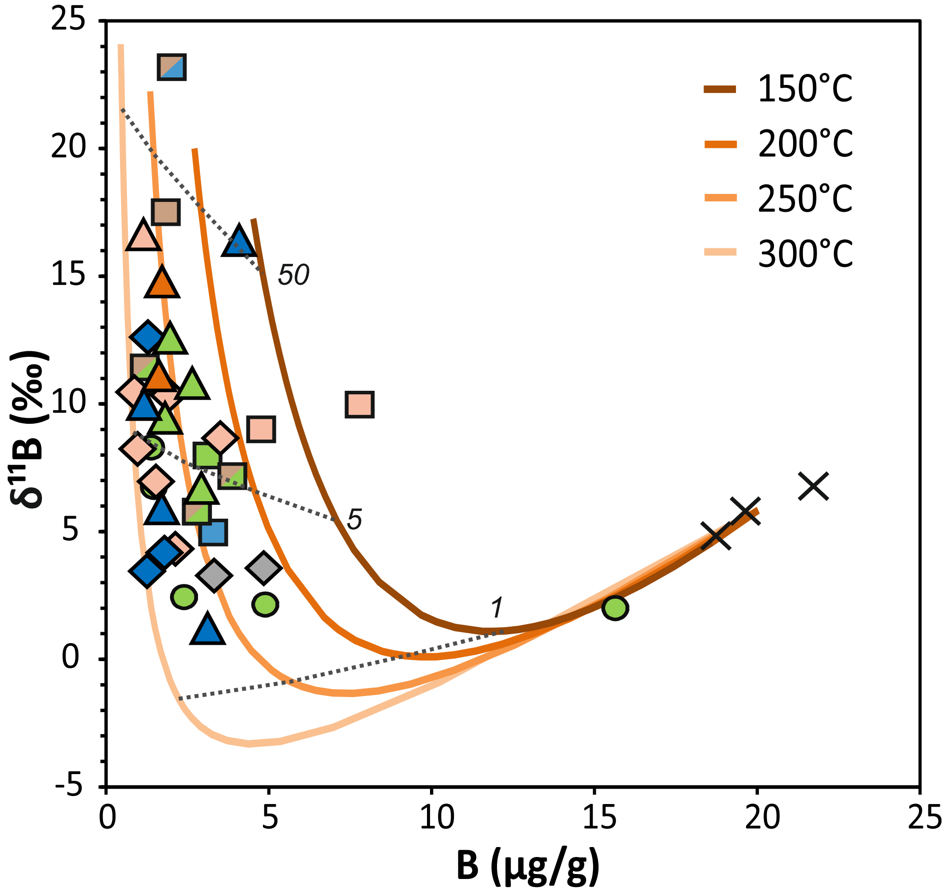

Fig. 8

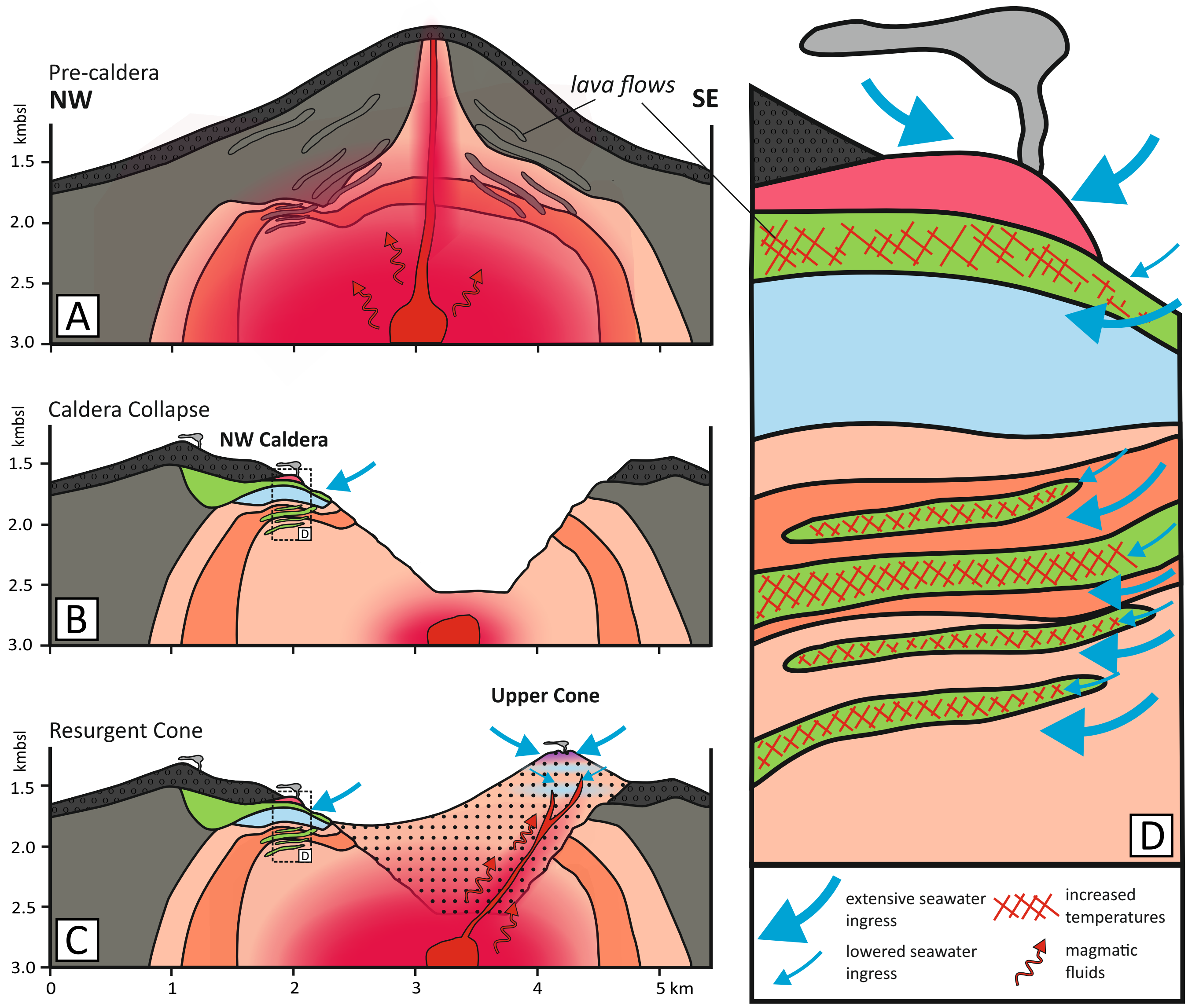

Pre-caldera
NW
SE
lava flows
kmbsl
1.5
2.0
2.5
3.0
A
Caldera Collapse
NW Caldera
D
B
Upper Cone
Resurgent Cone
C
0
1
2
3
4
5 km
D
extensive seawater ingress
lowered seawater ingress
increased temperatures
magmatic fluids

Table 1: Alteration types, secondary mineral assemblages, B concentrations and isotopic compositions of unaltered and altered rocks from Snowcap, Manus Basin.

sample name	alteration type*	depth (mbsf) top	bottom	secondary mineral assemblage**	B µg/g	$\delta^{11}B$ ‰	2sd ‰
193-U1188A-7R-1W, 145-147	prl-rich	49.65	49.67	anh (crs, py, prl, qtz)	7.8	10.0	0.1
193-U1188A-10R-1W, 35-37	prl-rich	77.65	77.67	qtz, crs (prl, ba, py)	4.8	9.0	0.1
193-U1188A-20R-1W, 46-47	mgt-ill-rich	174.36	174.37	qtz (plg, anh, crr, mgt, ill, py)	2.0	23.2	0.1
193-U1188A-21R-1W, 20-21	mgt-rich	183.30	183.31	qtz (plg, mgt, crr, py)	1.9	17.5	0.1
193-U1188F-16Z-1W, 139-141	ill-rich	256.29	256.31	qtz (py, ill, brittle mica, anh)	3.3	5.0	0.1
193-U1188F-26Z-1W, 20-23	chl-rich	300.03	300.06	qtz (anh, py, ill, chl, chl-mixed-layer, smc)	3.1	8.0	0.1
193-U1188F-31Z-1W, 1-3	mgt-chl-rich	322.61	322.63	qtz, plg (chl, mgt, py, anh)	1.2	11.4	0.1
193-U1188F-34Z-1W, 40-41	mgt-chl-rich	336.80	336.81	plg, qtz (ill, chl, py, mgt, ill-mixed-layer)	3.9	7.2	0.1
193-U1188F-43Z-1W, 90-91	mgt-chl-rich	372.40	372.41	qtz, plg (chl, anh, py, mgt)	2.8	5.8	0.1
SO-216-043-ROV10				fresh dacitic cap rock	21.7	6.8	0.1

* alteration types are described in the chapter "Sample Material", subchapter "Snowcap, Manus Basin".

**secondary mineral assemblages were identified by XRD and taken from Lackschewitz et al. (2006).

anh=anhydrite; ba=barite; chl=chlorite; crr=corrensite; crs=cristobalite; ill=illite; mgt=magnetite; plg=plagioclase; prl=pyrophyllite; py=pyrite; qtz=quartz; smc=smectite

Table 1: Alteration types, secondary mineral assemblages, B concentratio

sample name	alteration type*	depth (mbsf) top	bottom
193-U1188A-7R-1W, 145-147	prl-rich	49.65	49.67
193-U1188A-10R-1W, 35-37	prl-rich	77.65	77.67
193-U1188A-20R-1W, 46-47	mgt-ill-rich	174.36	174.37
193-U1188A-21R-1W, 20-21	mgt-rich	183.30	183.31
193-U1188F-16Z-1W, 139-141	ill-rich	256.29	256.31
193-U1188F-26Z-1W, 20-23	chl-rich	300.03	300.06
193-U1188F-31Z-1W, 1-3	mgt-chl-rich	322.61	322.63
193-U1188F-34Z-1W, 40-41	mgt-chl-rich	336.80	336.81
193-U1188F-43Z-1W, 90-91	mgt-chl-rich	372.40	372.41
SO-216-043-ROV10			

* alteration types are described in the chapter "Sample Material", subcha

**secondary mineral assemblages were identified by XRD and taken from

anh=anhydrite; ba=barite; chl=chlorite; crr=corrensite; crs=cristobalite; i ns and isotopic compositions of fresh and altered rocks from Snowcap, Manus Basin.

secondary mineral assemblage**	B µg/g	$\delta^{11}B$ ‰	2sd ‰
anh (crs, py, prl, qtz)	7.8	10.0	0.1
qtz, crs (prl, ba, py)	4.8	9.0	0.1
qtz (plg, anh, crr, mgt, ill, py)	2.0	23.2	0.1
qtz (plg, mgt, crr, py)	1.9	17.5	0.1
qtz (py, ill, brittle mica, anh)	3.3	5.0	0.1
qtz (anh, py, ill, chl, chl-mixed-layer, smc)	3.1	8.0	0.1
qtz, plg (chl, mgt, py, anh)	1.2	11.4	0.1
plg, qtz (ill, chl, py, mgt, ill-mixed-layer)	3.9	7.2	0.1
qtz, plg (chl, anh, py, mgt)	2.8	5.8	0.1
fresh dacitic cap rock	21.7	6.8	0.1

ɔter "Snowcap, Manus Basin"
Lackschewitz et al. (2006)

ll=illite; mgt=magnetite; plg=plagioclase; prl=pyrophyllite; py=pyrite; qtz=quartz; smc=smectite

Table 2: Alteration types, and B and Sr concentrations and isotopic compositions of altered and unaltered classified rocks from Brothers volcano, Kermadec arc.

sample name	alteration type*	depth (mbsf) top	bottom	B† μg/g	Sr† μg/g	$\delta^{11}B$ ‰	2sd ‰	$^{87}Sr/^{86}Sr$ ($2sd_{mean}$)
altered rock samples								
376-U1527C-								
11R-1W, 17-18	chl-rich	185.37	185.38	15.6	191	2.0	0.1	0.704621(9)†
11R-1W, 143-145	chl-rich	186.63	186.65	4.9	179			
11R-2W, 108-110	chl-rich	187.74	187.76	2.2	187			
11R-3W, 8-12	chl-rich	188.06	188.10	4.9	204	2.1	0.1	0.704336(4)
12R-1W, 142-144	chl-rich	196.22	196.24	2.4	222			0.704286(15)†
13R-1W, 65-68	chl-rich	200.25	200.28	2.2	205			
13R-3W, 50-52 GREEN	chl-rich	202.87	202.89	2.4	254	2.4	0.1	0.704208(4)
13R-3W, 50-52 YELLOW	chl-rich	202.87	202.89	3.5	216			0.704202(6)
14R-1W, 32-34	chl-rich	204.72	204.74	1.8	241			
14R-1W, 55-58	chl-rich	204.95	204.98	1.8	234			
14R-2W, 47-50	chl-rich	205.64	205.67	2.1	247			
14R-3W, 45-49 CLAST	chl-rich	207.01	207.05	1.6	242			
14R-3W, 45-49 MATRIX	chl-rich	207.01	207.05	2.0	223			
15R-2W, 43-50 MIX	chl-rich	211.02	211.09	2.2	222			
15R-2W, 43-50 CLAST	chl-rich	211.02	211.09	2.3	249			
15R-3W, 3-6	chl-rich	212.12	212.15	1.9	240			
17R-2W, 45-49	chl-rich	220.60	220.64	1.5	213			
18R-1W,60-63	chl-rich	224.20	224.23	1.4		8.3	0.1	
18R-2W, 52-56	chl-rich	225.51	225.55	1.5	200	6.8	0.1	0.704190(5)
18R-2W, 97-99	chl-rich	225.96	225.98	1.7	188			
19R-1W, 71-75	chl-rich	229.11	229.15	1.4	72			0.704536(13)†
19R-1W, 117-120 CLAST	chl-rich	229.57	229.60	2.3	209			
19R-1W, 117-120 MATRIX	chl-rich	229.57	229.60	1.5	121			
20R-1W, 40-43	chl-rich	233.60	233.63	1.4	210			
376-U1528A-								
7R-1W, 21-23 CLAST	prl-rich	45.21	45.23	3.5	127	8.7	0.1	0.704688(9)†
7R-1W, 21-23 MATRIX	prl-rich	45.21	45.23	1.5	189	7.0	0.1	0.704935(18)†
9R-2W, 97-99 CORE	ill-rich	57.07	57.09	1.3	147	12.6	0.1	0.704555(9)†
9R-2W, 97-99 HALO	prl-rich	57.07	57.09	0.9	430	10.5	0.1	0.705622(11)†
13R-1W, 57-59	prl-rich	74.37	74.39	1.9	138	10.4	0.1	0.704898(5)
14R-1W, 53-56 CORE	ill-rich	79.13	79.16	1.3	169			
376-U1528D-								
3R-1W, 75-77	prl-rich	66.85	66.87	1.0	215	8.3	0.1	0.706188(6)
4R-2W, 28-31 CLAST	prl-rich	72.64	72.75	0.8	222			
4R-2W, 28-31 MATRIX	ill-rich	72.64	72.75	1.4	213			
10R-2W, 16-18 HALO	prl-rich	101.72	101.74	0.9	424			
11R-1W, 100-102	ill-rich	105.90	105.92	1.3	220	3.5	0.1	0.704721(5)
11R-3W, 44-46 CORE	ill-rich	108.33	108.35	1.8	340			
11R-3W, 44-46 HALO	prl-rich	108.33	108.35	1.3	206			
14R-1W, 80-82	ill-rich	120.10	120.12	1.0	226			
16R-1W, 48-50 MATRIX	ill-rich	129.38	129.40	1.1	196			
16R-1W, 48-50 CLAST	prl-rich	129.38	129.40	0.8	235			
21R-1W, 16-18	ill-rich	153.06	153.08	1.8	148	4.2	0.1	0.705048(5)
23R-1W, 61-63	prl-rich	163.11	163.13	0.8	232			
29R-1W, 65-67	prl-rich	191.95	191.97	2.0	150			
45R-1W, 52-54	prl-rich	268.62	268.64	0.9	271			
46R-1W, 32-34 CORE	weakly altered	273.22	273.24	4.8	189	3.6	0.1	0.704191(19)†
46R-1W, 32-34 HALO	prl-rich	273.22	273.24	3.9	190			
49R-1W, 19-21	prl-rich	287.49	287.51	1.5	174			
51R-1W, 60-62	prl-rich	297.50	297.52	1.0	213			
51R-1W, 60-62 (replicate)	prl-rich	297.50	297.52	1.8	194			
55R-1W, 51-53	prl-rich	316.61	316.63	0.8	169			
57R-1W, 15-18 CORE	weakly altered	325.85	325.88	3.3	192	3.3	0.1	0.704227(14)†
57R-1W, 15-18 HALO	prl-rich	325.85	325.88	2.1	203	4.3	0.1	0.704383(6)
376-U1530A-								
3R-1W, 60-62	stockwork	17.50	17.52	1.6	297			
4R-1W, 67-69	stockwork	22.07	22.09	1.6	766			0.706376(5)
8R-1W, 19-21	chl-rich (sandstone)	40.49	40.51	4.4	15			0.705059(7)
12R-2W, 8-11	chl-rich (lava flow)	61.08	61.11	2.7	87	10.8	0.1	0.706809(7)
13R-1W, 100-102	ill-rich	65.30	65.32	4.1	84	16.4	0.1	0.706982(13)†
15R-2W, 43-45	ill-rich	75.78	75.85	5.2	124			
20R-1W, 24-26	ill-rich	98.14	98.16	1.2	29	10.0	0.1	0.706354(8)

25R-1W, 43-45	ill-rich	122.33	122.35	2.5	21			
26R-1W, 41-43 CLAST	ill-rich	127.11	127.13	3.1	39	1.2	0.1	0.706436(14)[†]
26R-1W, 41-43 MATRIX	ill-rich	127.11	127.13	1.7	19	5.9	0.1	0.705929(17)[†]
29R-1W, 22-24	ill-rich	141.32	141.34	1.9	42			
39R-1W, 6-8	prl-rich	189.16	189.18	2.0	58			
39R-2W, 78-80	prl-rich	191.38	191.40	1.2	45	16.7	0.1	0.705990(6)
39R-2W, 78-80 (replicate)	prl-rich	191.38	191.40					0.706007(14)[†]
48R-1W, 45-47	prl-dsp-rich	232.75	232.77	1.3	214			0.706301(7)
55R-1W, 137-139	prl-dsp-rich	267.27	267.29	1.7	91	14.8	0.1	0.706145(3)
56R-2W, 40-42	prl-dsp-rich	272.40	272.42	1.6	240			
57R-1W, 57-59	prl-dsp-rich	276.07	276.09	1.6	284	11.1	0.1	0.706962(14)
60R-1W, 96-98	chl-rich (lava flow)	290.86	290.88	2.0	16	12.6	0.1	0.704763(7)
64R-1W, 73-75	prl-dsp-rich	309.83	309.85	2.3	79			
76R-1W, 36-38	prl-rich	367.06	367.08	1.2	170			0.706326(15)[†]
81R-1W, 41-44	chl-rich (lava flow)	391.11	391.14	1.8	77	9.5	0.1	0.706072(25)[†]
82R-1W, 38-40	prl-rich	395.88	395.90	1.7	81			
83R-1W, 49-51	chl-rich (lava flow)	400.79	400.81	2.9	68	6.7	0.1	0.705891(17)[†]
88R-1W, 42-45	prl-rich	424.72	424.75	1.1	20			
				B	**Sr**	**$\delta^{11}B$**	**2sd**	**$^{87}Sr/^{86}Sr(2sd_{mean})$**
petrographic unaltered rock samples				μg/g	μg/g	‰	‰	
376-U1527A-6R-1W,71-78		49.21	49.28		215[◊]			
376-U1528D-21R-1W,75-79		153.65	153.69		202[◊]			
	water depth [m]	**Latitude**	**Longitude**					
SO-253-045-7R (Lower Cone)	1317	34° 52.730' S	179° 04.266' E	18.7	232[Δ]	4.8	0.1	0.703970(4)
SO-253-081-10B (NW Caldera)	1580	34° 51.659' S	179° 03.438' E	19.6	229[Δ]	5.8	0.1	0.704109(6)[Δ]

*alteration types are described in the chapter "Sample Material", subchapter "Brothers volcano, Kermadec Arc".

[†]measurements were performed at the PSO, Brest.

[◊]measurements were performed at the GEOMAR, Kiel.

[Δ]data were taken from Diehl (2019).

all measurements without special indications were performed at the MARUM, University of Bremen

mineral abbreviations: chl=chlorite; prl=pyrophyllite; ill=illite; dsp=diaspore

Table 2: Alteration types, B and Sr concentrations and B and Sr isotopic compositions of alte

sample name	alteration type*	depth (mbsf) top	bottom
altered rock samples			
376-U1527C-			
11R-1W, 17-18	chl-rich	185.37	185.38
11R-1W, 143-145	chl-rich	186.63	186.65
11R-2W, 108-110	chl-rich	187.74	187.76
11R-3W, 8-12	chl-rich	188.06	188.10
12R-1W, 142-144	chl-rich	196.22	196.24
13R-1W, 65-68	chl-rich	200.25	200.28
13R-3W, 50-52 GREEN	chl-rich	202.87	202.89
13R-3W, 50-52 YELLOW	chl-rich	202.87	202.89
14R-1W, 32-34	chl-rich	204.72	204.74
14R-1W, 55-58	chl-rich	204.95	204.98
14R-2W, 47-50	chl-rich	205.64	205.67
14R-3W, 45-49 CLAST	chl-rich	207.01	207.05
14R-3W, 45-49 MATRIX	chl-rich	207.01	207.05
15R-2W, 43-50 MIX	chl-rich	211.02	211.09
15R-2W, 43-50 CLAST	chl-rich	211.02	211.09
15R-3W, 3-6	chl-rich	212.12	212.15
17R-2W, 45-49	chl-rich	220.60	220.64
18R-1W,60-63	chl-rich	224.20	224.23
18R-2W, 52-56	chl-rich	225.51	225.55
18R-2W, 97-99	chl-rich	225.96	225.98
19R-1W, 71-75	chl-rich	229.11	229.15
19R-1W, 117-120 CLAST	chl-rich	229.57	229.60
19R-1W, 117-120 MATRIX	chl-rich	229.57	229.60
20R-1W, 40-43	chl-rich	233.60	233.63
376-U1528A-			
7R-1W, 21-23 CLAST	prl-rich	45.21	45.23
7R-1W, 21-23 MATRIX	prl-rich	45.21	45.23
9R-2W, 97-99 CORE	ill-rich	57.07	57.09
9R-2W, 97-99 HALO	prl-rich	57.07	57.09
13R-1W, 57-59	prl-rich	74.37	74.39
14R-1W, 53-56 CORE	ill-rich	79.13	79.16
376-U1528D-			
3R-1W, 75-77	prl-rich	66.85	66.87
4R-2W, 28-31 CLAST	prl-rich	72.64	72.75
4R-2W, 28-31 MATRIX	ill-rich	72.64	72.75
10R-2W, 16-18 HALO	prl-rich	101.72	101.74

	11R-1W, 100-102	ill-rich	105.90	105.92
	11R-3W, 44-46 CORE	ill-rich	108.33	108.35
	11R-3W, 44-46 HALO	prl-rich	108.33	108.35
	14R-1W, 80-82	ill-rich	120.10	120.12
	16R-1W, 48-50 MATRIX	ill-rich	129.38	129.40
	16R-1W, 48-50 CLAST	prl-rich	129.38	129.40
	21R-1W, 16-18	ill-rich	153.06	153.08
	23R-1W, 61-63	prl-rich	163.11	163.13
	29R-1W, 65-67	prl-rich	191.95	191.97
	45R-1W, 52-54	prl-rich	268.62	268.64
	46R-1W, 32-34 CORE	weakly altered	273.22	273.24
	46R-1W, 32-34 HALO	prl-rich	273.22	273.24
	49R-1W, 19-21	prl-rich	287.49	287.51
	51R-1W, 60-62	prl-rich	297.50	297.52
	51R-1W, 60-62 (replicate)	prl-rich	297.50	297.52
	55R-1W, 51-53	prl-rich	316.61	316.63
	57R-1W, 15-18 CORE	weakly altered	325.85	325.88
	57R-1W, 15-18 HALO	prl-rich	325.85	325.88
	376-U1530A-			
58	3R-1W, 60-62	stockwork	17.50	17.52
59	4R-1W, 67-69	stockwork	22.07	22.09
60	8R-1W, 19-21	chl-rich (sandstone)	40.49	40.51
61	12R-2W, 8-11	chl-rich (lava flow)	61.08	61.11
62	13R-1W, 100-102	ill-rich	65.30	65.32
63	15R-2W, 43-45	ill-rich	75.78	75.85
64	20R-1W, 24-26	ill-rich	98.14	98.16
65	25R-1W, 43-45	ill-rich	122.33	122.35
66	26R-1W, 41-43 CLAST	ill-rich	127.11	127.13
67	26R-1W, 41-43 MATRIX	ill-rich	127.11	127.13
68	29R-1W, 22-24	ill-rich	141.32	141.34
69	39R-1W, 6-8	prl-rich	189.16	189.18
70	39R-2W, 78-80	prl-rich	191.38	191.40
70	39R-2W, 78-80 (replicate)	prl-rich	191.38	191.40
71	48R-1W, 45-47	prl-dsp-rich	232.75	232.77
72	55R-1W, 137-139	prl-dsp-rich	267.27	267.29
73	56R-2W, 40-42	prl-dsp-rich	272.40	272.42
74	57R-1W, 57-59	prl-dsp-rich	276.07	276.09
75	60R-1W, 96-98	chl-rich (lava flow)	290.86	290.88
76	64R-1W, 73-75	prl-dsp-rich	309.83	309.85
77	76R-1W, 36-38	prl-rich	367.06	367.08
78	81R-1W, 41-44	chl-rich (lava flow)	391.11	391.14
79	82R-1W, 38-40	prl-rich	395.88	395.90
80	83R-1W, 49-51	chl-rich (lava flow)	400.79	400.81

81	88R-1W, 42-45	prl-rich	424.72	424.75
	petrographic unaltered rock samples			
	376-U1527A-6R-1W,71-78		49.21	49.28
	376-U1528D-21R-1W,75-79		153.65	153.69
		water depth [m]	**Latitude**	**Longitude**
	SO-253-045-7R (Lower Cone)	1317	34° 52.730' S	179° 04.266' E
	SO-253-081-10B (NW Caldera)	1580	34° 51.659' S	179° 03.438' E

*alteration types are described in the chapter "Sample Material", subchapter "Brothers volca

[†]measurements were performed at the PSO, Brest

[◊]measurements were performed at the GEOMAR, Kiel

[Δ]data were taken from Diehl (2019)

all measurements without special indications were performed at the MARUM, University of

mineral abbreviations: chl=chlorite; prl=pyrophyllite; ill=illite; dsp=diaspore ered and unaltered classified rocks based on petrographic characteristics from Brothers volcano, Kerr

B†	Sr†	$\delta^{11}B$	2sd	$^{87}Sr/^{86}Sr$ (2sd)
μg/g	μg/g	‰	‰	
15.6	191	2.0	0.1	0.704621(9)†
4.9	179			
2.2	187			
4.9	204	2.1	0.1	0.704336(4)
2.4	222			0.704286(15)†
2.2	205			
2.4	254	2.4	0.1	0.704208(4)
3.5	216			0.704202(6)
1.8	241			
1.8	234			
2.1	247			
1.6	242			
2.0	223			
2.2	222			
2.3	249			
1.9	240			
1.5	213			
1.4		8.3	0.1	
1.5	200	6.8	0.1	0.704190(5)
1.7	188			
1.4	72			0.704536(13)†
2.3	209			
1.5	121			
1.4	210			
3.5	127	8.7	0.1	0.704688(9)†
1.5	189	7.0	0.1	0.704935(18)†
1.3	147	12.6	0.1	0.704555(9)†
0.9	430	10.5	0.1	0.705622(11)†
1.9	138	10.4	0.1	0.704898(5)
1.3	169			
1.0	215	8.3	0.1	0.706188(6)
0.8	222			
1.4	213			
0.9	424			

1.3	220	3.5	0.1	0.704721(5)
1.8	340			
1.3	206			
1.0	226			
1.1	196			
0.8	235			
1.8	148	4.2	0.1	0.705048(5)
0.8	232			
2.0	150			
0.9	271			
4.8	189	3.6	0.1	0.704191(19)†
3.9	190			
1.5	174			
1.0	213			
1.8	194			
0.8	169			
3.3	192	3.3	0.1	0.704227(14)†
2.1	203	4.3	0.1	0.704383(6)

1.6	297			
1.6	766			0.706376(5)
4.4	15			0.705059(7)
2.7	87	10.8	0.1	0.706809(7)
4.1	84	16.4	0.1	0.706982(13)†
5.2	124			
1.2	29	10.0	0.1	0.706354(8)
2.5	21			
3.1	39	1.2	0.1	0.706436(14)†
1.7	19	5.9	0.1	0.705929(17)†
1.9	42			
2.0	58			
1.2	45	16.7	0.1	0.705990(6)
				0.706007(14)†
1.3	214			0.706301(7)
1.7	91	14.8	0.1	0.706145(3)
1.6	240			
1.6	284	11.1	0.1	0.706962(14)
2.0	16	12.6	0.1	0.704763(7)
2.3	79			
1.2	170			0.706326(15)†
1.8	77	9.5	0.1	0.706072(25)†
1.7	81			
2.9	68	6.7	0.1	0.705891(17)†

1.1 20

B	Sr	$\delta^{11}B$	2sd	$^{87}Sr/^{86}Sr$(2sd)
µg/g	µg/g	‰	‰	
	215$^{\lozenge}$			
	202$^{\lozenge}$			
18.7	232$^{\Delta}$	4.8	0.1	0.703970(4)
19.6	229$^{\Delta}$	5.8	0.1	0.704109(6)$^{\Delta}$

ano, Kermadec Arc"

Bremen

nadec arc.

Table 3: Oxygen isotope ratios ($\delta^{18}O_{VSMOW}$) measured by SIMS of quartz single crystal domains from Hole U1530A, NW Caldera, Brothers volcano.

Host rock		**depth (mbsf)**		**quartz separate**			**$\delta^{18}O_{VSMOW}$**	**2sd**	**temperature (°C)†**	
sample name	**alteration type***	**top**	**bottom**	**grain No.**	**point No.**	**description**	**(‰)**	**(‰)**	**$\delta^{18}O_{water}$ = 0 ‰◊**	**= +1 ‰◊**
376-U1530A-										
4R-1W, 67-69	stockwork	22.07	22.09	LSM1-17	1	vein infill	9.2	0.2	278	303
4R-1W, 67-69	stockwork	22.07	22.09	LSM1-17	2	vein infill	8.8	0.2	286	311
4R-1W, 67-69	stockwork	22.07	22.09	LSM1-18	1	vein infill	8.7	0.2	289	315
12R-2W, 8-11	chl-rich (lava flow)	61.08	61.11	LSM1-14	1	vug infill	9.6	0.2	269	292
12R-2W, 8-11	chl-rich (lava flow)	61.08	61.11	LSM1-14	2	vug infill	8.4	0.2	296	323
12R-2W, 8-11	chl-rich (lava flow)	61.08	61.11	LSM1-14	3	vug infill	9.1	0.2	280	305
12R-2W, 8-11	chl-rich (lava flow)	61.08	61.11	LSM1-14	4	vug infill	6.3	0.2	359	396
12R-2W, 8-11	chl-rich (lava flow)	61.08	61.11	LSM1-14	5	vug infill	7.1	0.2	330	363
12R-2W, 8-11	chl-rich (lava flow)	61.08	61.11	LSM1-14	6	vug infill	6.1	0.2	364	403
12R-2W, 8-11	chl-rich (lava flow)	61.08	61.11	LSM1-14	7	vug infill	7.6	0.2	317	347
12R-2W, 8-11	chl-rich (lava flow)	61.08	61.11	LSM1-14	8	vug infill	7.8	0.2	313	342
12R-2W, 8-11	chl-rich (lava flow)	61.08	61.11	LSM1-14	9	vug infill	6.0	0.2	366	405
12R-2W, 8-11	chl-rich (lava flow)	61.08	61.11	LSM1-14	10	vug infill	5.9	0.2	370	410
12R-2W, 8-11	chl-rich (lava flow)	61.08	61.11	LSM1-16	1	vug infill	5.6	0.1	383	425
12R-2W, 8-11	chl-rich (lava flow)	61.08	61.11	LSM1-16	2	vug infill	6.3	0.1	358	395
12R-2W, 8-11	chl-rich (lava flow)	61.08	61.11	LSM1-16	3	vug infill	6.1	0.1	363	402
12R-2W, 8-11	chl-rich (lava flow)	61.08	61.11	LSM1-16	4	vug infill	7.8	0.1	311	340
12R-2W, 8-11	chl-rich (lava flow)	61.08	61.11	LSM1-16	5	vug infill	5.8	0.1	374	415
12R-2W, 8-11	chl-rich (lava flow)	61.08	61.11	LSM1-16	6	vug infill	6.0	0.1	368	407
12R-2W, 8-11	chl-rich (lava flow)	61.08	61.11	LSM1-16	7	vug infill	6.3	0.1	358	395
12R-2W, 8-11	chl-rich (lava flow)	61.08	61.11	LSM1-16	8	vug infill	7.3	0.1	325	357
12R-2W, 8-11	chl-rich (lava flow)	61.08	61.11	LSM1-16	9	vug infill	7.6	0.1	317	347
12R-2W, 8-11	chl-rich (lava flow)	61.08	61.11	LSM1-16	10	vug infill	6.6	0.2	348	384
56R-2W, 40-42	prl-dsp-rich	272.40	272.42	LSM1-3	1	vein infill	7.4	0.1	322	354
56R-2W, 40-42	prl-dsp-rich	272.40	272.42	LSM1-3	2	vein infill	7.3	0.1	326	358
56R-2W, 40-42	prl-dsp-rich	272.40	272.42	LSM1-10	1	vein infill	6.8	0.1	342	376
56R-2W, 40-42	prl-dsp-rich	272.40	272.42	LSM1-10	2	vein infill	7.9	0.1	308	337
57R-1W, 57-59	prl-dsp-rich	276.07	276.09	LSM1-1	1	matrix replacement	8.5	0.1	294	320
57R-1W, 57-59	prl-dsp-rich	276.07	276.09	LSM1-1	2	matrix replacement	8.5	0.1	293	320
57R-1W, 57-59	prl-dsp-rich	276.07	276.09	LSM1-2	1	matrix replacement	7.5	0.1	320	351
57R-1W, 57-59	prl-dsp-rich	276.07	276.09	LSM1-2	2	matrix replacement	7.9	0.1	310	339
57R-1W, 57-59	prl-dsp-rich	276.07	276.09	LSM1-2	3	matrix replacement	7.8	0.1	313	342
57R-1W, 57-59	prl-dsp-rich	276.07	276.09	LSM1-2	4	matrix replacement	8.7	0.1	289	315
57R-1W, 57-59	prl-dsp-rich	276.07	276.09	LSM1-2	5	matrix replacement	8.6	0.1	291	317
60R-1W, 96-98	chl-rich (lava flow)	290.86	290.88	LSM1-4	1	vug infill	7.0	0.1	334	367
60R-1W, 96-98	chl-rich (lava flow)	290.86	290.88	LSM1-4	2	vug infill	7.0	0.1	335	368
60R-1W, 96-98	chl-rich (lava flow)	290.86	290.88	LSM1-4	3	vug infill	6.6	0.1	346	381
60R-1W, 96-98	chl-rich (lava flow)	290.86	290.88	LSM1-4	4	vug infill; point close to crack	8.7	0.1	289	315
60R-1W, 96-98	chl-rich (lava flow)	290.86	290.88	LSM1-4	5	vug infill	6.3	0.1	359	397
60R-1W, 96-98	chl-rich (lava flow)	290.86	290.88	LSM1-4	6	vug infill	6.6	0.1	348	384
60R-1W, 96-98	chl-rich (lava flow)	290.86	290.88	LSM1-4	7	vug infill	6.6	0.1	347	383
60R-1W, 96-98	chl-rich (lava flow)	290.86	290.88	LSM1-4	8	vug infill	6.3	0.1	356	393
60R-1W, 96-98	chl-rich (lava flow)	290.86	290.88	LSM1-4	9	vug infill	6.2	0.1	360	398
60R-1W, 96-98	chl-rich (lava flow)	290.86	290.88	LSM1-4	10	vug infill	6.6	0.1	347	383
60R-1W, 96-98	chl-rich (lava flow)	290.86	290.88	LSM1-5	1	vug infill	6.3	0.1	358	396
60R-1W, 96-98	chl-rich (lava flow)	290.86	290.88	LSM1-5	2	vug infill	6.7	0.1	343	378
60R-1W, 96-98	chl-rich (lava flow)	290.86	290.88	LSM1-5	3	vug infill	6.4	0.1	355	391
60R-1W, 96-98	chl-rich (lava flow)	290.86	290.88	LSM1-5	4	vug infill	6.3	0.1	356	394
60R-1W, 96-98	chl-rich (lava flow)	290.86	290.88	LSM1-5	5	vug infill	6.8	0.1	341	375
60R-1W, 96-98	chl-rich (lava flow)	290.86	290.88	LSM1-5	6	vug infill	6.2	0.1	361	399
60R-1W, 96-98	chl-rich (lava flow)	290.86	290.88	LSM1-5	7	vug infill	6.9	0.1	339	373
60R-1W, 96-98	chl-rich (lava flow)	290.86	290.88	LSM1-5	8	vug infill	6.4	0.1	355	392
60R-1W, 96-98	chl-rich (lava flow)	290.86	290.88	LSM1-5	9	vug infill	6.2	0.1	362	400
60R-1W, 96-98	chl-rich (lava flow)	290.86	290.88	LSM1-5	10	vug infill	6.3	0.1	357	394
64R-1W, 73-75	prl-dsp-rich	309.83	309.85	LSM1-11	1	vein infill	8.1	0.2	304	332
64R-1W, 73-75	prl-dsp-rich	309.83	309.85	LSM1-11	2	vein infill	8.7	0.2	288	314
64R-1W, 73-75	prl-dsp-rich	309.83	309.85	LSM1-11	3	vein infill	7.6	0.2	318	349
64R-1W, 73-75	prl-dsp-rich	309.83	309.85	LSM1-11	4	vein infill	7.4	0.2	323	354
64R-1W, 73-75	prl-dsp-rich	309.83	309.85	LSM1-11	5	vein infill	7.1	0.2	331	363
64R-1W, 73-75	prl-dsp-rich	309.83	309.85	LSM1-11	6	vein infill	7.2	0.2	329	361
64R-1W, 73-75	prl-dsp-rich	309.83	309.85	LSM1-11	7	vein infill	7.8	0.2	313	343
64R-1W, 73-75	prl-dsp-rich	309.83	309.85	LSM1-11	8	vein infill	6.8	0.2	342	377
64R-1W, 73-75	prl-dsp-rich	309.83	309.85	LSM1-11	9	vein infill	6.4	0.2	353	390
64R-1W, 73-75	prl-dsp-rich	309.83	309.85	LSM1-11	10	vein infill	7.8	0.2	312	341
64R-1W, 73-75	prl-dsp-rich	309.83	309.85	LSM1-12	1	vein infill; marginal diffusion?	7.5	0.2	319	350
64R-1W, 73-75	prl-dsp-rich	309.83	309.85	LSM1-12	2	vein infill	8.8	0.2	285	311
64R-1W, 73-75	prl-dsp-rich	309.83	309.85	LSM1-12	3	vein infill	8.6	0.2	291	318
64R-1W, 73-75	prl-dsp-rich	309.83	309.85	LSM1-12	4	vein infill	9.0	0.2	283	308
64R-1W, 73-75	prl-dsp-rich	309.83	309.85	LSM1-12	5	vein infill	9.0	0.2	282	307
64R-1W, 73-75	prl-dsp-rich	309.83	309.85	LSM1-12	6	vein infill	8.9	0.2	285	311
64R-1W, 73-75	prl-dsp-rich	309.83	309.85	LSM1-12	7	vein infill	8.6	0.2	290	316
64R-1W, 73-75	prl-dsp-rich	309.83	309.85	LSM1-12	8	vein infill	8.9	0.2	284	310
64R-1W, 73-75	prl-dsp-rich	309.83	309.85	LSM1-12	9	vein infill	8.9	0.2	285	310
64R-1W, 73-75	prl-dsp-rich	309.83	309.85	LSM1-12	10	vein infill	8.8	0.2	285	311

64R-1W, 73-75	prl-dsp-rich	309.83	309.85	LSM1-12	11	vein infill	8.8	0.2	286	312
64R-1W, 73-75	prl-dsp-rich	309.83	309.85	LSM1-12	12	vein infill	8.6	0.2	290	316
64R-1W, 73-75	prl-dsp-rich	309.83	309.85	LSM1-12	13	vein infill	8.9	0.2	285	310
64R-1W, 73-75	prl-dsp-rich	309.83	309.85	LSM1-12	14	vein infill	9.0	0.2	281	305
64R-1W, 73-75	prl-dsp-rich	309.83	309.85	LSM1-12	15	vein infill	9.0	0.2	281	306
64R-1W, 73-75	prl-dsp-rich	309.83	309.85	LSM1-12	16	vein infill	8.9	0.2	285	310
64R-1W, 73-75	prl-dsp-rich	309.83	309.85	LSM1-12	17	vein infill	9.5	0.2	271	295
64R-1W, 73-75	prl-dsp-rich	309.83	309.85	LSM1-12	18	vein infill	9.5	0.2	271	295
64R-1W, 73-75	prl-dsp-rich	309.83	309.85	LSM1-12	19	vein infill	9.9	0.2	262	284
64R-1W, 73-75	prl-dsp-rich	309.83	309.85	LSM1-12	20	vein infill; marginal diffusion?	8.3	0.2	300	327
64R-1W, 73-75	prl-dsp-rich	309.83	309.85	LSM1-13	1	vein infill	8.9	0.2	284	309
64R-1W, 73-75	prl-dsp-rich	309.83	309.85	LSM1-13	2	vein infill	9.1	0.2	279	304
64R-1W, 73-75	prl-dsp-rich	309.83	309.85	LSM1-13	3	vein infill	9.0	0.2	282	307
64R-1W, 73-75	prl-dsp-rich	309.83	309.85	LSM1-13	4	vein infill	8.8	0.2	286	312
64R-1W, 73-75	prl-dsp-rich	309.83	309.85	LSM1-13	5	vein infill	8.9	0.2	285	310
64R-1W, 73-75	prl-dsp-rich	309.83	309.85	LSM1-13	6	vein infill	8.9	0.2	284	309
64R-1W, 73-75	prl-dsp-rich	309.83	309.85	LSM1-13	7	vein infill	9.2	0.2	278	303
64R-1W, 73-75	prl-dsp-rich	309.83	309.85	LSM1-13	8	vein infill	9.0	0.2	281	306
64R-1W, 73-75	prl-dsp-rich	309.83	309.85	LSM1-13	9	vein infill	9.4	0.2	273	297
64R-1W, 73-75	prl-dsp-rich	309.83	309.85	LSM1-13	10	vein infill	9.5	0.2	269	293
64R-1W, 73-75	prl-dsp-rich	309.83	309.85	LSM1-13	11	vein infill	7.3	0.2	325	356
64R-1W, 73-75	prl-dsp-rich	309.83	309.85	LSM1-13	12	vein infill	7.2	0.2	329	362
64R-1W, 73-75	prl-dsp-rich	309.83	309.85	LSM1-13	13	vein infill	8.1	0.2	305	333
64R-1W, 73-75	prl-dsp-rich	309.83	309.85	LSM1-13	14	vein infill	8.0	0.2	307	336
64R-1W, 73-75	prl-dsp-rich	309.83	309.85	LSM1-13	15	vein infill	7.0	0.2	334	367
64R-1W, 73-75	prl-dsp-rich	309.83	309.85	LSM1-13	16	vein infill	6.8	0.2	341	375
64R-1W, 73-75	prl-dsp-rich	309.83	309.85	LSM1-13	17	vein infill	6.7	0.2	345	380
64R-1W, 73-75	prl-dsp-rich	309.83	309.85	LSM1-13	18	vein infill	6.7	0.2	343	378
64R-1W, 73-75	prl-dsp-rich	309.83	309.85	LSM1-13	19	vein infill	7.7	0.2	313	343
64R-1W, 73-75	prl-dsp-rich	309.83	309.85	LSM1-13	20	vein infill	7.1	0.2	332	365

*alteration types are described in the chapter "Sample Material", subchapter "Brothers volcano, Kermdec Arc".

†temperatures were calculated based on the equation given by Sharp & Kirschner (1994).

◊minimum and maximum measured $\delta^{18}O$ hydrothermal fluid compositions at the NW Caldera of Brothers volcano after deRonde et al. (2011).

Table 3: Oxygen isotope measurements ($\delta^{18}O_{VSMOW}$) for quartz separates of Hole U1530A, NW Ca

Host rock		**depth (mbsf)**		**quartz separate**	
sample name	**alteration type***	**top**	**bottom**	**grain No.**	**point No.**
376-U1530A-					
4R-1W, 67-69	stockwork	22.07	22.09	LSM1-17	1
4R-1W, 67-69	stockwork	22.07	22.09	LSM1-17	2
4R-1W, 67-69	stockwork	22.07	22.09	LSM1-18	1
12R-2W, 8-11	chl-rich (lava flow)	61.08	61.11	LSM1-14	1
12R-2W, 8-11	chl-rich (lava flow)	61.08	61.11	LSM1-14	2
12R-2W, 8-11	chl-rich (lava flow)	61.08	61.11	LSM1-14	3
12R-2W, 8-11	chl-rich (lava flow)	61.08	61.11	LSM1-14	4
12R-2W, 8-11	chl-rich (lava flow)	61.08	61.11	LSM1-14	5
12R-2W, 8-11	chl-rich (lava flow)	61.08	61.11	LSM1-14	6
12R-2W, 8-11	chl-rich (lava flow)	61.08	61.11	LSM1-14	7
12R-2W, 8-11	chl-rich (lava flow)	61.08	61.11	LSM1-14	8
12R-2W, 8-11	chl-rich (lava flow)	61.08	61.11	LSM1-14	9
12R-2W, 8-11	chl-rich (lava flow)	61.08	61.11	LSM1-14	10
12R-2W, 8-11	chl-rich (lava flow)	61.08	61.11	LSM1-16	1
12R-2W, 8-11	chl-rich (lava flow)	61.08	61.11	LSM1-16	2
12R-2W, 8-11	chl-rich (lava flow)	61.08	61.11	LSM1-16	3
12R-2W, 8-11	chl-rich (lava flow)	61.08	61.11	LSM1-16	4
12R-2W, 8-11	chl-rich (lava flow)	61.08	61.11	LSM1-16	5
12R-2W, 8-11	chl-rich (lava flow)	61.08	61.11	LSM1-16	6
12R-2W, 8-11	chl-rich (lava flow)	61.08	61.11	LSM1-16	7
12R-2W, 8-11	chl-rich (lava flow)	61.08	61.11	LSM1-16	8
12R-2W, 8-11	chl-rich (lava flow)	61.08	61.11	LSM1-16	9
12R-2W, 8-11	chl-rich (lava flow)	61.08	61.11	LSM1-16	10
56R-2W, 40-42	prl-dsp-rich	272.40	272.42	LSM1-3	1
56R-2W, 40-42	prl-dsp-rich	272.40	272.42	LSM1-3	2
56R-2W, 40-42	prl-dsp-rich	272.40	272.42	LSM1-10	1
56R-2W, 40-42	prl-dsp-rich	272.40	272.42	LSM1-10	2
57R-1W, 57-59	prl-dsp-rich	276.07	276.09	LSM1-1	1
57R-1W, 57-59	prl-dsp-rich	276.07	276.09	LSM1-1	2
57R-1W, 57-59	prl-dsp-rich	276.07	276.09	LSM1-2	1
57R-1W, 57-59	prl-dsp-rich	276.07	276.09	LSM1-2	2
57R-1W, 57-59	prl-dsp-rich	276.07	276.09	LSM1-2	3
57R-1W, 57-59	prl-dsp-rich	276.07	276.09	LSM1-2	4
57R-1W, 57-59	prl-dsp-rich	276.07	276.09	LSM1-2	5
60R-1W, 96-98	chl-rich (lava flow)	290.86	290.88	LSM1-4	1
60R-1W, 96-98	chl-rich (lava flow)	290.86	290.88	LSM1-4	2
60R-1W, 96-98	chl-rich (lava flow)	290.86	290.88	LSM1-4	3
60R-1W, 96-98	chl-rich (lava flow)	290.86	290.88	LSM1-4	4
60R-1W, 96-98	chl-rich (lava flow)	290.86	290.88	LSM1-4	5

60R-1W, 96-98	chl-rich (lava flow)	290.86	290.88	LSM1-4	6
60R-1W, 96-98	chl-rich (lava flow)	290.86	290.88	LSM1-4	7
60R-1W, 96-98	chl-rich (lava flow)	290.86	290.88	LSM1-4	8
60R-1W, 96-98	chl-rich (lava flow)	290.86	290.88	LSM1-4	9
60R-1W, 96-98	chl-rich (lava flow)	290.86	290.88	LSM1-4	10
60R-1W, 96-98	chl-rich (lava flow)	290.86	290.88	LSM1-5	1
60R-1W, 96-98	chl-rich (lava flow)	290.86	290.88	LSM1-5	2
60R-1W, 96-98	chl-rich (lava flow)	290.86	290.88	LSM1-5	3
60R-1W, 96-98	chl-rich (lava flow)	290.86	290.88	LSM1-5	4
60R-1W, 96-98	chl-rich (lava flow)	290.86	290.88	LSM1-5	5
60R-1W, 96-98	chl-rich (lava flow)	290.86	290.88	LSM1-5	6
60R-1W, 96-98	chl-rich (lava flow)	290.86	290.88	LSM1-5	7
60R-1W, 96-98	chl-rich (lava flow)	290.86	290.88	LSM1-5	8
60R-1W, 96-98	chl-rich (lava flow)	290.86	290.88	LSM1-5	9
60R-1W, 96-98	chl-rich (lava flow)	290.86	290.88	LSM1-5	10
64R-1W, 73-75	prl-dsp-rich	309.83	309.85	LSM1-11	1
64R-1W, 73-75	prl-dsp-rich	309.83	309.85	LSM1-11	2
64R-1W, 73-75	prl-dsp-rich	309.83	309.85	LSM1-11	3
64R-1W, 73-75	prl-dsp-rich	309.83	309.85	LSM1-11	4
64R-1W, 73-75	prl-dsp-rich	309.83	309.85	LSM1-11	5
64R-1W, 73-75	prl-dsp-rich	309.83	309.85	LSM1-11	6
64R-1W, 73-75	prl-dsp-rich	309.83	309.85	LSM1-11	7
64R-1W, 73-75	prl-dsp-rich	309.83	309.85	LSM1-11	8
64R-1W, 73-75	prl-dsp-rich	309.83	309.85	LSM1-11	9
64R-1W, 73-75	prl-dsp-rich	309.83	309.85	LSM1-11	10
64R-1W, 73-75	prl-dsp-rich	309.83	309.85	LSM1-12	1
64R-1W, 73-75	prl-dsp-rich	309.83	309.85	LSM1-12	2
64R-1W, 73-75	prl-dsp-rich	309.83	309.85	LSM1-12	3
64R-1W, 73-75	prl-dsp-rich	309.83	309.85	LSM1-12	4
64R-1W, 73-75	prl-dsp-rich	309.83	309.85	LSM1-12	5
64R-1W, 73-75	prl-dsp-rich	309.83	309.85	LSM1-12	6
64R-1W, 73-75	prl-dsp-rich	309.83	309.85	LSM1-12	7
64R-1W, 73-75	prl-dsp-rich	309.83	309.85	LSM1-12	8
64R-1W, 73-75	prl-dsp-rich	309.83	309.85	LSM1-12	9
64R-1W, 73-75	prl-dsp-rich	309.83	309.85	LSM1-12	10
64R-1W, 73-75	prl-dsp-rich	309.83	309.85	LSM1-12	11
64R-1W, 73-75	prl-dsp-rich	309.83	309.85	LSM1-12	12
64R-1W, 73-75	prl-dsp-rich	309.83	309.85	LSM1-12	13
64R-1W, 73-75	prl-dsp-rich	309.83	309.85	LSM1-12	14
64R-1W, 73-75	prl-dsp-rich	309.83	309.85	LSM1-12	15
64R-1W, 73-75	prl-dsp-rich	309.83	309.85	LSM1-12	16
64R-1W, 73-75	prl-dsp-rich	309.83	309.85	LSM1-12	17
64R-1W, 73-75	prl-dsp-rich	309.83	309.85	LSM1-12	18
64R-1W, 73-75	prl-dsp-rich	309.83	309.85	LSM1-12	19
64R-1W, 73-75	prl-dsp-rich	309.83	309.85	LSM1-12	20

64R-1W, 73-75	prl-dsp-rich	309.83	309.85	LSM1-13	1
64R-1W, 73-75	prl-dsp-rich	309.83	309.85	LSM1-13	2
64R-1W, 73-75	prl-dsp-rich	309.83	309.85	LSM1-13	3
64R-1W, 73-75	prl-dsp-rich	309.83	309.85	LSM1-13	4
64R-1W, 73-75	prl-dsp-rich	309.83	309.85	LSM1-13	5
64R-1W, 73-75	prl-dsp-rich	309.83	309.85	LSM1-13	6
64R-1W, 73-75	prl-dsp-rich	309.83	309.85	LSM1-13	7
64R-1W, 73-75	prl-dsp-rich	309.83	309.85	LSM1-13	8
64R-1W, 73-75	prl-dsp-rich	309.83	309.85	LSM1-13	9
64R-1W, 73-75	prl-dsp-rich	309.83	309.85	LSM1-13	10
64R-1W, 73-75	prl-dsp-rich	309.83	309.85	LSM1-13	11
64R-1W, 73-75	prl-dsp-rich	309.83	309.85	LSM1-13	12
64R-1W, 73-75	prl-dsp-rich	309.83	309.85	LSM1-13	13
64R-1W, 73-75	prl-dsp-rich	309.83	309.85	LSM1-13	14
64R-1W, 73-75	prl-dsp-rich	309.83	309.85	LSM1-13	15
64R-1W, 73-75	prl-dsp-rich	309.83	309.85	LSM1-13	16
64R-1W, 73-75	prl-dsp-rich	309.83	309.85	LSM1-13	17
64R-1W, 73-75	prl-dsp-rich	309.83	309.85	LSM1-13	18
64R-1W, 73-75	prl-dsp-rich	309.83	309.85	LSM1-13	19
64R-1W, 73-75	prl-dsp-rich	309.83	309.85	LSM1-13	20

*alteration types are described in the chapter "Sample Material", subchapter "Brothers volcan

†temperatures were calculated based on the equation given by Sharp & Kirschner (1994)

◊minimum and maximum measured δ^{18}O hydrothermal fluid compositions at the NW Caldera

aldera, Brothers volcano (point positions are given in the Appendix, Table A. 3-8).

description	$\delta^{18}O_{VSMOW}$ (‰)	2sd (‰)	temperature (°C)† $\delta^{18}O_{water}$ = 0 ‰◊	$\delta^{18}O_{water}$ = +1 ‰◊
vein infill	9.2	0.2	278	303
vein infill	8.8	0.2	286	311
vein infill	8.7	0.2	289	315
vug infill	9.6	0.2	269	292
vug infill	8.4	0.2	296	323
vug infill	9.1	0.2	280	305
vug infill	6.3	0.2	359	396
vug infill	7.1	0.2	330	363
vug infill	6.1	0.2	364	403
vug infill	7.6	0.2	317	347
vug infill	7.8	0.2	313	342
vug infill	6.0	0.2	366	405
vug infill	5.9	0.2	370	410
vug infill	5.6	0.1	383	425
vug infill	6.3	0.1	358	395
vug infill	6.1	0.1	363	402
vug infill	7.8	0.1	311	340
vug infill	5.8	0.1	374	415
vug infill	6.0	0.1	368	407
vug infill	6.3	0.1	358	395
vug infill	7.3	0.1	325	357
vug infill	7.6	0.1	317	347
vug infill	6.6	0.2	348	384
vein infill	7.4	0.1	322	354
vein infill	7.3	0.1	326	358
vein infill	6.8	0.1	342	376
vein infill	7.9	0.1	308	337
matrix replacement	8.5	0.1	294	320
matrix replacement	8.5	0.1	293	320
matrix replacement	7.5	0.1	320	351
matrix replacement	7.9	0.1	310	339
matrix replacement	7.8	0.1	313	342
matrix replacement	8.7	0.1	289	315
matrix replacement	8.6	0.1	291	317
vug infill	7.0	0.1	334	367
vug infill	7.0	0.1	335	368
vug infill	6.6	0.1	346	381
vug infill; point close to crack	8.7	0.1	289	315
vug infill	6.3	0.1	359	397

vug infill	6.6	0.1	348	384
vug infill	6.6	0.1	347	383
vug infill	6.3	0.1	356	393
vug infill	6.2	0.1	360	398
vug infill	6.6	0.1	347	383
vug infill	6.3	0.1	358	396
vug infill	6.7	0.1	343	378
vug infill	6.4	0.1	355	391
vug infill	6.3	0.1	356	394
vug infill	6.8	0.1	341	375
vug infill	6.2	0.1	361	399
vug infill	6.9	0.1	339	373
vug infill	6.4	0.1	355	392
vug infill	6.2	0.1	362	400
vug infill	6.3	0.1	357	394
vein infill	8.1	0.2	304	332
vein infill	8.7	0.2	288	314
vein infill	7.6	0.2	318	349
vein infill	7.4	0.2	323	354
vein infill	7.1	0.2	331	363
vein infill	7.2	0.2	329	361
vein infill	7.8	0.2	313	343
vein infill	6.8	0.2	342	377
vein infill	6.4	0.2	353	390
vein infill	7.8	0.2	312	341
vein infill; marginal diffusion?	7.5	0.2	319	350
vein infill	8.8	0.2	285	311
vein infill	8.6	0.2	291	318
vein infill	9.0	0.2	283	308
vein infill	9.0	0.2	282	307
vein infill	8.9	0.2	285	311
vein infill	8.6	0.2	290	316
vein infill	8.9	0.2	284	310
vein infill	8.9	0.2	285	310
vein infill	8.8	0.2	285	311
vein infill	8.8	0.2	286	312
vein infill	8.6	0.2	290	316
vein infill	8.9	0.2	285	310
vein infill	9.0	0.2	281	305
vein infill	9.0	0.2	281	306
vein infill	8.9	0.2	285	310
vein infill	9.5	0.2	271	295
vein infill	9.5	0.2	271	295
vein infill	9.9	0.2	262	284
vein infill; marginal diffusion?	8.3	0.2	300	327

vein infill	8.9	0.2	284	309
vein infill	9.1	0.2	279	304
vein infill	9.0	0.2	282	307
vein infill	8.8	0.2	286	312
vein infill	8.9	0.2	285	310
vein infill	8.9	0.2	284	309
vein infill	9.2	0.2	278	303
vein infill	9.0	0.2	281	306
vein infill	9.4	0.2	273	297
vein infill	9.5	0.2	269	293
vein infill	7.3	0.2	325	356
vein infill	7.2	0.2	329	362
vein infill	8.1	0.2	305	333
vein infill	8.0	0.2	307	336
vein infill	7.0	0.2	334	367
vein infill	6.8	0.2	341	375
vein infill	6.7	0.2	345	380
vein infill	6.7	0.2	343	378
vein infill	7.7	0.2	313	343
vein infill	7.1	0.2	332	365

o, Kermdec Arc"

of Brothers volcano after deRonde et al. (2011)

Table A1: Oxygen isotope measurements on quartz that were conducted by SIMS on sample m

spot number	spot name	host rock sample name
20200302@787.asc	LSM1 UWQ-1 g1	
20200302@788.asc	LSM1 UWQ-1 g1	
20200302@789.asc	LSM1 UWQ-1 g1	
20200302@790.asc	LSM1 UWQ-1 g1	
	average and 2SD	
20200302@791.asc	LSM1_4 spot-1	376-U1530A-60R-1W, 96-98
20200302@792.asc	LSM1_4 spot-2	376-U1530A-60R-1W, 96-98
20200302@793.asc	LSM1_4 spot-3	376-U1530A-60R-1W, 96-98
20200302@794.asc	LSM1_4 spot-4	376-U1530A-60R-1W, 96-98
20200302@795.asc	LSM1_4 spot-5	376-U1530A-60R-1W, 96-98
20200302@796.asc	LSM1_4 spot-6	376-U1530A-60R-1W, 96-98
20200302@797.asc	LSM1_4 spot-7	376-U1530A-60R-1W, 96-98
20200302@798.asc	LSM1_4 spot-8	376-U1530A-60R-1W, 96-98
20200302@799.asc	LSM1_4 spot-9	376-U1530A-60R-1W, 96-98
20200302@800.asc	LSM1_4 spot-10	376-U1530A-60R-1W, 96-98
20200302@801.asc	LSM1_5 spot-1	376-U1530A-60R-1W, 96-98
20200302@802.asc	LSM1_5 spot-2	376-U1530A-60R-1W, 96-98
20200302@803.asc	LSM1_5 spot-3	376-U1530A-60R-1W, 96-98
20200302@804.asc	LSM1_5 spot-4	376-U1530A-60R-1W, 96-98
20200302@805.asc	LSM1_5 spot-5	376-U1530A-60R-1W, 96-98
20200302@806.asc	LSM1_5 spot-6	376-U1530A-60R-1W, 96-98
20200302@807.asc	LSM1_5 spot-7	376-U1530A-60R-1W, 96-98
20200302@808.asc	LSM1_5 spot-8	376-U1530A-60R-1W, 96-98
20200302@809.asc	LSM1_5 spot-9	376-U1530A-60R-1W, 96-98
20200302@810.asc	LSM1_5 spot-10	376-U1530A-60R-1W, 96-98
20200302@811.asc	LSM1 UWQ-1 g1 CsRes=143	
20200302@812.asc	LSM1 UWQ-1 g1	
20200302@813.asc	LSM1 UWQ-1 g1	
20200302@814.asc	LSM1 UWQ-1 g1	
	average and 2SD	
	bracket average and 2SD	
20200302@815.asc	LSM1_11 spot-1	376-U1530A-64R-1W, 73-75
20200302@816.asc	LSM1_11 spot-2	376-U1530A-64R-1W, 73-75
20200302@817.asc	LSM1_11 spot-3	376-U1530A-64R-1W, 73-75
20200302@818.asc	LSM1_11 spot-4	376-U1530A-64R-1W, 73-75
20200302@819.asc	LSM1_11 spot-5	376-U1530A-64R-1W, 73-75
20200302@820.asc	LSM1_11 spot-6	376-U1530A-64R-1W, 73-75
20200302@821.asc	LSM1_11 spot-7	376-U1530A-64R-1W, 73-75
20200302@822.asc	LSM1_11 spot-8	376-U1530A-64R-1W, 73-75
20200302@823.asc	LSM1_11 spot-9	376-U1530A-64R-1W, 73-75
20200302@824.asc	LSM1_11 spot-10	376-U1530A-64R-1W, 73-75

20200302@825.asc	LSM1_14 spot-1	376-U1530A-12R-2W, 8-11
20200302@826.asc	LSM1_14 spot-2	376-U1530A-12R-2W, 8-11
20200302@827.asc	LSM1_14 spot-3	376-U1530A-12R-2W, 8-11
20200302@828.asc	LSM1_14 spot-4	376-U1530A-12R-2W, 8-11
20200302@829.asc	LSM1_14 spot-5	376-U1530A-12R-2W, 8-11
20200302@830.asc	LSM1_14 spot-6	376-U1530A-12R-2W, 8-11
20200302@831.asc	LSM1_14 spot-7	376-U1530A-12R-2W, 8-11
20200302@832.asc	LSM1_14 spot-8	376-U1530A-12R-2W, 8-11
20200302@833.asc	LSM1_14 spot-9	376-U1530A-12R-2W, 8-11
20200302@834.asc	LSM1_14 spot-10	376-U1530A-12R-2W, 8-11
20200302@835.asc	LSM1 UWQ-1 g1	
20200302@836.asc	LSM1 UWQ-1 g1	
20200302@837.asc	LSM1 UWQ-1 g1	
20200302@838.asc	LSM1 UWQ-1 g1	
	average and 2SD	
	bracket average and 2SD	
20200302@839.asc	LSM1_1 spot-1	376-U1530A-57R-1W, 57-59
20200302@840.asc	LSM1_1 spot-2	376-U1530A-57R-1W, 57-59
20200302@841.asc	LSM1_2 spot-1	376-U1530A-57R-1W, 57-59
20200302@842.asc	LSM1_2 spot-2	376-U1530A-57R-1W, 57-59
20200302@843.asc	LSM1_2 spot-3	376-U1530A-57R-1W, 57-59
20200302@844.asc	LSM1_2 spot-4	376-U1530A-57R-1W, 57-59
20200302@845.asc	LSM1_2 spot-5 CsRes=144	376-U1530A-57R-1W, 57-59
20200302@846.asc	LSM1_3 spot-1	376-U1530A-56R-2W, 40-42
20200302@847.asc	LSM1_3 spot-2	376-U1530A-56R-2W, 40-42
20200302@848.asc	LSM1_10 spot-1	376-U1530A-56R-2W, 40-42
20200302@849.asc	LSM1_10 spot-2	376-U1530A-56R-2W, 40-42
20200302@850.asc	LSM1_16 spot-1	376-U1530A-12R-2W, 8-11
20200302@851.asc	LSM1_16 spot-2	376-U1530A-12R-2W, 8-11
20200302@852.asc	LSM1_16 spot-3	376-U1530A-12R-2W, 8-11
20200302@853.asc	LSM1_16 spot-4	376-U1530A-12R-2W, 8-11
20200302@854.asc	LSM1_16 spot-5	376-U1530A-12R-2W, 8-11
20200302@855.asc	LSM1_16 spot-6	376-U1530A-12R-2W, 8-11
20200302@856.asc	LSM1_16 spot-7	376-U1530A-12R-2W, 8-11
20200302@857.asc	LSM1_16 spot-8	376-U1530A-12R-2W, 8-11
20200302@858.asc	LSM1_16 spot-9	376-U1530A-12R-2W, 8-11
20200302@859.asc	LSM1 UWQ-1 g1	
20200302@860.asc	LSM1 UWQ-1 g1	
20200302@861.asc	LSM1 UWQ-1 g1	
20200302@862.asc	LSM1 UWQ-1 g1	
	average and 2SD	
	bracket average and 2SD	
20200302@863.asc	LSM1_16 spot-10	376-U1530A-12R-2W, 8-11
20200302@864.asc	LSM1_17 spot-1	376-U1530A-4R-1W, 67-69

20200302@865.asc	LSM1_17 spot-2	376-U1530A-4R-1W, 67-69
20200302@866.asc	LSM1_18 spot-1	376-U1530A-4R-1W, 67-69
20200302@867.asc	LSM1_12 spot-1	376-U1530A-64R-1W, 73-75
20200302@868.asc	LSM1_12 spot-2	376-U1530A-64R-1W, 73-75
20200302@869.asc	LSM1_12 spot-3 CsRes=145	376-U1530A-64R-1W, 73-75
20200302@870.asc	LSM1_12 spot-4	376-U1530A-64R-1W, 73-75
20200302@871.asc	LSM1_12 spot-5	376-U1530A-64R-1W, 73-75
20200302@872.asc	LSM1_12 spot-6	376-U1530A-64R-1W, 73-75
20200302@873.asc	LSM1_12 spot-7	376-U1530A-64R-1W, 73-75
20200302@874.asc	LSM1_12 spot-8	376-U1530A-64R-1W, 73-75
20200302@875.asc	LSM1_12 spot-9	376-U1530A-64R-1W, 73-75
20200302@876.asc	LSM1_12 spot-10	376-U1530A-64R-1W, 73-75
20200302@877.asc	LSM1_12 spot-11	376-U1530A-64R-1W, 73-75
20200302@878.asc	LSM1_12 spot-12	376-U1530A-64R-1W, 73-75
20200302@879.asc	LSM1_12 spot-13	376-U1530A-64R-1W, 73-75
20200302@880.asc	LSM1_12 spot-14	376-U1530A-64R-1W, 73-75
20200302@881.asc	LSM1_12 spot-15	376-U1530A-64R-1W, 73-75
20200302@882.asc	LSM1_12 spot-16	376-U1530A-64R-1W, 73-75
20200302@883.asc	LSM1 UWQ-1 g1	
20200302@884.asc	LSM1 UWQ-1 g1	
20200302@885.asc	LSM1 UWQ-1 g1	
20200302@886.asc	LSM1 UWQ-1 g1	
	average and 2SD	
	bracket average and 2SD	
20200302@887.asc	LSM1_12 spot-17	376-U1530A-64R-1W, 73-75
20200302@888.asc	LSM1_12 spot-18	376-U1530A-64R-1W, 73-75
20200302@889.asc	LSM1_12 spot-19	376-U1530A-64R-1W, 73-75
20200302@890.asc	LSM1_12 spot-20	376-U1530A-64R-1W, 73-75
20200302@891.asc	LSM1_13 spot-1	376-U1530A-64R-1W, 73-75
20200302@892.asc	LSM1_13 spot-2	376-U1530A-64R-1W, 73-75
20200302@893.asc	LSM1_13 spot-3	376-U1530A-64R-1W, 73-75
20200302@894.asc	LSM1_13 spot-4	376-U1530A-64R-1W, 73-75
20200302@895.asc	LSM1_13 spot-5	376-U1530A-64R-1W, 73-75
20200302@896.asc	LSM1_13 spot-6	376-U1530A-64R-1W, 73-75
20200302@897.asc	LSM1_13 spot-7	376-U1530A-64R-1W, 73-75
20200302@898.asc	LSM1_13 spot-8	376-U1530A-64R-1W, 73-75
20200302@899.asc	LSM1_13 spot-9	376-U1530A-64R-1W, 73-75
20200302@900.asc	LSM1_13 spot-10	376-U1530A-64R-1W, 73-75
20200302@901.asc	LSM1_13 spot-11	376-U1530A-64R-1W, 73-75
20200302@902.asc	LSM1_13 spot-12	376-U1530A-64R-1W, 73-75
20200302@903.asc	LSM1_13 spot-13 CsRes=146	376-U1530A-64R-1W, 73-75
20200302@904.asc	LSM1_13 spot-14	376-U1530A-64R-1W, 73-75
20200302@905.asc	LSM1_13 spot-15	376-U1530A-64R-1W, 73-75
20200302@906.asc	LSM1_13 spot-16	376-U1530A-64R-1W, 73-75
20200302@907.asc	LSM1 UWQ-1 g1	

20200302@908.asc	LSM1 UWQ-1 g1	
20200302@909.asc	LSM1 UWQ-1 g1	
20200302@910.asc	LSM1 UWQ-1 g1	
	average and 2SD	
	bracket average and 2SD	
20200302@911.asc	LSM1_13 spot-17	376-U1530A-64R-1W, 73-75
20200302@912.asc	LSM1_13 spot-18	376-U1530A-64R-1W, 73-75
20200302@913.asc	LSM1_13 spot-19	376-U1530A-64R-1W, 73-75
20200302@914.asc	LSM1_13 spot-20	376-U1530A-64R-1W, 73-75
20200302@915.asc	LSM1 UWQ-1 g1	
20200302@916.asc	LSM1 UWQ-1 g1	
20200302@917.asc	**LSM1 UWQ-1 g1**	
20200302@918.asc	LSM1 UWQ-1 g1	
	average and 2SD	
	bracket average and 2SD	

*External error is given as 2 standard deviations (2SD) of the quartz standard values for a particu

#Uncorrected value measured on the ion probe.

†Internal error is reported as 2 standard error of an individual spot (2SE) during measurement.

**$^{16}O^{1}H/^{16}O$ was measured to monitor potential contamination by water.

ıaterial (IODP Exp. 376, Brothers volcano) and the reference material UWQ-1. The position of the measuri

quartz replacement type	$\delta^{18}O$ ‰ VSMOW	2SD (external error)*	Mass Bias (‰)	$\delta^{18}O$ ‰ raw#
				3.24
				3.27
				3.26
				3.23
				3.25
vug infill	7.02	0.12	-8.97	-2.01
vug infill	6.99	0.12	-8.97	-2.04
vug infill	6.65	0.12	-8.97	-2.38
vug infill	8.69	0.12	-8.97	-0.35
vug infill	6.26	0.12	-8.97	-2.77
vug infill	6.57	0.12	-8.97	-2.46
vug infill	6.60	0.12	-8.97	-2.43
vug infill	6.34	0.12	-8.97	-2.69
vug infill	6.22	0.12	-8.97	-2.80
vug infill	6.61	0.12	-8.97	-2.42
vug infill	6.27	0.12	-8.97	-2.76
vug infill	6.73	0.12	-8.97	-2.30
vug infill	6.38	0.12	-8.97	-2.64
vug infill	6.33	0.12	-8.97	-2.70
vug infill	6.80	0.12	-8.97	-2.23
vug infill	6.20	0.12	-8.97	-2.83
vug infill	6.86	0.12	-8.97	-2.17
vug infill	6.36	0.12	-8.97	-2.66
vug infill	6.17	0.12	-8.97	-2.86
vug infill	6.32	0.12	-8.97	-2.70
				3.38
				3.24
				3.22
				3.16
				3.25
	12.33		**-8.97**	**3.25**
vein infill	8.09	0.18	-8.91	-0.90
vein infill	8.71	0.18	-8.91	-0.28
vein infill	7.56	0.18	-8.91	-1.42
vein infill	7.41	0.18	-8.91	-1.57
vein infill	7.13	0.18	-8.91	-1.84
vein infill	7.20	0.18	-8.91	-1.77
vein infill	7.76	0.18	-8.91	-1.22
vein infill	6.76	0.18	-8.91	-2.21
vein infill	6.42	0.18	-8.91	-2.55
vein infill	7.80	0.18	-8.91	-1.18

vug infill	9.55	0.18	-8.91	0.56
vug infill	8.39	0.18	-8.91	-0.59
vug infill	9.05	0.18	-8.91	0.06
vug infill	6.26	0.18	-8.91	-2.70
vug infill	7.15	0.18	-8.91	-1.82
vug infill	6.11	0.18	-8.91	-2.85
vug infill	7.61	0.18	-8.91	-1.36
vug infill	7.77	0.18	-8.91	-1.21
vug infill	6.05	0.18	-8.91	-2.92
vug infill	5.93	0.18	-8.91	-3.03
				3.31
				3.37
				3.39
				3.41
				3.37
	12.33		**-8.91**	**3.31**
matrix replacement	8.50	0.11	-8.84	-0.42
matrix replacement	8.52	0.11	-8.84	-0.39
matrix replacement	7.51	0.11	-8.84	-1.40
matrix replacement	7.86	0.11	-8.84	-1.04
matrix replacement	7.77	0.11	-8.84	-1.14
matrix replacement	8.67	0.11	-8.84	-0.24
matrix replacement	8.60	0.11	-8.84	-0.32
vein infill	7.42	0.11	-8.84	-1.48
vein infill	7.29	0.11	-8.84	-1.62
vein infill	6.78	0.11	-8.84	-2.12
vein infill	7.93	0.11	-8.84	-0.98
vug infill	5.61	0.11	-8.84	-3.28
vug infill	6.29	0.11	-8.84	-2.60
vug infill	6.13	0.11	-8.84	-2.77
vug infill	7.83	0.11	-8.84	-1.08
vug infill	5.82	0.11	-8.84	-3.07
vug infill	6.00	0.11	-8.84	-2.89
vug infill	6.29	0.11	-8.84	-2.61
vug infill	7.32	0.11	-8.84	-1.58
vug infill	7.61	0.11	-8.84	-1.30
				3.42
				3.48
				3.36
				3.33
				3.40
	12.33		**-8.84**	**3.38**
vug infill	6.58	0.15	-8.85	-2.33
vein infill	9.15	0.15	-8.85	0.22

vein infill	8.83	0.15	-8.85	-0.11
vein infill	8.68	0.15	-8.85	-0.25
vein infill	7.52	0.15	-8.85	-1.40
vein infill	8.85	0.15	-8.85	-0.08
vein infill	8.59	0.15	-8.85	-0.34
vein infill	8.96	0.15	-8.85	0.02
vein infill	8.99	0.15	-8.85	0.06
vein infill	8.85	0.15	-8.85	-0.08
vein infill	8.64	0.15	-8.85	-0.29
vein infill	8.88	0.15	-8.85	-0.05
vein infill	8.85	0.15	-8.85	-0.08
vein infill	8.84	0.15	-8.85	-0.09
vein infill	8.81	0.15	-8.85	-0.12
vein infill	8.65	0.15	-8.85	-0.28
vein infill	8.86	0.15	-8.85	-0.07
vein infill	9.04	0.15	-8.85	0.11
vein infill	9.04	0.15	-8.85	0.10
vein infill	8.87	0.15	-8.85	-0.06
				3.33
				3.29
				3.45
				3.27
				3.34
	12.33		**-8.85**	**3.37**
vein infill	9.47	0.15	-8.87	0.52
vein infill	9.46	0.15	-8.87	0.51
vein infill	9.90	0.15	-8.87	0.95
vein infill	8.26	0.15	-8.87	-0.68
vein infill	8.92	0.15	-8.87	-0.03
vein infill	9.11	0.15	-8.87	0.16
vein infill	8.99	0.15	-8.87	0.04
vein infill	8.79	0.15	-8.87	-0.15
vein infill	8.86	0.15	-8.87	-0.09
vein infill	8.90	0.15	-8.87	-0.05
vein infill	9.15	0.15	-8.87	0.20
vein infill	9.03	0.15	-8.87	0.09
vein infill	9.36	0.15	-8.87	0.41
vein infill	9.55	0.15	-8.87	0.60
vein infill	7.35	0.15	-8.87	-1.59
vein infill	7.18	0.15	-8.87	-1.76
vein infill	8.06	0.15	-8.87	-0.88
vein infill	7.97	0.15	-8.87	-0.97
vein infill	7.03	0.15	-8.87	-1.90
vein infill	6.81	0.15	-8.87	-2.12
				3.46

			3.40
			3.34
			3.28
			3.37
12.33		**-8.87**	**3.35**
6.68	0.20	-8.86	-2.24
6.74	0.20	-8.86	-2.18
7.74	0.20	-8.86	-1.19
7.08	0.20	-8.86	-1.84
			3.38
			3.47
			~~0.34~~
			3.18
			3.35
12.33		**-8.86**	**3.36**

ılar bracket.

ng points is projected to the CL images (F level) of the quartz separates.

2SE (internal error)†	^{16}O (Gcps)	Primary beam intensity (nA)	Yield (Gcps/nA)	X
0.29	3.09	1.96	1.58	2660
0.28	3.10	1.97	1.58	2685
0.32	3.12	1.97	1.58	2710
0.32	3.12	1.97	1.58	2735
0.04				
0.28	2.98	1.97	1.51	201
0.34	3.10	1.97	1.57	182
0.33	3.10	1.96	1.58	160
0.38	3.10	1.96	1.58	147
0.27	3.10	1.95	1.59	139
0.35	3.10	1.95	1.59	129
0.33	3.11	1.94	1.60	116
0.35	3.09	1.93	1.60	101
0.32	3.08	1.93	1.60	86
0.36	3.01	1.92	1.56	71
0.24	2.97	1.92	1.55	2374
0.30	2.96	1.91	1.55	2324
0.30	2.98	1.90	1.57	2274
0.31	2.98	1.89	1.58	2224
0.31	2.99	1.89	1.59	2174
0.28	2.97	1.88	1.58	2124
0.35	2.97	1.87	1.59	2074
0.31	2.93	1.86	1.58	2024
0.34	2.90	1.85	1.57	1975
0.30	2.87	1.84	1.55	1925
0.37	3.08	1.96	1.57	2660
0.32	3.14	2.00	1.57	2685
0.34	3.16	2.01	1.57	2710
0.32	3.18	2.02	1.57	2735
0.18				
0.12			**1.58**	
0.30	2.78	2.01	1.38	-3068
0.22	2.99	2.02	1.48	-3036
0.28	3.02	2.02	1.50	-3004
0.35	3.09	2.02	1.53	-2972
0.32	3.10	2.01	1.54	-2941
0.26	3.15	2.01	1.57	-2909
0.35	3.16	2.00	1.58	-2877
0.32	3.20	2.00	1.60	-2845
0.30	3.22	2.00	1.61	-2813
0.36	3.19	2.00	1.60	-2781

0.35	2.93	1.99	1.47	-2714
0.32	3.05	1.99	1.54	-2636
0.37	3.02	1.98	1.52	-2558
0.23	3.02	1.97	1.53	-2479
0.34	3.04	1.96	1.55	-2401
0.32	3.00	1.96	1.53	-2323
0.29	3.03	1.95	1.55	-2244
0.42	3.01	1.95	1.55	-2166
0.24	2.98	1.93	1.54	-2088
0.25	2.96	1.92	1.54	-2010
0.29	3.00	1.92	1.56	2660
0.30	2.98	1.91	1.56	2685
0.26	3.00	1.91	1.57	2710
0.29	2.99	1.90	1.57	2735
0.08				
0.18			**1.57**	
0.31	2.99	1.89	1.58	-932
0.22	2.75	1.89	1.46	-1054
0.41	3.02	1.88	1.61	1653
0.33	2.99	1.87	1.60	1553
0.33	2.92	1.86	1.57	1454
0.36	2.85	1.83	1.56	1355
0.27	2.75	1.94	1.42	1258
0.33	3.17	1.97	1.60	3875
0.32	3.19	1.98	1.61	4217
0.24	3.20	1.99	1.61	4322
0.25	3.13	1.99	1.58	4736
0.32	3.18	1.98	1.60	123
0.35	3.13	1.98	1.58	37
0.34	3.12	1.98	1.58	-48
0.26	3.09	1.98	1.57	-134
0.33	3.10	1.97	1.57	-220
0.32	3.07	1.96	1.56	-305
0.30	2.99	1.95	1.53	-391
0.25	2.88	1.94	1.49	-477
0.27	2.67	1.93	1.38	-563
0.33	3.01	1.92	1.56	2660
0.37	2.98	1.91	1.56	2685
0.31	2.99	1.91	1.57	2710
0.30	2.99	1.90	1.57	2735
0.13				
0.11			**1.57**	
0.29	2.54	1.89	1.35	-648
0.25	2.86	1.88	1.52	1624

0.30	2.98	1.88	1.59	1898
0.29	2.92	1.87	1.56	2270
0.26	3.06	1.86	1.65	-1185
0.33	2.91	1.85	1.57	-1244
0.34	3.16	1.97	1.60	-1303
0.34	3.21	2.00	1.60	-1362
0.31	3.21	2.01	1.59	-1421
0.39	3.20	2.02	1.59	-1480
0.32	3.22	2.02	1.59	-1539
0.28	3.22	2.02	1.59	-1598
0.33	3.21	2.02	1.59	-1657
0.37	3.17	2.01	1.58	-1716
0.33	3.16	2.00	1.58	-1775
0.28	3.15	2.00	1.58	-1834
0.34	3.13	1.99	1.57	-1893
0.34	3.12	1.99	1.57	-1951
0.35	3.12	1.98	1.57	-2010
0.32	3.08	1.98	1.56	-2069
0.33	3.09	1.98	1.56	2660
0.31	3.09	1.98	1.56	2685
0.35	3.09	1.97	1.56	2710
0.31	3.10	1.97	1.57	2735
0.16				
0.15			**1.57**	
0.36	3.02	1.96	1.54	-2128
0.32	2.97	1.95	1.52	-2187
0.38	2.87	1.95	1.48	-2246
0.29	2.74	1.94	1.41	-2304
0.27	3.07	1.94	1.58	-203
0.34	3.04	1.94	1.57	-255
0.31	3.04	1.93	1.58	-307
0.34	3.02	1.92	1.57	-359
0.29	2.99	1.91	1.57	-410
0.30	2.97	1.89	1.57	-462
0.35	2.96	1.88	1.57	-514
0.39	2.95	1.87	1.57	-566
0.34	2.93	1.87	1.57	-618
0.31	2.92	1.86	1.57	-670
0.30	2.90	1.85	1.56	-721
0.33	2.90	1.85	1.57	-773
0.20	3.10	1.97	1.57	-825
0.35	3.15	2.01	1.57	-877
0.37	3.14	2.02	1.56	-929
0.33	3.14	2.02	1.55	-981
0.33	3.15	2.02	1.56	2660

0.30	3.17	2.03	1.56	2685
0.30	3.18	2.02	1.57	2710
0.33	3.19	2.02	1.58	2735
0.16				
0.15			**1.57**	
0.29	3.13	2.02	1.55	-1033
0.34	3.08	2.02	1.53	-1084
0.48	3.04	2.02	1.51	-1136
0.31	2.84	2.01	1.41	-1188
0.27	3.14	2.01	1.56	2660
0.37	3.14	2.01	1.56	2685
~~0.43~~	~~3.00~~	~~2.01~~	~~1.49~~	~~2710~~
0.32	3.15	2.01	1.57	2735
0.29				
0.20			**1.57**	

Y	DTFA-X	DTFA-Y	$^{16}O^{1}H/^{16}O$**	reasons for rejection
-1291	-21	-18	0.000433151	
-1291	-21	-18	0.000432442	
-1291	-21	-18	0.000428615	
-1291	-21	-17	0.000434105	
603	-16	-16	0.000631247	
720	-17	-13	0.000605429	
827	-17	-12	0.000646146	
920	-17	-11	0.000700863	
1033	-17	-9	0.000495338	
1134	-17	-8	0.000533974	
1237	-15	-6	0.000621931	
1355	-14	-5	0.000771374	
1441	-14	-5	0.00065283	
1532	-14	-6	0.000612831	
294	-18	-14	0.000432296	
329	-18	-13	0.000741974	
363	-19	-13	0.000658627	
397	-19	-13	0.000683699	
431	-20	-12	0.000636441	
465	-19	-11	0.000511395	
499	-19	-10	0.000592954	
534	-18	-9	0.000760161	
568	-18	-8	0.000702317	
602	-19	-9	0.000714963	
-1311	-20	-18	0.000427062	
-1311	-20	-18	0.00043297	
-1311	-20	-18	0.000435911	
-1311	-20	-18	0.000432281	
			0.000432067	
-1380	-7	-20	0.000498536	
-1306	-8	-18	0.000504841	
-1232	-8	-17	0.000539515	
-1158	-9	-16	0.000559826	
-1084	-9	-14	0.000542666	
-1010	-10	-12	0.000527462	
-936	-11	-11	0.000454647	
-862	-11	-9	0.000503291	
-788	-10	-8	0.000483451	
-714	-7	-11	0.000434279	

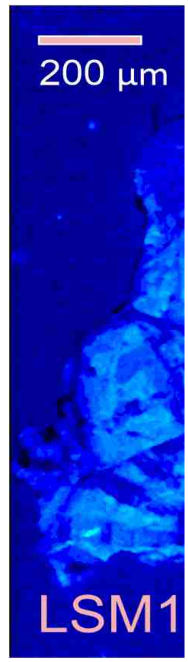

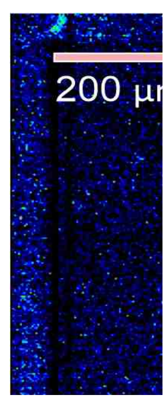

-3261	-6	-16	0.000791031
-3315	-7	-16	0.000765052
-3369	-8	-17	0.000774299
-3423	-9	-18	0.000728584
-3478	-10	-19	0.000739651
-3532	-11	-21	0.00061307
-3586	-11	-22	0.000648854
-3640	-11	-22	0.000554894
-3695	-11	-22	0.00060175
-3749	-7	-22	0.000417288

-1331	-19	-17	0.000417081
-1331	-20	-17	0.000423004
-1331	-20	-17	0.000413843
-1331	-20	-17	0.000399451

0.0004227

2989	-15	-6	0.0004155
2629	-12	-16	0.000387917
2587	-19	-5	0.00041913
2565	-17	-7	0.000526663
2543	-17	-8	0.000759426
2520	-16	-8	0.000674942
2485	-14	-9	0.000572205
1048	-22	-11	0.000408314
1428	-18	-7	0.000411743
-1215	-21	-14	0.000378405
-1266	-20	-15	0.000500078
-4384	-12	-22	0.000596559
-4420	-14	-21	0.000802076
-4456	-14	-22	0.000655582
-4492	-14	-23	0.004181011
-4528	-13	-25	0.000570781
-4565	-13	-26	0.000552443
-4601	-12	-27	0.000557125
-4637	-11	-27	0.000766271
-4673	-10	-28	0.0007599

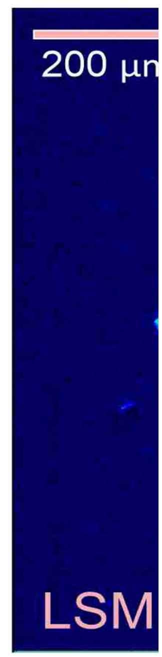

-1351	-20	-18	0.000389316
-1351	-20	-18	0.00041456
-1351	-20	-18	0.000400483
-1351	-20	-18	0.000385166

0.000405363

-4710	-8	-28	0.000578133
-3941	-15	-24	0.000863076

-3976	-12	-24	0.000860303
-3670	-12	-21	0.000703863
-2192	-9	-15	0.000739032
-2184	-9	-16	0.000705499
-2175	-11	-15	0.000503533
-2167	-12	-15	0.000455464
-2158	-12	-15	0.000429677
-2150	-12	-15	0.000470253
-2142	-12	-15	0.000464728
-2133	-12	-16	0.000467091
-2125	-12	-16	0.000439952
-2116	-12	-16	0.000391831
-2108	-11	-16	0.000378045
-2099	-11	-15	0.000375505
-2091	-11	-15	0.000372192
-2082	-10	-15	0.000374508
-2074	-10	-15	0.000396482
-2066	-9	-16	0.000382499

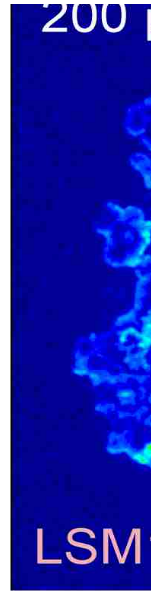

-1371	-20	-19	0.000366287
-1371	-20	-19	0.000385285
-1371	-20	-19	0.000385521
-1371	-20	-19	0.000364706

0.000386415

-2057	-9	-14	0.000501125
-2049	-9	-15	0.00039952
-2041	-8	-16	0.000522515
-2032	-7	-15	0.000555443
-2430	-18	-19	0.00037271
-2429	-17	-19	0.000474038
-2428	-17	-19	0.000392212
-2427	-17	-18	0.00038333
-2425	-16	-18	0.00052996
-2424	-16	-18	0.000565558
-2422	-16	-18	0.000641005
-2421	-16	-18	0.000405183
-2419	-15	-18	0.000499663
-2418	-15	-18	0.000531048
-2416	-15	-17	0.000507714
-2414	-14	-18	0.000478194
-2413	-14	-18	0.000527978
-2411	-13	-18	0.00048105
-2409	-13	-18	0.000439964
-2408	-12	-18	0.00048224

-1391	-20	-19	0.000357101

-1391	-20	-19	0.000372741	
-1391	-20	-19	0.000374501	
-1391	-20	-19	0.000351889	
			0.000369754	
-2406	-12	-18	0.000455957	
-2404	-12	-18	0.000515341	
-2402	-13	-18	0.000445007	
-2401	-12	-18	0.000380405	
-1411	-20	-19	0.000353871	
-1411	-20	-19	0.000392931	
~~-1411~~	~~-20~~	~~-19~~	~~0.000397239~~	Low yield and higher 2SE
-1411	-20	-19	0.000354315	
			0.000365335	

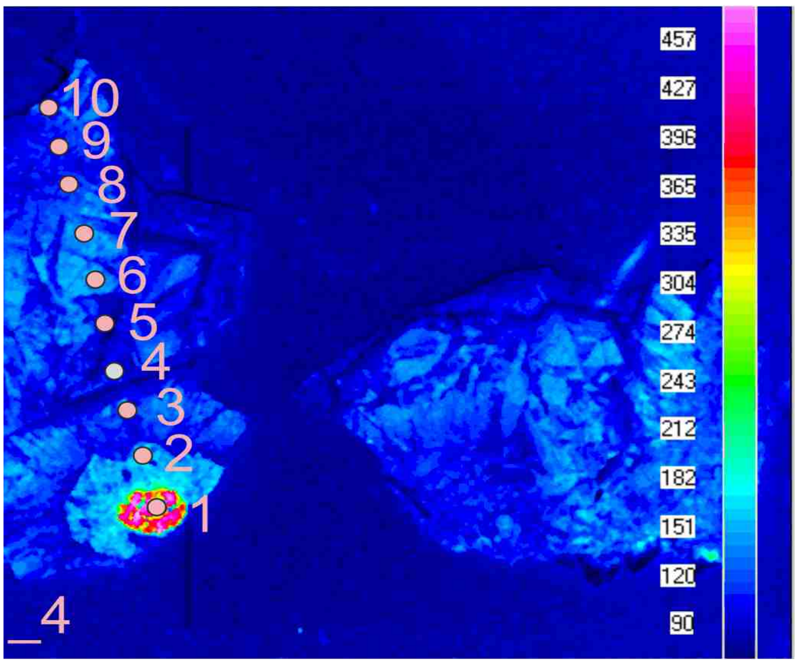
10
9
8
7
6
5
4
3
2
1
_4
457
427
396
365
335
304
274
243
212
182
151
120
90

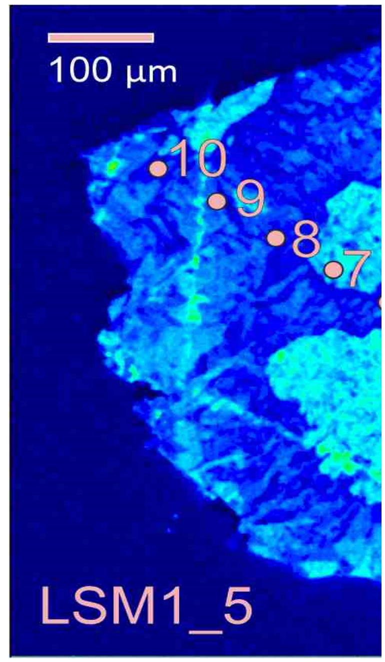
100 μm
10
9
8
7
LSM1_5

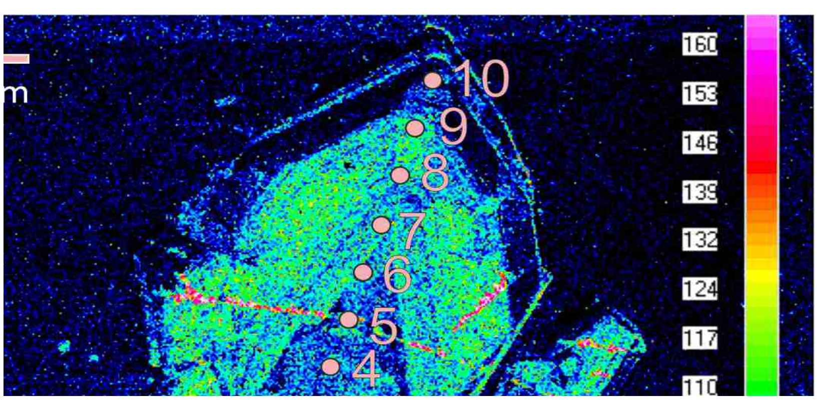
m
10
9
8
7
6
5
4
160
153
146
139
132
124
117
110

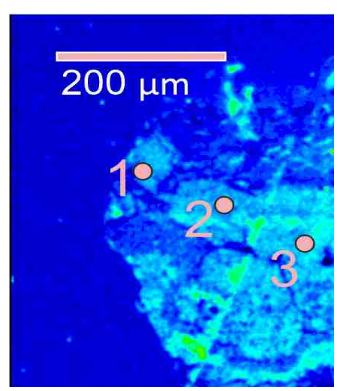
200 μm
1
2
3

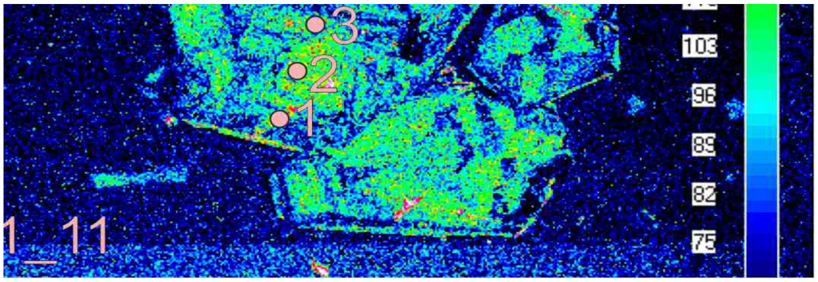
3
2
1
1_11
103
96
89
82
75

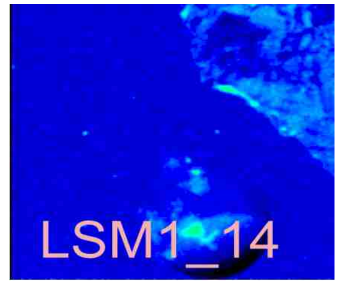
LSM1_14

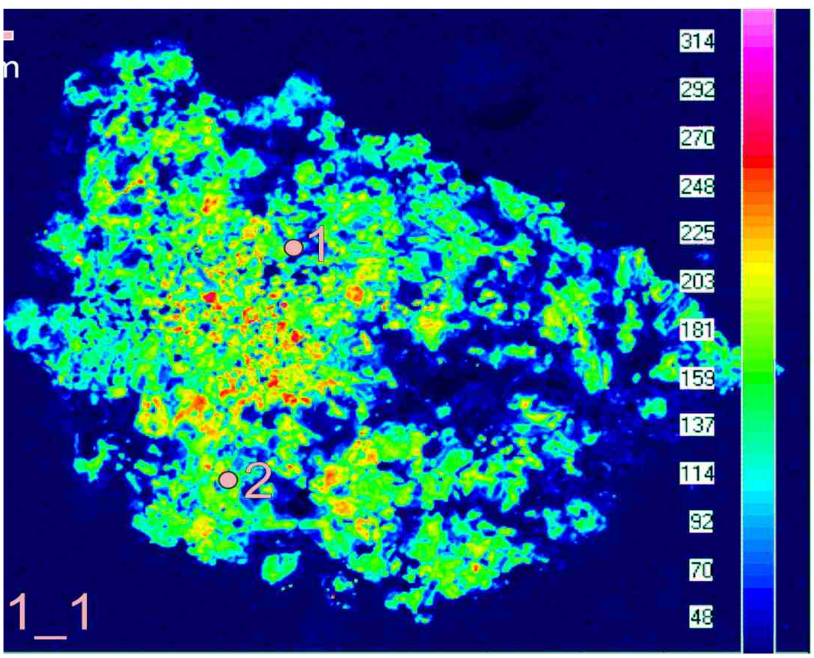
314
292
270
248
225
203
181
159
137
114
92
70
48
1
2
1_1

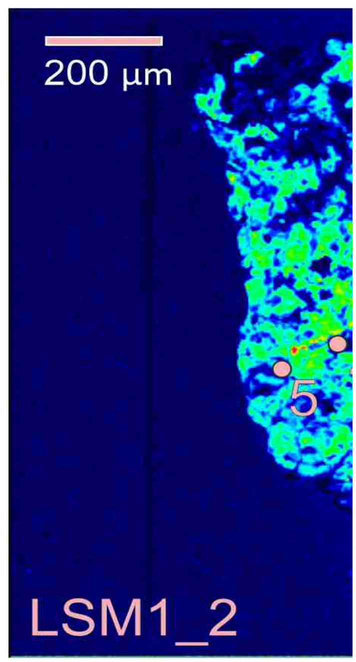
200 µm
5
LSM1_2


311

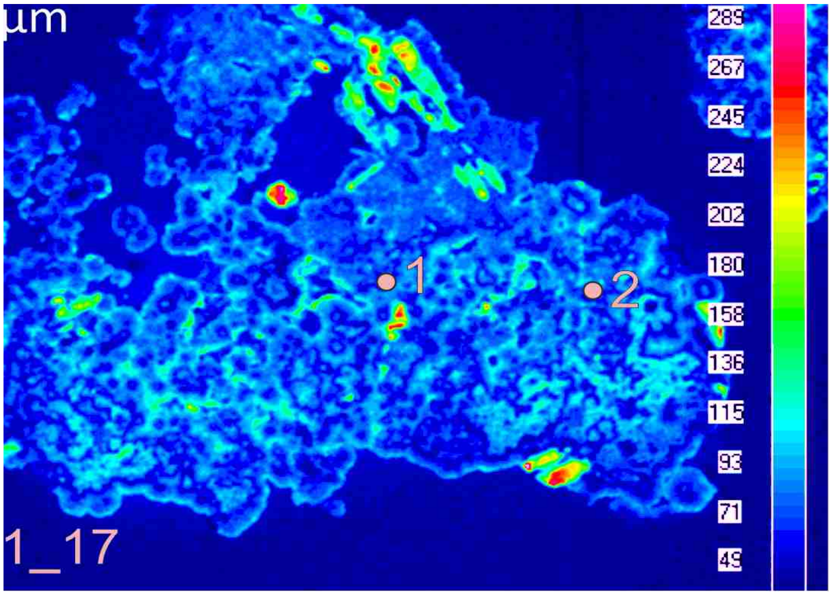
µm
1
2
1_17
289
267
245
224
202
180
158
136
115
93
71
49

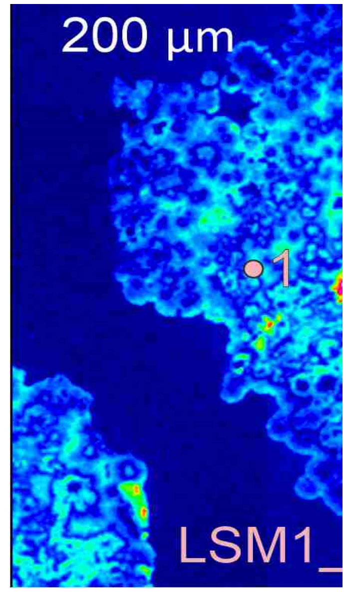
200 µm
1
LSM1_

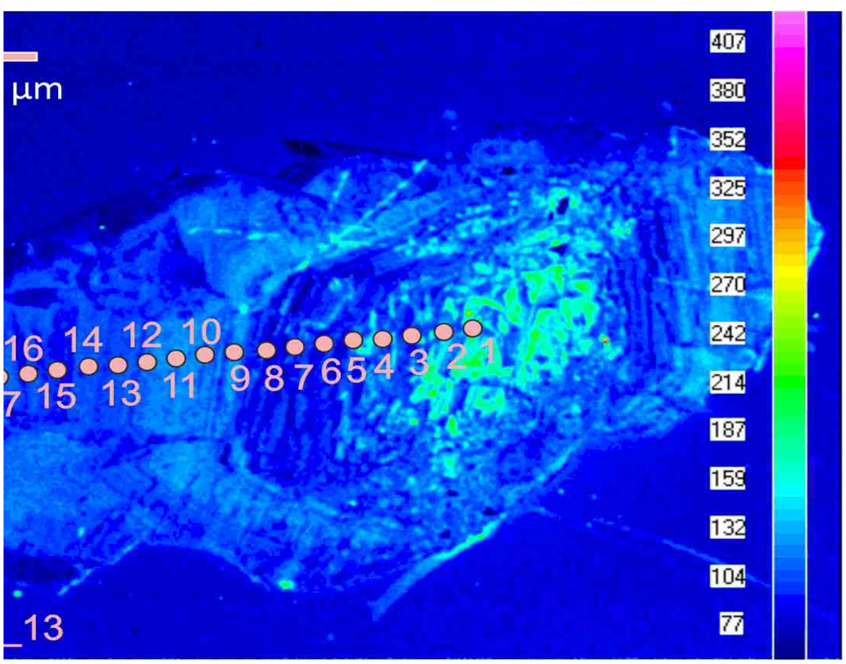
µm
16 14 12 10
15 13 11 9 8 7 6 5 4 3 2 1
_13
407
380
352
325
297
270
242
214
187
159
132
104
77

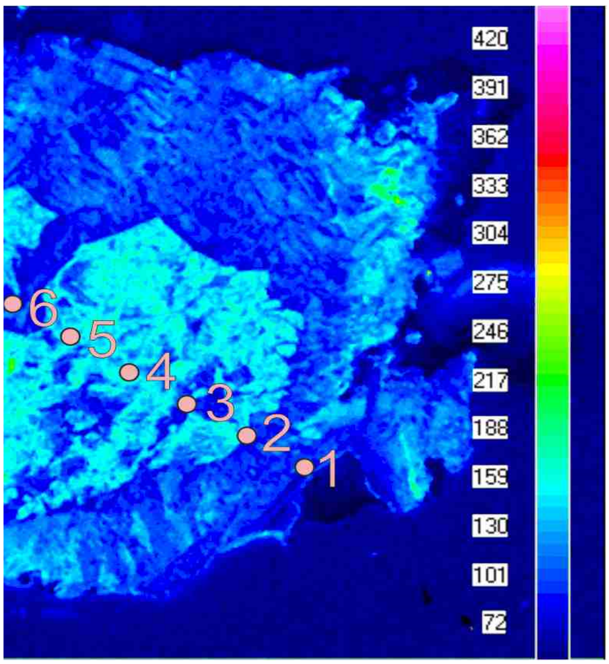

420
391
362
333
304
275
246
217
188
159
130
101
72
6
5
4
3
2
1

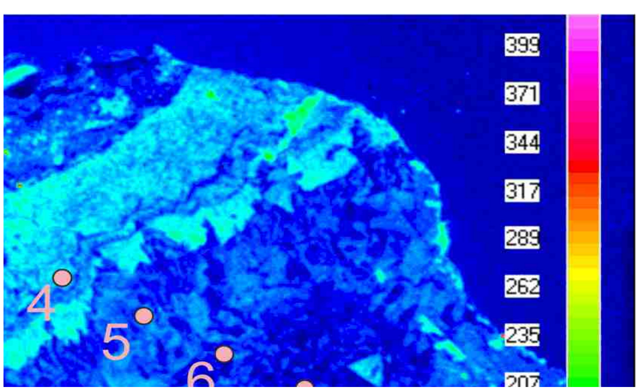

399
371
344
317
289
262
235
4
5
6

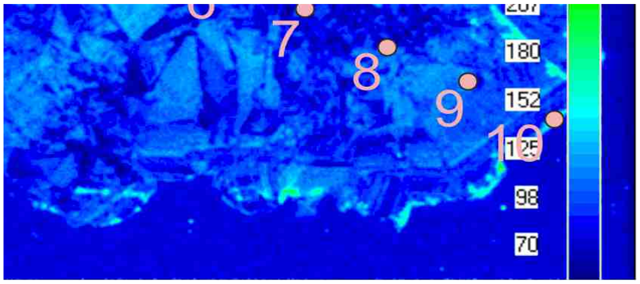
7
8
9
180
152
98
70

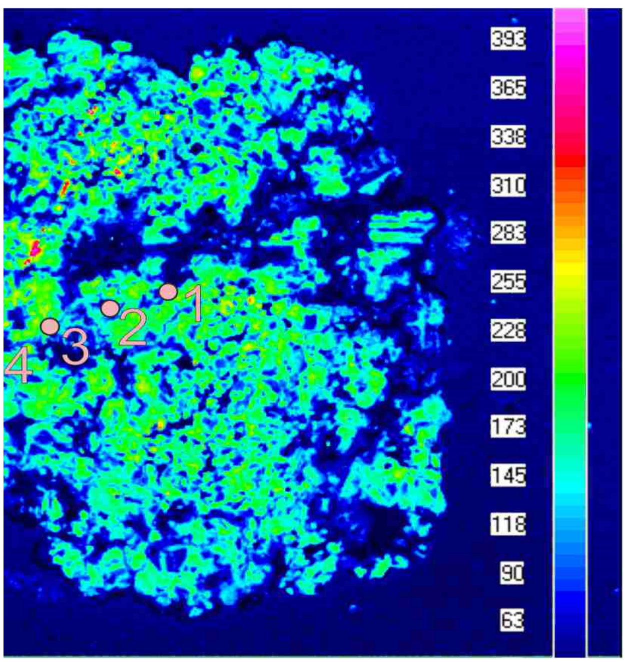
393
365
338
310
283
255
228
200
173
145
118
90
63
1
2
3
4

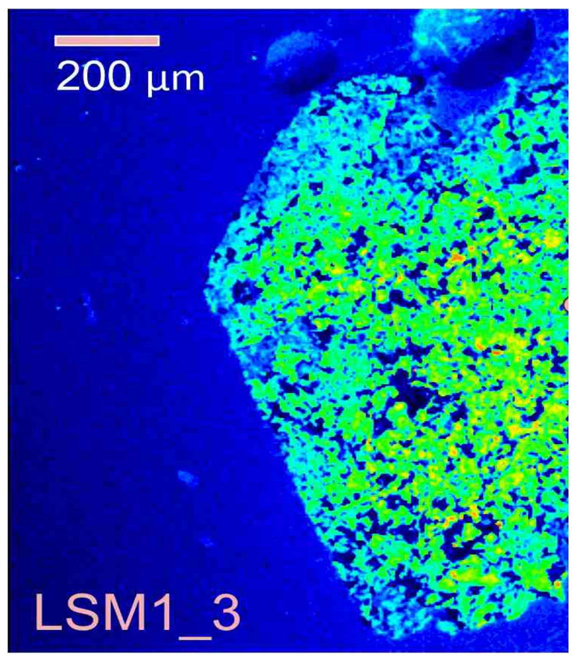
200 µm
LSM1_3


308

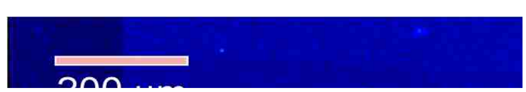

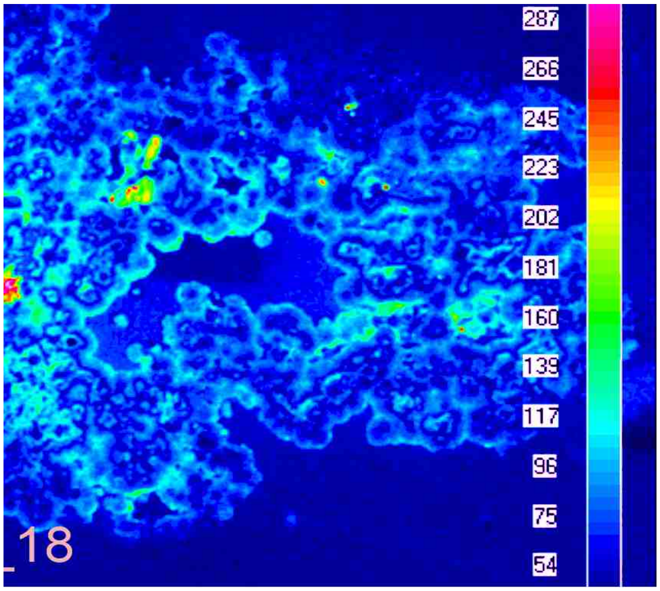
287
266
245
223
202
181
160
139
117
96
75
54
_18

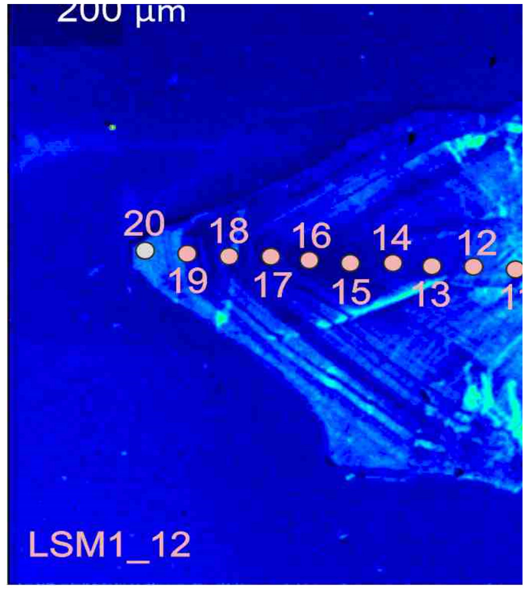
200 µm
20
19
18
17
16
15
14
13
12
LSM1_12

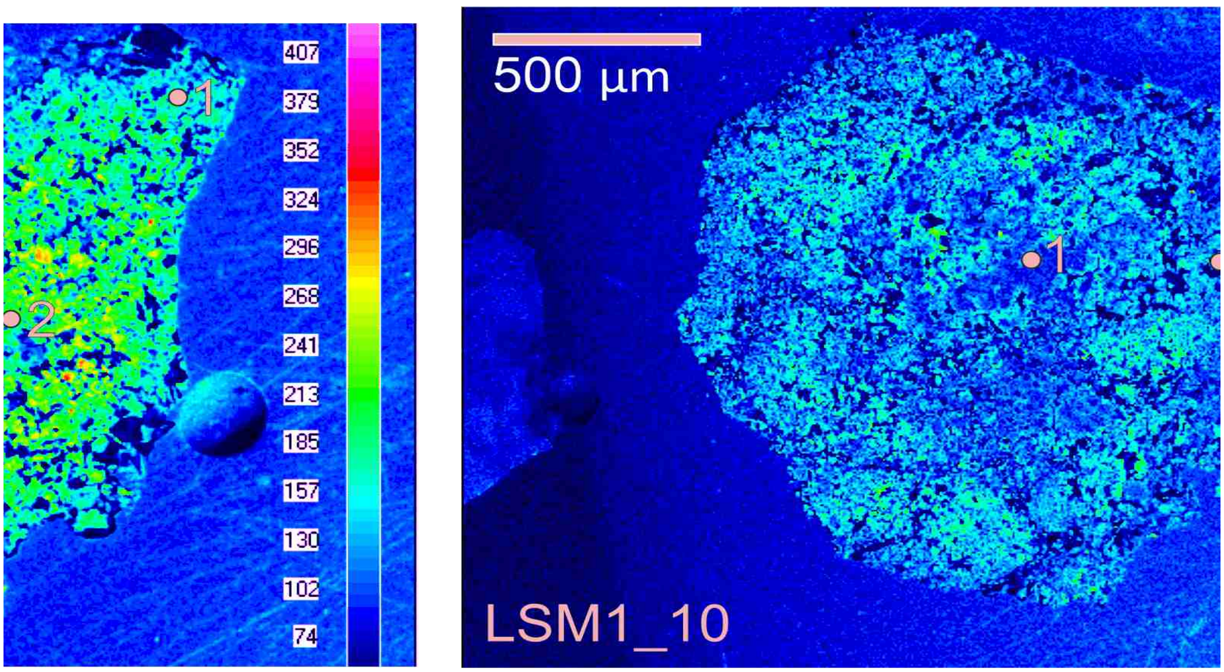
1
2
407
379
352
324
296
268
241
213
185
157
130
102
74
500 µm
1
LSM1_10


408

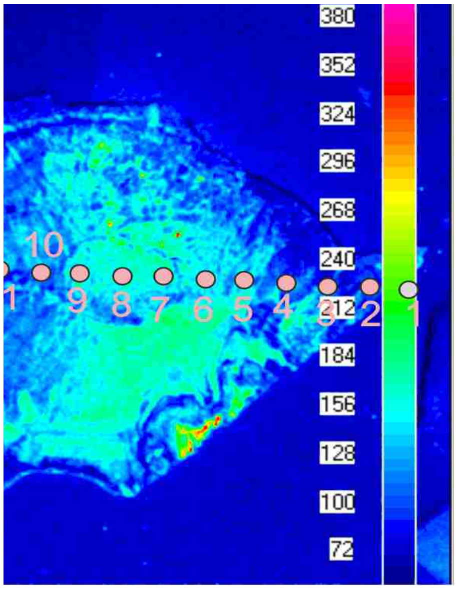
380
352
324
296
268
240
212
184
156
128
100
72
10
1
9
8
7
6
5
4
3
2
1

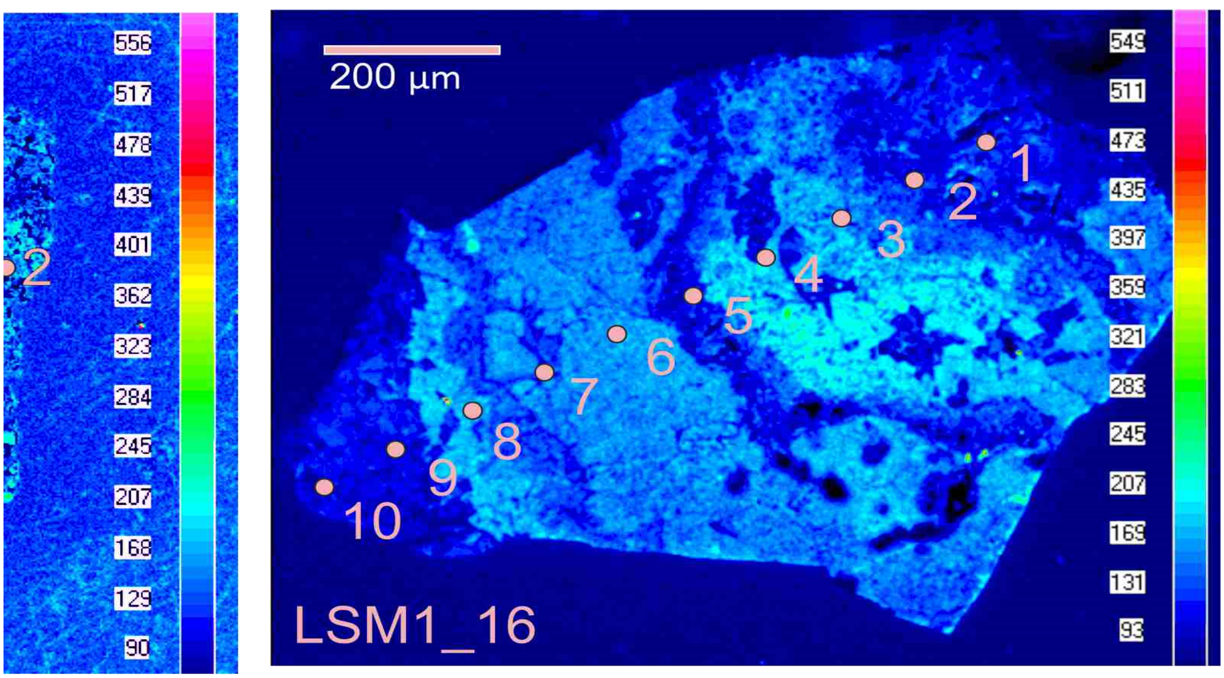
556
517
478
439
401
362
323
284
245
207
168
129
90
2
200 µm
1
2
3
4
5
6
7
8
9
10
LSM1_16
549
511
473
435
397
359
321
283
245
207
169
131
93